



NATIONAL TECHNICAL UNIVERSITY OF ATHENS
SCHOOL OF ELECTRICAL AND COMPUTER ENGINEERING
SCHOOL OF MECHANICAL ENGINEERING

INTERDISCIPLINARY POSTGRADUATE PROGRAMME
“Translational Engineering in Health and Medicine”

***DESIGN AND CONSTRUCTION OF AN ANTHROPOMORPHIC
CARDIAC PHANTOM FOR SIMULATION OF DIAGNOSTIC
NUCLEAR MEDICINE EXAMINATIONS***

Postgraduate Diploma Thesis

ANTONIOS T. SPANIDIS

Supervisor: *Marios J. Anagnostakis,*
Professor – School of Mechanical Engineering, NTUA

Athens, October 2024



NATIONAL TECHNICAL UNIVERSITY OF ATHENS
SCHOOL OF ELECTRICAL AND COMPUTER ENGINEERING
SCHOOL OF MECHANICAL ENGINEERING

INTERDISCIPLINARY POSTGRADUATE PROGRAMME
“Translational Engineering in Health and Medicine”

**DESIGN AND CONSTRUCTION OF AN ANTHROPOMORPHIC
CARDIAC PHANTOM FOR SIMULATION OF DIAGNOSTIC
NUCLEAR MEDICINE EXAMINATIONS**

Postgraduate Diploma Thesis

ANTONIOS T. SPANIDIS

Supervisor : Marios J. Anagnostakis, Professor NTUA

The postgraduate diploma thesis has been approved by the examination committee
on 30th October 2024

1st member

2nd member

3rd member

Marios Anagnostakis

Georgios Matsopoulos

Nikolaos Petropoulos

Professor

Professor

Associate Professor

*School of Mechanical
Engineering NTUA*

*School of Electrical and
Computer Engineering NTUA*

*School of Mechanical
Engineering NTUA*

Athens, October 2024

.....

ANTONIOS T. SPANIDIS

Graduate of the Interdisciplinary Postgraduate Programme,
“Translational Engineering in Health and Medicine”,
Master of Science,
School of Electrical and Computer Engineering,
National Technical University of Athens

Copyright © - (*ANTONIOS T. SPANIDIS, 2024*)

All rights reserved.

You may not copy, reproduce, distribute, publish, display, modify, create derivative works, transmit, or in any way exploit this thesis or part of it for commercial purposes. You may reproduce, store or distribute this thesis for non-profit educational or research purposes, provided that the source is cited, and the present copyright notice is retained. Inquiries for commercial use should be addressed to the original author.

The ideas and conclusions presented in this paper are the author’s and do not necessarily reflect the official views of the National Technical University of Athens.

Abstract

Cardiac scintigraphy, using isotopes like Technetium-99m and Thallium-201, is vital in diagnosing cardiovascular diseases, as it offers detailed imaging of the heart's structure and function. Accurately simulating diagnostic nuclear medicine examinations is crucial for optimizing imaging protocols and improving patient outcomes.

In this study, an anthropomorphic cardiac phantom was designed and constructed using advanced 3D printing techniques at the National Technical University of Athens, with further printing completed at the 3DHUB laboratory. This phantom replicates the anatomical and physiological characteristics of the human heart, providing a valuable tool for testing and refining cardiac imaging procedures.

To assess the performance of different gamma camera systems in cardiac scintigraphy, a series of experiments were conducted using the developed phantom. These experiments involved imaging sessions with a range of gamma cameras, from older one-headed systems to modern two-headed systems and cameras utilizing cutting-edge CZT (Cadmium Zinc Telluride) technology. Each system was evaluated for its ability to capture high-quality images, focusing on key metrics such as spatial resolution and contrast.

Additionally, the study measured and compared the radiation doses delivered to the phantom by each imaging system. These dose comparisons are critical for determining the efficiency of different gamma camera technologies in minimizing radiation exposure while maintaining diagnostic accuracy.

The results of this study offer valuable insights into the strengths and limitations of various gamma camera systems in cardiac imaging. This knowledge can aid in the refinement of imaging protocols, enhancing diagnostic accuracy in nuclear medicine and contributing to better patient care.

This MSc Diploma Thesis was prepared in the Nuclear Technology Department of NTUA School of Mechanical Engineering as part of the course "Medical Imaging and Image Analysis".

I wish to express my sincere thanks to Professor Mr. Marios Anagnostakis for the trust he showed me by assigning me the subject of this Thesis. From our excellent collaboration both during the preparation of this work and during the attendance of the courses of the Nuclear Technology Sector, not only I evolved my knowledge on the subjects of Nuclear Medicine and Radiology but I obtained a plethora of interesting ideas for this thesis.

I would especially like to thank Professor Mr. Vasilios Spitas and the PhD candidate of his laboratory, Mr. Vasilios Gekos for their catalytic contribution and help in the creation of the cardiac phantom. Their help was invaluable and the cooperation with them was impeccable throughout the preparation of this project.

Finally, I would like to thank the staff of KeV Medical Imaging and especially my employers Mr. Kostopoulos Konstantinos and Varonos Agamemnon for their support and trust throughout the duration of this postgraduate program, as without them, this work could not have been completed.

Antonios T. Spanidis
Athens, October 2024

Contents

CHAPTER 1 st	9
INTRODUCTION	9
CHAPTER 2 nd	11
NUCLEAR MEDICINE	11
2.1 Introduction.....	11
2.2 History.....	11
2.3 Radiation sources – Diagnostic Radiopharmaceuticals	12
2.4 Therapeutic Radiopharmaceuticals	13
2.5 Diagnostic Nuclear Medicine systems	14
2.5.1 History	14
2.5.2 Basic principles of analog γ -cameras	15
2.5.3 Basic principles of digital γ -cameras	25
2.6.1 Importance of Cyclotrons.....	29
2.6.2 History of PET and early designs	31
2.6.3 Modern Commercial PET Systems	34
2.6.4 Physics of PET Imaging	40
CHAPTER 3 rd	42
NUCLEAR CARDIOLOGY	42
3.1 Introduction.....	42
3.2 Anatomy and Physiology	42
3.3 SPECT Myocardial Perfusion Imaging.....	43
3.4 Cardiac Scintigraphy Radiopharmaceuticals.....	45
CHAPTER 4 th	60
CARDIAC PHANTOM CONSTRUCTION	60
4.1 Introduction to 3D Printing	60
4.2 History of 3D Printing	60
4.3 Basic methods of 3D Printing.....	61
4.3.1 Stereolithography (SLA)	61
4.3.2 Fused Deposition Modeling (FDM)	66
4.3.3 Selective Laser Sintering (SLS)	71
4.3.4 Digital Light Processing (DLP).....	75
4.3.5 Multi Jet Fusion (MJF)	80

4.4 Advantages and Disadvantages of 3D Printing Methods	81
4.5 3D Printing in Medicine	82
4.6 Development of the Cardiac Phantom	87
CHAPTER 5 th	95
CARDIAC PHANTOM IMAGING	95
5.1 General Framework of Cardiac Phantom Imaging	95
5.2 Overview of SPECT Systems Employed	98
5.3 Cardiac Phantom Imaging and Processing Experiment	100
5.3.1 Variation 1: Simulating Realistic Heart Activity	101
5.3.2 Variation 2: High-Activity Simulation	118
5.3.3 Variation 3: Low-Dose Protocol for the CZT System	130
CHAPTER 6 th	133
SUMMARY OF FINDINGS AND FUTURE PERSPECTIVES	133
6.1 Synopsis and Conclusions	133
6.2 Recommendations and Future Research Plans	135
BIBLIOGRAPHY	137

CHAPTER 1st

INTRODUCTION

The creation of a realistic human heart phantom for the simulation of cardiac scintigraphy examinations represents a significant advancement in Nuclear Medicine imaging. Cardiac scintigraphy is widely used for diagnosing coronary artery disease and assessing myocardial perfusion. However, most commercially available cardiac phantoms are simple, hollow, oval vessels that can be filled with water but do not accurately represent the complex anatomical structure of a human left ventricle (LV). This limitation can result in less reliable simulation data and challenges in producing realistic imaging results.

In this thesis, the primary objective was to design and construct a realistic anthropomorphic heart phantom to simulate both normal cardiac function and various degrees of artificial myocardial infarctions of different diameters. The images generated from this phantom were compared across three distinct SPECT systems: an older round single-head SPECT system, a more modern dual-head system, and a state-of-the-art cardiac-specific CZT system. These systems represent a range of technological advancements in nuclear cardiology imaging, and the comparison aimed to assess the image quality and accuracy of each in both normal and pathological scenarios.

Chapter 2 of the thesis introduces the field of Nuclear Medicine, providing definitions, a brief history, and an overview of the radiopharmaceuticals used for both diagnostic and therapeutic purposes. Additionally, this chapter details the evolution of diagnostic nuclear medicine systems, exploring their historical development, key components, and operational principles.

Chapter 3 delves into nuclear cardiology, beginning with an explanation of the anatomy and physiology of the heart. The chapter then explores cardiac SPECT imaging, including the radiopharmaceuticals used in these studies, and continues with a discussion of imaging protocols, image processing techniques, and analysis methods. Cardiac PET imaging is also covered, offering insights into its role in cardiac diagnostics.

In Chapter 4, attention shifts to the design and construction of the realistic heart phantom. This chapter begins by discussing 3D printing technology and its most popular methods, before describing in detail the steps taken to create the phantom used in this study. The goal was to produce an anatomically accurate model that could be used to simulate a wide range of clinical conditions.

Chapter 5 outlines the experimental process in detail, including the acquisition protocols and imaging techniques used across the three SPECT systems. The chapter

also covers the processing software and methods employed for each system, examining the differences between the older, modern, and CZT technologies.

Finally, Chapter 6 provides a synopsis of the thesis and offers conclusions based on the findings of the experiments. Recommendations and potential future research directions are discussed, with the aim of further advancing the accuracy and applicability of cardiac phantom simulations in nuclear medicine.

CHAPTER 2nd

NUCLEAR MEDICINE

2.1 Introduction

Nuclear Medicine is a medical specialty involving the application of radioactive substances in the diagnosis and treatment of disease. Nuclear imaging, in a sense, is "radiology done inside out" because it records radiation emitted from within the body rather than radiation that is transmitted through the body from external sources like X-ray generators. In addition, nuclear medicine scans differ from radiology, as the emphasis is not on imaging anatomy, but on the function (physiology). For such reason, it is called a physiological imaging modality. Single Photon Emission Computed Tomography (SPECT) and Positron Emission Tomography (PET) scans are the two most common imaging modalities in nuclear medicine.

2.2 History

The history of Nuclear Medicine contains contributions of scientists across various disciplines, including physics, chemistry, engineering, and medicine. Its multidisciplinary nature renders pinpointing its exact birthdate a challenge for medical historians, though it likely lies between the discovery of artificial radioactivity in 1934 and the production of radionuclides for medical use by Oak Ridge National Laboratory in 1946.

The origins of this medical field trace back to the mid-1920s in Freiburg, Germany, where George de Hevesy conducted experiments with radionuclides administered to rats, revealing metabolic pathways and establishing the tracer principle. The genesis of Nuclear Medicine as a distinct specialty may be dated to 1936, when John Lawrence, dubbed "the father of nuclear medicine," visited his brother Ernest Lawrence at his radiation laboratory in Berkeley, California. Subsequently, John applied Phosphorus-32 in treating leukemia, marking the first application of an artificial radionuclide in patients.

Among the pivotal milestones in Nuclear Medicine's history is the discovery of artificially produced radionuclides by Frédéric and Irène Joliot-Curie in 1934. Their breakthrough, reported in *Nature*, built upon the earlier work of luminaries such as Wilhelm Roentgen, Henri Becquerel, and Marie Curie. Another significant moment came in 1946, with the publication of an article in the *Journal of the American Medical Association* by Dr. Saul Hertz and Dr. Arthur Roberts, detailing the successful treatment of Graves' Disease with radioactive iodine. This marked the public recognition of Nuclear Medicine's potential as a medical specialty.

The discovery and development of Technetium-99m in 1937 further propelled Nuclear Medicine forward. Its practical use became feasible with the development of

a generator system in the 1960s, making it the most utilized element in nuclear medicine imaging studies today. Widespread clinical adoption of Nuclear Medicine commenced in the early 1950s, facilitated by advancements in radionuclide knowledge and detection techniques. Pioneering works by Benedict Cassen and Hal O. Anger expanded the discipline into a full-fledged medical imaging specialty.

In the 1970s, Nuclear Medicine achieved official recognition as a medical specialty by the American Medical Association. Radiopharmaceuticals designed for diagnosing heart disease emerged, alongside the development of single photon emission computed tomography (SPECT), advancing nuclear cardiology. The 1980s saw further innovations with the invention of positron emission tomography (PET) and PET/CT imaging, revolutionizing oncology diagnosis, staging, and treatment monitoring. PET/CT imaging's growth was accelerated by administrative decisions allowing medical reimbursement for limited applications, leading to its widespread acceptance in recent years.

Looking ahead, the integration of fully integrated MRI/PET scanners represents the next frontier in nuclear medicine, promising enhanced diagnostic capabilities and treatment monitoring in oncology and beyond. (1)

2.3 Radiation sources – Diagnostic Radiopharmaceuticals

In Nuclear Medicine examinations, radiation sources in the form of radiopharmaceuticals are administered to patients via injection, ingestion, or inhalation. These radioisotopes possess chemical properties that enable them to accumulate in the specific organs targeted for imaging. Once within the body, these radiopharmaceuticals emit radiation, which is captured by specialized imaging systems such as γ -cameras or PET scanners. The resulting images provide valuable insights into the functional and physiological aspects of the organs under examination, aiding clinicians in diagnosis and treatment planning. Radioisotopes employed in diagnostic tests and treatments are either administered in their pure form or incorporated into preparations known as "cold kits." These kits earn their moniker "cold" because, in the absence of a radioisotope, the vials do not emit radiation. **Table 2.1** below enumerates the prevalent radioisotopes utilized in Nuclear Medicine diagnostic tests. Notably, over 90% of Nuclear Medicine examinations utilize chemical compounds containing Tc-99m. The table also includes the natural half-life of each radioisotope, denoted in the T_p column.

Radioisotope	Energy	T _p	Applications
Tc-99m	140 keV	6 hours	Diagnostic tests of bones, kidneys, liver, brain, heart, lungs, thyroid etc.
I-131	364 keV	8.04 days	Thyroid diagnostic tests, hyperthyroidism treatment and thyroid cancer.
I-123	159 keV	13.3 days	Thyroid diagnostic tests. Marking with other compounds.
Ga-67	93 keV 184 keV 300 keV 393 keV	3.2 days	Detection of inflammations and tumors.
Tl-201	67-82 keV 135 keV 167 keV	3.1 days	Imaging of myocardium, parathyroid glands.
In-111	171 keV 247 keV	2.8 days	Brain imaging, pituitary imaging, platelet labeling.

Table 2.1: Most commonly used diagnostic isotopes for SPECT examinations (2)

Furthermore, alongside the physical doubling time, there exist the biological and active doubling times.

The **biological half-life** (T_b) of a radiopharmaceutical refers to the duration over which half of its initial amount persists in the body, solely attributable to elimination via biological processes (e.g., excretion through urination).

The **active half-life** (T_e) of a radiopharmaceutical denotes the timeframe within which the administered radiopharmaceutical activity reduces by half in the body, and it relies on both the physical and biological half-lives, expressed as:

$$1/T_e = 1/T_p + 1/T_b$$

Active doubling time is always shorter than natural and biological.

2.4 Therapeutic Radiopharmaceuticals

In the preceding paragraph, we outlined the potential for acquiring diagnostic insights by detecting γ -photons emitted during the transition of radionuclides absorbed by the human body, selectively concentrating in specific organs owing to their distinct chemical properties. Given this, it becomes apparent that radionuclides-radiopharmaceuticals could serve therapeutic objectives provided they can be predominantly concentrated in a target tumor.

Procedures grounded on this principle are termed Nuclear Medicine treatments, diverging from external Radiation Therapy practices. An important advantage of Nuclear Medicine methods is the irradiation of small tumors, protecting the surrounding normal tissues.

The fundamental Nuclear Medicine treatment revolves around thyroid cancer, employing radioactive Iodine (I-131). Administered orally via capsules, I-131 preferentially accumulates in the thyroid. Through its β -decay, it generates photons and electrons. Unlike in diagnostic procedures, treatment focuses on the emitted electrons. These electrons, with their limited tissue penetration, deposit energy locally, effectively eradicating cancer cells while inducing minimal harm to surrounding healthy tissues.

The **Table 2.2** below gives some of the therapeutic radioisotopes as well as their respective delivery activities.

Radioisotope	T_p	Treatment	Activity (mCi)
I-131	8 days	Differentiated thyroid cancer	100-150
Sr-89	51 days	Palliative treatment of bone metastases	4
Sm-153	47 hours	Palliative treatment of bone metastases	70
Re-186	90 hours	Palliative treatment of bone metastases	35
Y-90	64 hours	Non Hodgkins lymphoma, liver metastases hepatocellular carcinoma, neuro-endocrine tumours	35
Lu-177	6.7 days	Prostate cancer, neuro-endocrine tumours	100-250

Table 2.2: Most commonly used therapeutic isotopes (3)

2.5 Diagnostic Nuclear Medicine systems

2.5.1 History

The first gamma camera, developed in 1957 by Anger Oscar Hal, an American electrical engineer and biophysicist at the Donner Laboratory of the University of Berkley California, is the fundamental imaging device in Nuclear Medicine used for diagnostic imaging. Anger's invention, known as the "Anger-camera," **Figure 2.1** forms the basis for modern gamma cameras.



Figure 2.1: Oscar Hal Anger next to “Anger camera” (4)

2.5.2 Basic principles of analog γ -cameras

The gamma camera system comprises the detector head with its electronics, examination bench, control interface, and a computer responsible for image acquisition and processing. Within the detector head is the detection system containing the NaI crystal doped with thallium (Tl) and the photomultipliers, all surrounded by lead shielding to minimize ambient radiation interference without compromising the image quality. This system's capability to fully rotate around its axis and around the patient's body enables the acquisition of both tomographic and whole-body images, respectively. While modern gamma cameras with multiple heads (**Figure 2.2**) accelerate image acquisition, the fundamental principle of operation remains unchanged from early systems like the Anger camera. The NaI crystal's flat surface is positioned as close as possible to the patient's surface, aligned with the organ of interest. Following the administration of a radiopharmaceutical, emitted photons penetrate the patient's body, interacting with the NaI crystal to produce visible light. Photomultipliers detect this light, converting it into electrical pulses. Depending on the relative intensity of the signal of each photomultiplier it is possible to determine the position where the photon hit the crystal (spatial information). Then the sum of the electrical pulses, (the height of which is proportional to the energy of the photon that hit the crystal) is sent to the pulse height analyzer, which allows only

the pulses with a height equal to the one selected by the operator to pass. This filtered pulse is recorded by the PC and with appropriate software the image is captured on the screen. This image is actually the two-dimensional projection of the distribution of the radiopharmaceutical in the area under consideration.

Subsequently, the most important of the individual parts of the analogue γ -cameras will be thoroughly analyzed



Figure 2.2: Mediso Anyscan TRIO SPECT

2.5.2.1 NaI(Tl) crystal

It is the most critical and at the same time the most expensive single part of the γ -camera system. The NaI(Tl) crystal has a thickness of 0.6-1.8 cm and a shape either circular (mainly for older systems and cameras exclusively for imaging the thyroid gland) with a diameter of 25.4-50.8 cm, or rectangular. When a photon interacts with the crystal, a momentarily visible foe (scintillation) is produced and for this reason the crystal is called a scintillator and the examination a scintigram.

2.5.2.2 Photomultipliers (PMTs)

Very carefully and very precisely placed with the help of a special silicone gel on one side of the crystal are connected up to 94 multipliers (in veterinary imaging systems

there may be more) mainly in a polygonal or circular arrangement (**Figure 2.3**) depending on the type of system. In this special gel that stabilizes the photomultipliers on the NaI crystal, the generated visible quanta or scintillations pass almost without loss to the photomultipliers. These in turn convert the sparks into electrons and by extension into an electrical pulse. These electrons create at the output of the photomultiplier an electric pulse whose height is proportional to their number and also proportional to the number of scintillations incident on the NaI crystal. The pulses of all the photomultipliers are then summed and give a pulse, the height of which is proportional to the energy of the photon that after its prolapse was absorbed by the NaI crystal. In this way the photon energy information is obtained and it can be distinguished whether it is primary (required in medical imaging) or scattered.



Figure 2.3: Different types of photomultipliers (PMTs)

However, in addition to the information of the energy, the information of the location of the appearance of the spark on the crystal is also required. Each photomultiplier sees each scintillation generated with different intensity depending on where the scintillation occurs. Thus, by the law of photometry, the photomultiplier that is closer to the scintillation point will receive a greater intensity of light and therefore will record a greater pulse. Finally, with the use of special lead linearity phantoms during the calibration process and with appropriate software, the points are mathematically processed and the point of the crystal where the photon hit is determined with relative accuracy.

2.5.2.3 Electronic systems for amplification, separation and analysis of electrical pulses

The output pulses from the photomultipliers are initially weak and lack sufficient height for easy measurement. Consequently, there's a requirement to amplify them without altering their relative ratios. This amplification is accomplished through the use of specialized electric circuits known as analog linear amplifiers. Through proportional or linear amplification, the pulses retain their original height differences in proportion to one another.

It's essential to note that not all pulses originate solely from the photoelectric absorption of primary photons. They also result from the absorption of other photons, notably those from Compton scattering, along with background radiation. Therefore, it's crucial to separate and eliminate unwanted pulses.

The task of regulating pulse heights is managed by the pulse height analyzer. It receives the summed pulse from the photomultiplier outputs. This analyzer, an electrical circuit, is preset by the operator to filter out pulses below a desired height. Practically, this configuration establishes an upper and lower pulse height limit known as the energy window. This window accounts for errors and statistical variations in electrical systems, acknowledging that not every detected primary photon yields an exact pulse height.

For instance, in experiments involving the most commonly used Nuclear Medicine isotope Tc-99m emitting 140 keV photons, the operator sets the pulse height that corresponds to an energy of 140 keV +/- 10% to pass through the analyzer unimpeded. Consequently, pulses from scattered photons exceeding this selected window height are effectively blocked.

Following separation and analysis, the pulses are directed to various electronic systems, notably rhythmometers and downscale devices. Rhythmometers track the numerical fluctuations in the concentration of the radioactive material over time, indicating the pulse generation rate. Downscale systems individually score each pulse passing through the window, progressively adding them to the cumulative hit count. These systems incorporate automatic mechanisms to cease measurements once a predetermined count is reached, signaling the examination's completion.

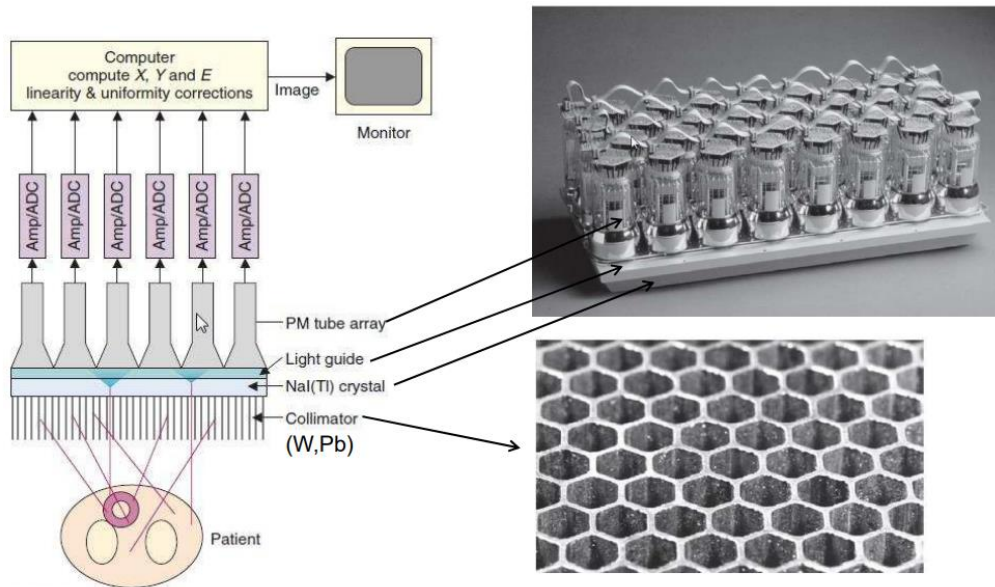


Figure 2.4: γ -camera main components (5)

2.5.2.4 System operation

The operation of the γ -camera is managed by a PC equipped with suitable software, facilitating the selection and adjustment of examination parameters. Within the PC, signals from the head and electronic systems undergo fully automated processing, culminating in the creation of the examination image (**Figure 2.5**). Additionally, the image can be edited to emphasize optimal diagnostic results.

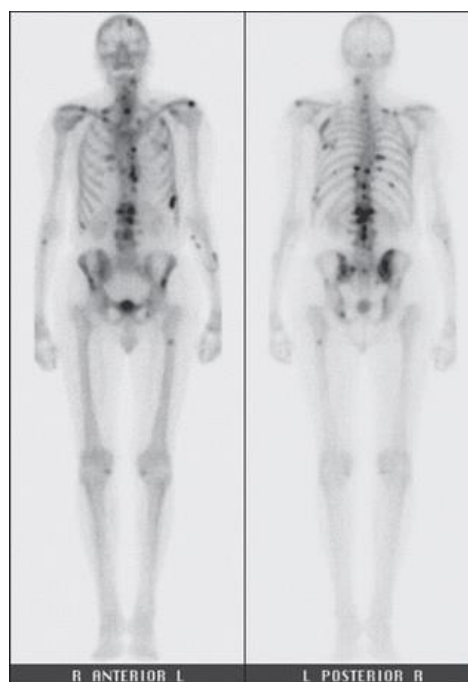


Figure 2.5: Tc-99m Wholebody bone scintigraphy

2.5.2.5 Collimators

It's typical for photons, having undergone scattering (Compton effect) within the patient's body, to reach the γ -camera's crystal. These scattered photons carry inaccurate position information and thus need to be eliminated. One accessory aiding in their removal is the collimator. Typically made of lead (Pb) and several centimeters thick, the collimator features numerous holes. These holes allow primary photons emitted in a specific direction to strike the crystal. Depending on the examination and radionuclide photon energy, various types of collimators are employed with each γ -camera. The primary ones (**Figure 2.6**) include:

- **Pinhole collimator:** Conically shaped with a height of approximately 25 cm, photons pass through the top of the cone. This collimator is used for examinations necessitating magnification of small structures like the thyroid.
- **Multi-hole collimator:** Featuring parallel axes, this collimator prevents photon passage between holes by varying lead thickness. It comes in three thicknesses:
 - LE (Low Energy) for isotopes like Tc-99m, Tl-201, and I-123.
 - ME (Medium Energy) for isotopes such as Ga-67.
 - HE (High Energy) for high energy isotopes like I-131.

The size of the object remains unchanged with this collimator, making it suitable for most examinations.

- **Multiple converging holes collimator:** With holes focused at a point around 50 cm away, this collimator magnifies the image of the organ being examined, primarily used for imaging small organs but less frequently in modern systems.
- **Multiple diverging holes collimator:** Unlike the former, this collimator converges holes towards the side of the crystal, resulting in object image reduction. It's employed for imaging large organs, albeit sparingly in modern systems.

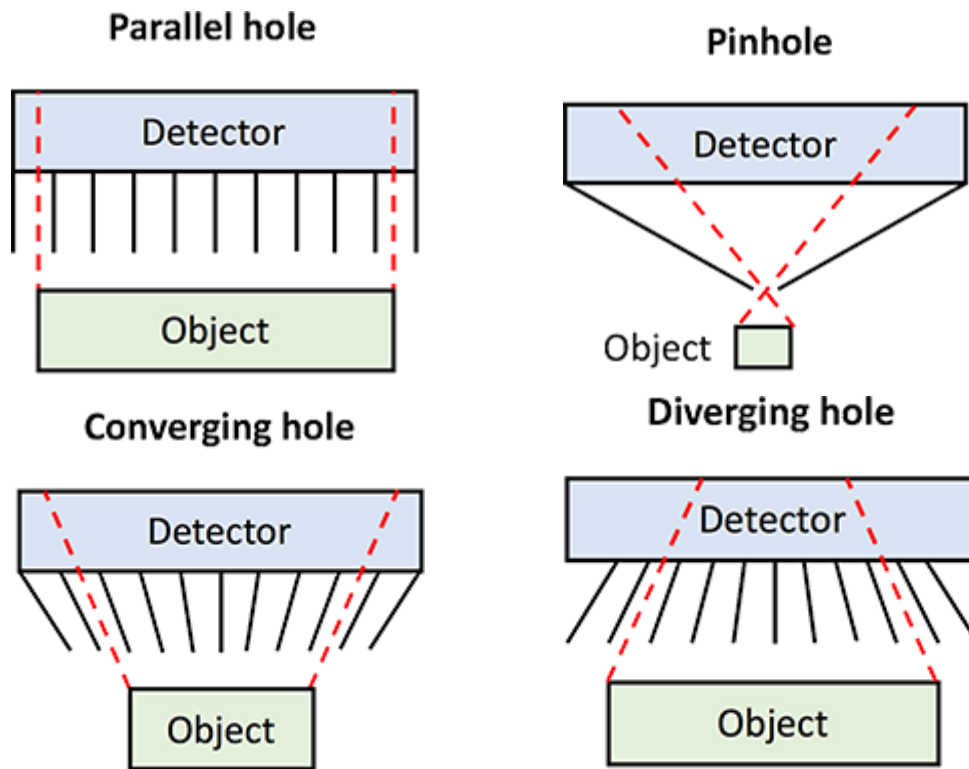


Figure 2.6: Primary γ -camera Collimator types

2.5.2.6 Image creation

The γ -camera crystal's surface serves as the defining space for the coordinates of photon impacts. This scintillation data is stored in a computer in a two-dimensional table mirroring the crystal's shape, with individual elements termed pixels. The table's size, or dimension, along with its pixel depth, directly impacts image resolution, because larger dimensions yield higher resolutions. Operators select table dimensions based on the examination type, commonly opting for sizes like 32x32, 64x64, up to 1024x1024. Once the examination concludes, the results are displayed on a PC screen. Imagine this screen as a grid, with each square representing a pixel and displaying recorded values. To enhance readability for observers, pixel values are mapped to shades of gray through a linear relationship, forming the diagnostic image. When printing onto film or paper, pixel values are mapped to optical density instead of grayscale. It's important to note that the printing process in Nuclear Medicine, unlike Radiodiagnosis, doesn't involve radiation exposure, because special printers are used for this purpose. Despite the printing differences, the concept of optical density remains consistent across both fields.

2.5.2.7 Evaluation of γ -camera operation

Several factors influence the γ -camera's operation, impacting the resulting image, examination duration, and patient dose. These factors often interact, such that improving one may compromise another. Here are the primary evaluation factors of the γ -camera:

- **Intrinsic or internal detection efficiency:** This refers to the ratio of detected photons to photons incident on the crystal. It relies on the crystal's thickness; thicker crystals enhance photon detection by increasing interaction probability.
- **System Detection Performance:** This factor combines internal performance with collimator involvement. It measures detected photons relative to photons incident on the collimator surface. Notably, system detection performance is lower than internal performance and is influenced by factors affecting internal efficiency and collimator performance.
- **Dead time:** At high sampling rates, electronic systems may merge two photons closely detected in time into one event, resulting in missed detections. Dead time refers to the period required for the system to reset after detecting a scintillation, during which subsequent scintillations may go unrecorded.
- **Intrinsic or internal spatial resolution:** This denotes the crystal and electronics' precision in pinpointing scintillation locations. Internal spatial resolution depends on crystal thickness and statistical variations in scintillation recordings by photomultipliers. Thicker crystals pose challenges due to photon diffusion, while scintillation location determination relies on comparing photomultiplier pulse heights.
- **System spatial resolution:** This combines internal spatial resolution (R_i) and collimator spatial resolution (R_c). System resolution (R_s) is determined by the lesser of these components, as per the relationship:

$$R_s = \sqrt{R_i^2 + R_c^2}$$

As mentioned at the beginning of the section, these factors affect the image and dose to the patient. For example, if the efficiency of the system is low, then the number of photons incident on the detector should be increased in order to increase the photons detected and create an acceptable image. This entails increasing the activity given to the patient or lengthening the time of the examination. (2)

2.5.2.8 Image quality

Image quality in Nuclear Medicine is described in the same way as in Radiology. Contrast, spatial resolution and noise are defined in a similar way although they refer to completely different processes.

- **Contrast:** Defined as the difference in intensity or optical density between two regions of different radionuclide concentration. Optical density is the quantity that expresses the amount of darkening in the film. Contrast is reduced by the presence of scattered photons that were not cut off by the guide or pulse height analyzer, background radiation (from structures that have bound radiopharmaceutical and lie below or above the tissue to be imaged), and the film.
- **Spatial resolution:** In addition to the aforementioned, it is worth adding the degradation of resolution, due to the movement of the patient and the examined organs (heart, lungs) but also the choice of the dimensions of the recording table.
- **Noise:** Image noise has two components. Structure noise and random or quantum noise. Structure noise originates from adjacent structures that have taken up radiopharmaceutical and are visible in the image, reducing the diagnostic information from the probe. In contrast, quantum noise is due to the statistical variation of the detected photons and the statistical nature of the radioactive decay phenomenon. In an image of homogeneous radioactive emission, ideally, each pixel should have the same number of photons N recorded.

2.5.2.9 Tomographic γ -camera (SPECT)

The image obtained from a γ -camera is a two-dimensional projection of a three-dimensional distribution of the radiopharmaceutical, within the patient's body.

The acquisition of the information of the third spatial dimension is achieved with the tomography methodology. Its application system is called SPECT (Single Photon Emission Computed Tomography). In essence, the SPECT camera is the technological evolution of the Anger camera mainly at the level of software and mechanical rotation of the head. A SPECT system consists of one or more heads with the possibility of automatic and programmable rotation around the patient, in a desired radius and speed of rotation.

To perform the tomography, images of the distribution of the radiopharmaceutical must be taken at various angles. In practice these images are common two-dimensional images obtained by programmed automatic rotation of the SPECT system head or heads. Each shot is called a projection of the radioactivity distribution. The basic process in projection is the summation of radioactivity along imaginary rays

(projection rays), which start from the detector and pass through the radioactive source. The sum of the radioactivity along a projection ray is the ray sum. The collimators used in imaging determine the relative origin of the projection rays.

When processing the data to produce the cross-sections or 3D representation of the target organ, corrections are made for photon absorption and changes in sensitivity and resolution along the projection rays. The reconstruction of the tomographic image involves two stages. Backprojection and the correction of backprojection errors. Backprojection is a process in which projection data is re-entered into space along the projection rays from which it came. Backprojection also determines the geometry on which the tomographic images are composed. All processing is done with sophisticated computer systems and numerical algorithms, which use approximate methods and apply corrections using special mathematical filters and applications of Fourier theory. In modern SPECT systems, there is the possibility, with special processing of the data from the received views, to produce transverse, sagittal or coronal sections or even sections along anatomical axes of the examined organ or system, such as e.g. the heart.

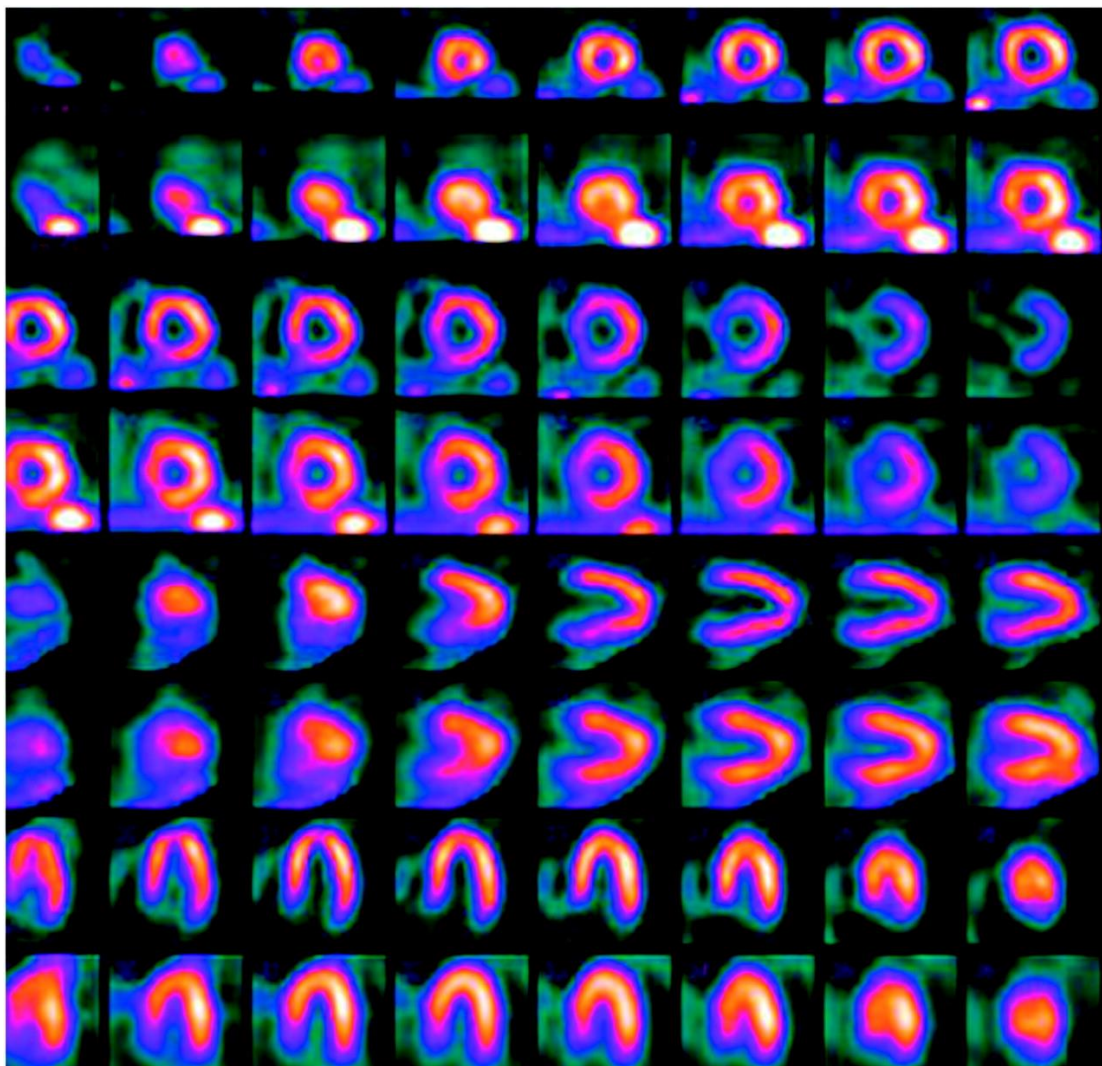


Figure 2.7: Cardiac SPECT scintigraphy typical views (6)

As mentioned above, modern γ -cameras perform both static and dynamic, as well as tomographic images with one to three heads. The latest development (beyond the emergence of CZT detector technology which will be discussed below) is SPECT systems, capable of functioning also as PET, in which there is an integrated CT scanner with a low-energy X-ray lamp. The purpose of these systems is to combine the information functions of scintigraphy with the anatomical details of CT by fusing the two images, to increase the diagnostic information from a study.



Figure 2.8: Mediso Anyscan SCP (SPECT/CT/PET)

2.5.3 Basic principles of digital γ -cameras

The emergence of Cadmium Zinc Telluride (CZT) technology within Single Photon Emission Computed Tomography (SPECT) systems signifies a significant departure from the conventional employment of sodium iodide (NaI) detectors. While the NaI technology has endured since the era of the Anger camera with minimal evolution, CZT technology represents a transformative leap in detector construction and efficacy. Characterized by superior energy resolution, heightened sensitivity, and enhanced spatial resolution, CZT-based SPECT systems bring a new era of innovation and refinement in nuclear imaging practices.

2.5.3.1 CZT detector construction and function

CZT detectors undergo a fabrication process involving the deposition of ultra-thin metalized electrode geometries onto their surfaces. These electrodes are subsequently electrically biased, creating a distinct electrical potential gradient within the detector volume. Upon interaction with ionizing radiation, the CZT crystal generates numerous pairs of electrons and holes, the quantity of which correlates with the energy of the incident radiation.

Following their creation, the negatively charged electrons and positively charged holes migrate towards the oppositely charged electrodes, where they are captured and collected. The resultant charge pulse is then detected by a preamplifier, which generates a voltage pulse proportional to the energy of the incoming photon.

Subsequently, the signal is channeled into a shaping amplifier, which converts it into a Gaussian pulse and enhances its magnitude. This processed signal can then be directed into a standard counting system or Multi-Channel Analyzer (MCA) to construct the characteristic spectrum for the incoming photons.

To optimize efficiency and reduce the footprint of the readout electronics, CZT-based detectors are often coupled with an Application-Specific Integrated Circuit (ASIC). This coupling facilitates compactness and cost-effectiveness, streamlining the operation of the detector system. (7)



Figure 2.9: CZT module basic components (8)

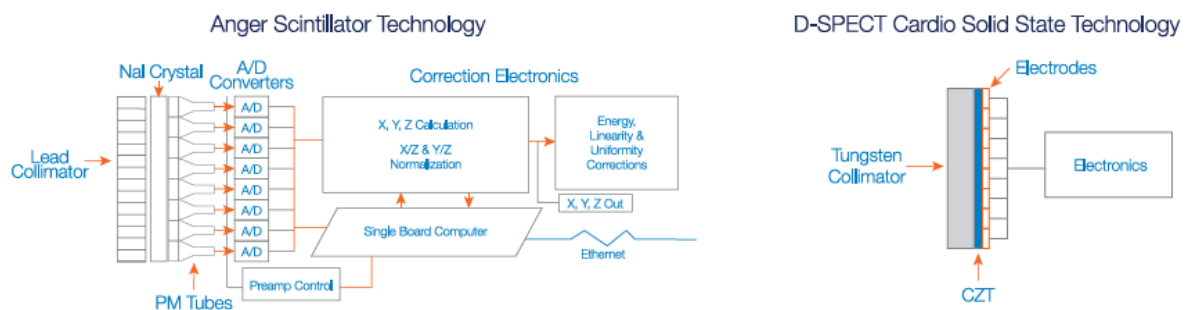


Figure 2.10: Diagram comparison between NaI and CZT technology γ -cameras

2.5.3.2 Advantages of digital SPECT systems

The utilization of CZT technology in SPECT systems presents a new era in nuclear medicine, offering a plethora of advantages over traditional NaI detectors. Chief among these advantages is the superior energy resolution of CZT detectors, enabling precise discrimination of gamma ray energies and enhancing the accuracy of imaging studies (**Figure 2.11**). Additionally, CZT detectors exhibit heightened sensitivity to gamma rays, allowing for improved detection of low levels of radioactivity and reducing imaging times for enhanced patient comfort. Moreover, CZT-based SPECT systems boast higher spatial resolution, enabling the visualization of fine anatomical details with remarkable clarity. Furthermore, CZT technology facilitates the development of compact and more simplistic designs, streamlining system operation and maintenance. Overall, the adoption of CZT technology in SPECT systems represents a significant advancement in nuclear medicine, providing clinicians with unprecedented imaging capabilities and diagnostic precision.

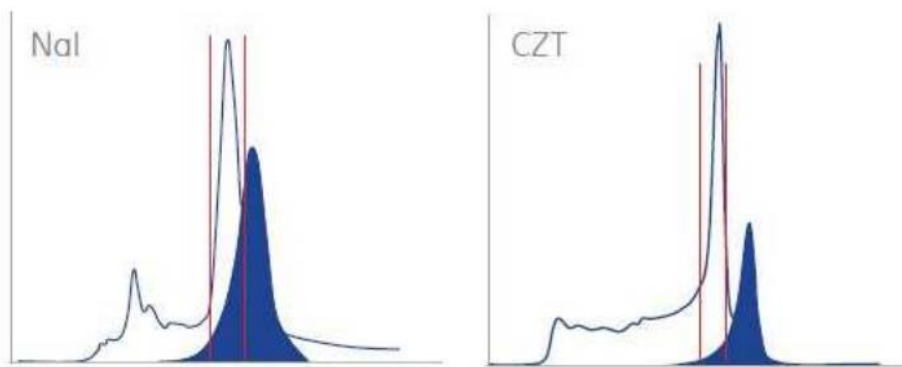


Figure 2.11: Overlay of ^{99m}Tc and ¹²³I spectra, showing greater crosstalk between the two peaks for the NaI detector with its poorer energy resolution and wider energy window (9)

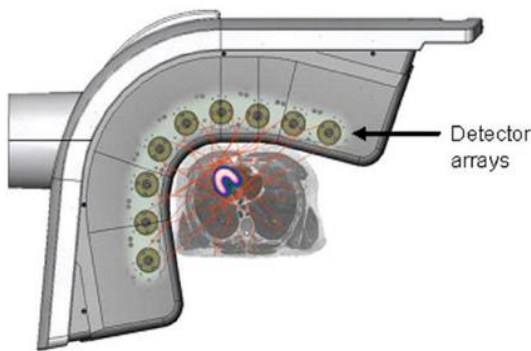
2.5.3.3 Types of digital SPECT systems

As mentioned above, CZT technology has revolutionized the landscape of SPECT systems, giving rise to a diverse array of advanced imaging platforms catering to various clinical needs. One such system is the Spectrum Dynamics D-SPECT (**Figure 2.12**), a cutting-edge cardiological imaging solution renowned for its exceptional sensitivity and spatial resolution. Leveraging 6 to 9 CZT detector blocks, the D-SPECT system enables high-quality myocardial perfusion imaging with unprecedented detail and accuracy, facilitating the diagnosis and management of cardiovascular conditions, including the calculation of the Coronary Flow Reserve (CFR) by the coronary artery. This information can be crucial to diagnose multi-vessel and microvascular disease which used to be only available for PET. Another notable CZT-based SPECT system is the GE CZT SPECT, which combines the latest innovations in detector technology with state-of-the-art imaging algorithms. This system offers clinicians unparalleled flexibility and performance, allowing for comprehensive imaging studies across a wide range of medical specialties.

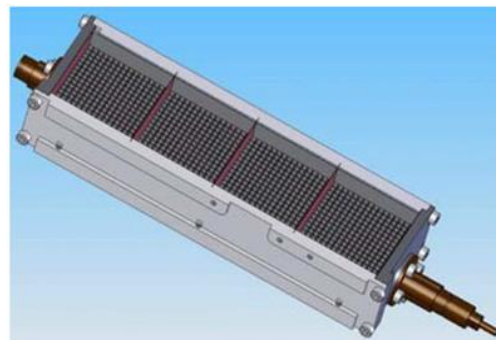
Additionally, the Spectrum Dynamics Veriton SPECT/CT system (**Figure 2.13**) represents the pinnacle of CZT-based imaging technology, seamlessly integrating CZT detectors with computed tomography (CT) for hybrid functional and anatomical imaging. By combining the sensitivity and resolution of CZT detectors with the detailed anatomical information provided by CT, the Veriton system delivers comprehensive diagnostic insights for enhanced patient care. Collectively, these CZT-based SPECT systems exemplify the transformative potential of advanced detector technology in revolutionizing nuclear medicine practice.



(a)



(b)



(c)

Figure 2.12: (a) Spectrum Dynamics D-SPECT cardiological System. (b) Internal D-SPECT view with 9 detector columns. (c) D-SPECT detector column (10)

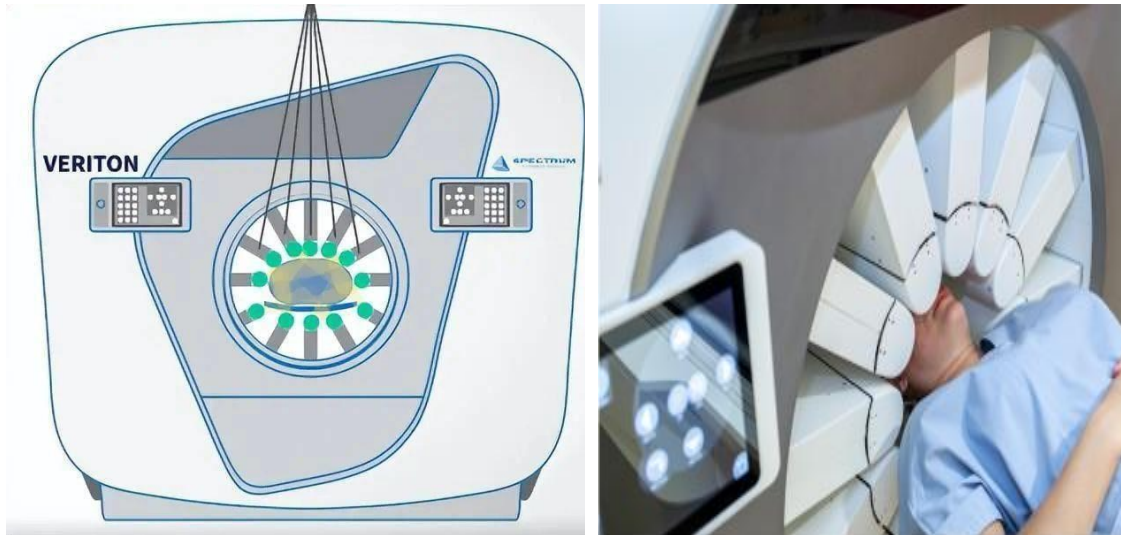


Figure 2.13: Spectrum Dynamics Veriton SPECT/CT (11)

2.6 PET and PET/CT systems

2.6.1 Importance of Cyclotrons

In 1930 Ernest Lawrence and his team in Berkeley, California, developed the idea of accelerating particles using a device called a cyclotron, which consisted of two D-shaped magnets, to generate higher energy protons and deuterons for bombarding elements and studying atomic nuclei. Their initial cyclotron had 4-inch magnets, with later versions featuring 10, 37, and 60-inch magnets. Unbeknownst to them, between 1930 and 1934, they had been producing radioactive cobalt, copper, and other radionuclides through the bombardment of metal components in their cyclotrons. The 1934 discovery of artificial radioactivity by Joliot and Curie was disappointing for the Berkeley team, as they missed the chance to be the first to show that nearly any element could be made radioactive. They missed this discovery because their cyclotron and radiation detection instruments shared the same power supply, which was turned off simultaneously every evening.

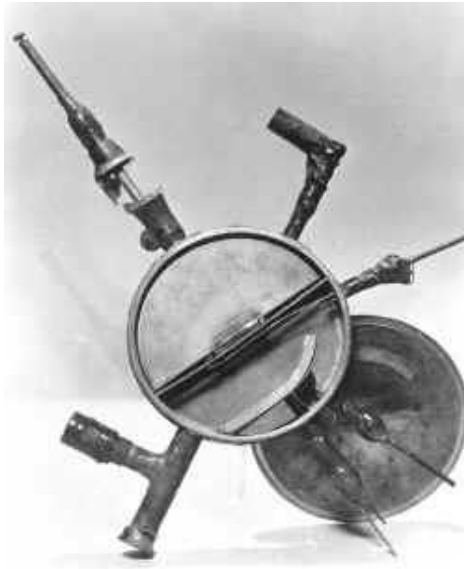


Figure 2.13: Ernest Lawrence's original 11 cm cyclotron (12)

As their cyclotrons grew larger, the Berkeley group could produce and identify significant quantities of artificial radioisotopes such as Carbon-11, Nitrogen-13, Oxygen-15, and Fluorine-18, which later became vital to biomedical research. In the 1930s, recognizing the importance of these new radioelements for applying the tracer principle first introduced by Hevesy with naturally occurring radiotracers, scientists from various fields gathered in Berkeley. By 1938, Lawrence and his colleagues designated their fourth cyclotron a "medical cyclotron."

The history of nuclear medicine is marked by the creation of increasingly refined radiotracers for examining the human body. This began with studies on photosynthesis in plants using Carbon-11 and investigations into carbon monoxide metabolism in humans, along with using Phosphorus-32 to further understand the dynamic state of body constituents.

During wartime research from the late 1930s to the 1950s, the development of the nuclear reactor shifted focus away from the cyclotron. Initially supported by private sources like the Rockefeller Foundation, Lawrence's work gained substantial government backing with the development of the Calutron for purifying Uranium-238. In 1939, Niels Bohr visited Princeton University and learned about the recent experiments by Hahn and Strassmann, which showed that neutron bombardment of uranium resulted in nuclear fission, producing barium. This discovery led Bohr and Fermi to conceive the idea of a chain reaction, calculating that the fission of a kilogram of Uranium-235 could release energy equivalent to 20,000 tons of TNT, highlighting its military potential. Thus, nuclear weapons, nuclear power, and nuclear medicine became interlinked.

The invention of the nuclear reactor by Fermi and his team at the University of Chicago enabled the production of large quantities of Carbon-14, tritium, phosphorus-

32, and other radionuclides, significantly advancing biochemistry. The longer half-lives of these tracers made them more available, affordable, and usable compared to cyclotron-produced radionuclides. Despite its short half-life of 20 minutes, Carbon-11 lost appeal, while Carbon-14 and tritium, which emit beta particles with a short range in tissue, could not be used for studying regional biochemistry in living bodies. It took three decades for interest in cyclotrons for biomedical research to revive due to the need to measure in vivo regional biochemistry.

Initially, nuclear medicine physicians focused on imaging organs like the liver and spleen, which conventional x-rays could not visualize. Radionuclides within the body could reveal the structure and defects in these organs. Technetium-99m, with its ideal physical properties for in vivo imaging, became a popular choice. However, Technetium-99m is a man-made element not found in the human body. Organic chemistry relies on carbon, and the only photon-emitting radionuclide of carbon is Carbon-11, which necessitates a cyclotron for production. The advent of competing imaging methods like computed tomography (CT) and magnetic resonance imaging (MRI) shifted the focus of nuclear medicine back to biological elements like carbon-11, fluorine-18, nitrogen-13, and oxygen-15. (13)

2.6.2 History of PET and early designs

Positron emission tomography (PET) is the most specific and sensitive method for imaging molecular interactions and pathways in the human body. This specificity is due to the variety of positron-emitting radionuclides that can label specific biomarkers, biochemicals, and pharmaceuticals without disrupting their biological functions. The radiation from a radiolabeled tracer is unique to that tracer and can be detected against the low natural radiation background. However, it is necessary to correct for scatter effects and photon attenuation by tissue, fundamental aspects for which George de Hevesy received the Nobel Prize in Chemistry in 1943. The sensitivity of PET, which detects low molecular masses of the tracer, relies on producing labeled compounds with high specific activity and detecting positron-emitting nuclei using coincidence counting to capture the paired annihilation photons.

Over the past 60 years, PET technology has evolved from single pairs of detectors for planar imaging to advanced scanners with arrays of detector elements. The first total-body PET scanner, the EXPLORER, under construction, features a 2-meter axial length and 560,000 detector elements, significantly increasing sensitivity compared to commercial scanners. The goal has always been to improve sensitivity to maximize acquired counts per radiation dose to the patient and achieve high spatial and temporal resolutions. Key developments include advancements in scintillator crystals, photodetectors, acquisition electronics, data processing, and image analysis. Since 2001, PET scanners have been combined with anatomical imaging devices such as CT and MR scanners, providing high-resolution anatomical frameworks accurately coregistered with functional PET images and improving image quality.

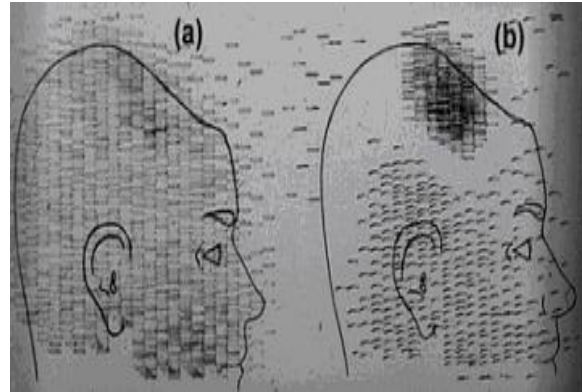


Figure 2.14: (left) The first coincidence scanner – (right) Acquired image from the first coincidence scanner (14)

Systematic advances in PET technology have increased sensitivity by a factor of 40 from early single-slice designs to modern commercial scanners. Each phase of this progression has come at additional cost, offset by increased signal acquisition per unit cost, leading to new clinical and research applications. Since Medicare began reimbursing some cancer indications in 1998, commercial competition among PET vendors has helped contain development costs. The introduction of new PET technology is expected to meet growing demands by increasing sensitivity for whole-body imaging, leading to new clinical and research applications and realizing PET's full potential. Innovations from physicists and engineers will be crucial in exploiting PET-based molecular imaging's unique capabilities.

Early PET developments include Chesler's transmission imaging method using Ga-68, avoiding distortion in reconstructed images and allowing quantitative values for tissue concentrations of radioisotopes. The St. Louis group minimized unwanted coincidences in their scanner design, enabling quantitative measurements of regional tissue concentrations of positron-emitting radionuclides. This capability of PET to make absolute in vivo measurements noninvasively is a significant strength for clinical research and healthcare.

The collaboration between Phelps, Hoffman, Douglass, and Williams resulted in the commercial single transaxial plane PET scanner known as the ECAT I, leading to widespread adoption and numerous clinical research programs using standardized, commercially supported PET scanners. After relocating to UCLA, Hoffman and colleagues published a series of papers on the criteria for achieving true quantification using PET. Their next design featured a ring-based geometry, which required innovations due to the size and spacing of the detector elements to obtain sufficient spatial sampling. This was achieved through a half-crystal rotation and a wobble of the entire detector ring. The wobble mode, developed by Eriksson at the Karolinska Hospital in Stockholm, involved moving the center of the tomograph to four specific

locations around a 1-inch diameter circle. Each wobble position acquired a complete emission data set, allowing different lines of response to be sampled throughout the field of view. The four sets were then combined into parallel projections with higher projection sampling than any single acquisition. An alternative approach was the "clam shell" design by Derenzo at the Berkeley Laboratory in California.

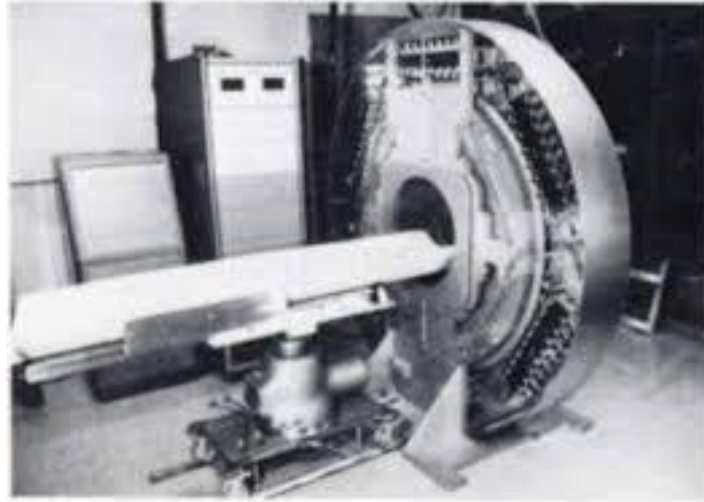


Figure 2.15: PET with multi-rings geometry – UCLA 1970s (15)

These early designs used one-to-one coupling between the scintillation crystal and photodetector, typically a photomultiplier tube, which complicated the assembly of multiple transaxial planes for extended axial coverage. Despite this, the NEUROECAT was successfully completed, featuring three octagonal arrays of bismuth germanate (BGO) detectors that imaged five transaxial planes simultaneously. This was followed by the ECAT III, designed primarily for cardiac imaging, which incorporated three rings of detectors. The smaller crystal size in the ECAT III provided sufficient in-plane sampling, eliminating the need to rotate or wobble the ring. Eriksson, in collaboration with the Scanditronix Company, pioneered the phoswich design for higher in-plane resolution. This involved coupling two scintillation crystals, one BGO and one gadolinium orthosilicate (GSO), to a single photomultiplier, allowing the specific crystal to be identified based on their different light output characteristics. This detector configuration was incorporated into a whole-body scanner design.

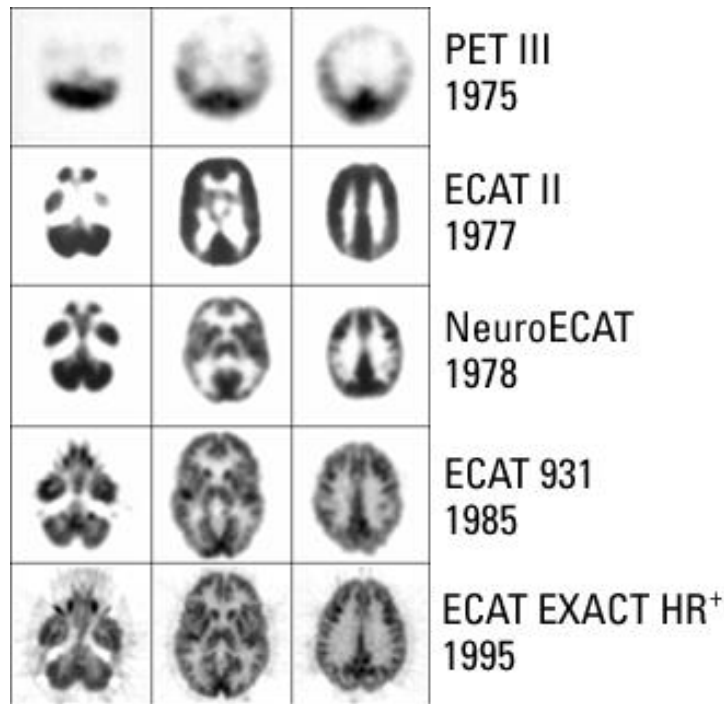


Figure 2.16: Image evolution in early PET systems (16)

Crystal material	Light yield (photons/MeV)	Emitted light wavelength (nm)	Light emission decay time (ns)	Density (g/cm ³)	Effective atomic number	Refractive index	Energy resolution at 511 keV (%)
NaI(Tl)	38000	415	230	3.7	51	1.85	10
BGO	9000	480	300	7.1	75	2.15	20
LSO	26000	420	40	7.4	66	1.82	15
LYSO	32000	430	40	7.1	66	1.82	12
GSO	13000	440	50	6.7	59	1.85	15
LaBr ₃	60000	370	25	5.3	47	1.9	10
LuAP ^a	12000	365	18	8.3	65	1.94	7

Table 2.3: Characteristics of the most important scintillator crystals used in PET (17)

2.6.3 Modern Commercial PET Systems

Due to the finite size of photomultiplier tubes, one-to-one coupling was physically limiting and expensive for improving volume spatial resolution and axial coverage. As patients receive a whole-body radiation dose regardless of the imaged area, extending axial coverage enhances the use of emitted photon flux and overall system sensitivity. The limitation of one-to-one coupling in ring systems was addressed by using light-sharing between photomultipliers, a method pioneered by Anger in the gamma camera and later adopted in the MGH positron camera. Utilizing this technology, Casey and Nutt developed a block detector with four photomultipliers coupled to an 8×4 array of BGO crystal elements. BGO, denser and non-hygroscopic

compared to sodium iodide, was easier to assemble into a mosaic array. The principle of the block detector is illustrated for an 8×8 array coupled to four photomultipliers.

The first commercial block-based PET scanner, featuring a 10-cm axial length and 15 transaxial-plane read-out, was acquired by the Hammersmith group in London. It included eight retractable rings of Ge-68 for transmission scanning, also used for daily detector checks. Initial designs with multiple detector rings used thin tungsten sheets (septa) between rings to restrict photon detection to specific planes, imaging a 3-D volume as 2-D parallel transaxial planes. While septa reduced system dead time and random coincidences, they also resulted in low sensitivity, challenging the collection of high-quality time course data for kinetic sampling. Removing the septa from the first block detector scanner at Hammersmith improved sensitivity and enabled fully 3-D reconstructions, leading to PET scanners capable of recording data in both 2-D (septa-in) and high-sensitivity 3-D modes. The first such scanner with retractable septa was installed at Hammersmith Cyclotron Unit in 1991, specifically for brain imaging.

To leverage the increased sensitivity of 3-D data collection, a lower-cost scanner was developed with 40% of the detector ring, rotating around the patient to collect all tomographic views. This design was commercialized in the early 1990s as the ECAT ART. However, with Medicare reimbursement for PET studies in 1998, interest in low-cost scanners waned in favor of more expensive full-ring scanners offering faster imaging times and higher throughput. Rotating gantry PET technology was later combined with spiral x-ray CT to produce the first PET/CT prototype.

Throughout the 1980s and 1990s, BGO was the main scintillator used in PET scanners by CTI PET Systems and General Electric. The block design by Casey and Nutt evolved into various crystal matrices coupled to four phototubes. The ECAT HR 47, with an 8×7 crystal matrix, became a clinical PET workhorse, while the ECAT HR+ featured 8×8 crystals for high-resolution brain and whole-body imaging. The ECAT EXACT3D, evaluated at Hammersmith Hospital Cyclotron Unit, comprised six rings of HR+ detector blocks, operating fully in 3-D with a 25-cm axial field-of-view and 10% sensitivity for a central point source. Attenuation correction was performed using a rotating Cs-137 source.

Today, all commercial PET scanners operate in high-sensitivity 3-D mode without septa. The 3-D scatter fraction can exceed 35%, necessitating sophisticated scatter correction models. Early 2-D scatter correction techniques evolved into 3-D methods, like the convolution–subtraction method and the single scatter model, improving the accuracy of scatter distribution estimates.

The search for better scintillators led to the discovery of lutetium oxyorthosilicate (LSO), superior to BGO for PET imaging. The first commercial LSO PET scanner, the ECAT ACCEL, appeared around 1999. LSO is also used in the high-resolution research tomograph (HRRT) for brain imaging. Some vendors adopted a derivative, LYSO, while Philips Healthcare introduced GSO-based scanners. These new scintillators offered better energy resolution, finer detector block subdivisions, lower scatter fractions, and improved timing resolution, resulting in higher noise equivalent count rates, especially for large patients.



Figure 2.17: ECAT ACCEL – PET system

A significant advantage of LSO is its fast timing, enabling time-of-flight (TOF) measurements that provide additional positioning information, improving statistical gain and image noise reduction. TOF PET, reintroduced with LSO, appeared in scanners like the Philips Gemini TF and Siemens Biograph mCT, demonstrating improved lesion detectability, especially in large patients. Modern PET scanners with fast scintillators integrate TOF into the reconstruction algorithm.

Advances in image data presentation have also increased PET adoption. Coregistration of PET and MRI scans aids in interpreting brain anatomy, while whole-body FDG18 scans, presented as integrated longitudinal sections, facilitate cancer staging by identifying metastatic deposits. The feasibility of multistep imaging protocols was demonstrated by Dahlbom et al. at UCLA, influencing current clinical practices.

Despite the dominance of BGO, an exception was the HEAD PENN-PET, developed with sodium iodide (NaI) scintillators by Muehllehner, Karp et al. at the University of Pennsylvania. Although NaI-based PET scanners had lower performance, they led to the development of the C-PET by UGM Medical. However, gamma cameras equipped with coincidence circuitry were eventually abandoned in favor of dedicated PET scanners due to their superior image quality.



Figure 2.18: UGM Medical C-PET

Some PET scanners are designed for specific organs like the brain, breast, or prostate. For example, the Montreal group's pioneering work on a breast tumor imaging device led to various breast PET designs, including commercial systems like the Oncovision MAMMI. Another example is a brain specific PET system, manufactured by the Swiss company POSITRIGO. Despite their improvements, most centers prefer whole-body PET scanners for their versatility in imaging all organs.



Figure 2.19: (left) Mammi Breast PET – (right) Positron NeuroLF Brain PET

During the 1990s and even earlier in the 1960s, there was significant interest in combining different imaging modalities to achieve a more comprehensive understanding of disease. Since the devices were separate and often in different departments, this was done through sophisticated software fusion algorithms. These algorithms were highly effective for brain images, such as PET with MR or PET with CT, due to the brain's fixed position within the skull. However, for other body parts,

the complexity increased due to more movement possibilities for organs. Bruce Hasegawa from UCSF, a pioneer in multimodality imaging, recognized this issue and in 1991, adopted "hardware" fusion by combining SPECT and CT. Independently, Townsend and Nutt proposed combining PET with x-ray CT in the same year, unaware that a similar design was developed by Prof. Nagai et al. at Gunma University in Japan in 1984. Their design placed a PET and CT scanner side-by-side with a single bed that moved between the scanners to acquire coregistered images without the patient leaving the bed. Townsend and Nutt's design integrated PET and x-ray CT into a single device, imaging both anatomy (CT) and function (PET), allowing a whole-body scan with minimal patient movement in one session.

A prototype PET/CT scanner was developed in collaboration between CPS Innovations and the University of Pittsburgh, funded by the National Cancer Institute, and began clinical evaluation in 1998, coinciding with Medicare's approval for some PET studies. This prototype allowed CT to provide attenuation correction factors for PET data, reducing patient throughput time. Despite initial mixed clinical interest, the successful early scans led to General Electric and Siemens developing commercial PET/CT designs in 2001. The combined device improved PET imaging and increased patient throughput, making PET/CT scans economically beneficial for hospitals and providing more accurate staging and diagnosis by synergizing PET's metabolic data with CT's anatomical information. By 2004, PET-only scanners were no longer available from major vendors. Philips also introduced a PET/CT scanner, and the technology rapidly advanced. Recent innovations include Toshiba's Celesteion PET/CT and United Imaging Healthcare's uMI 510, showing continuous improvements in design and technology. Today, there are more than 5000 PET/CT scanners worldwide, documenting the technology's benefits in over 12,000 publications.



Figure 2.20: United Imaging uMI Panorama PET/CT

The integration of PET/CT technology led to improvements like respiratory and cardiac gating, and continuous bed motion acquisition, which provides a more flexible interface for whole-body imaging. Before PET/CT's clinical reality, there was interest in combining PET with MR for better soft tissue contrast, especially in small animal imaging. However, traditional photomultiplier-based PET detectors do not function in a magnetic field. Development of semiconductor photodetectors led to the first PET detector using APDs, with Siemens producing the first APD-based PET/MR ring in 2006, followed by the first whole-body PET/MR in 2010. While PET/MR has shown advantages, its high cost has limited its clinical use, remaining primarily in research settings. SiPMs, offering faster timing and better performance, were introduced in PET/CT scanners by Philips and GE, enhancing the technology further.



Figure 2.21: United Imaging uMI Panorama PET/CT

Comparing PET/CT and PET/MR, a meta-analysis showed no clear advantage of PET/MR over PET/CT when MR is used only for anatomical framework. However, as the technology becomes more affordable and clinical applications emerge, PET/MR may find a place alongside PET/CT in clinical settings.

Reflecting on the progress of PET scanners, the ECAT II from 1976 had 66 detectors and a sensitivity of 0.16%, while today's Siemens Biograph mCT PET/CT scanner has 32,448 detector elements and a sensitivity of 6.4%, a forty-fold improvement over 40 years. This significant advancement highlights the remarkable progress in PET technology. (13)

2.6.4 Physics of PET Imaging

The physics underlying PET imaging are based on the emission of positrons by neutron-deficient radioisotopes. This process is illustrated with fluorine-18 (^{18}F), the most commonly used radioisotope, in **Figure 2.22**. As the radioisotope decays to a stable state, it emits a positron that travels a short distance (typically 1–2 mm) before interacting with an electron. This interaction annihilates both particles, producing two high-energy photons. These photons travel in opposite directions along a nearly straight line and can be detected by a PET scanner outside the body. The scanner's detectors, which use scintillator crystals coupled to photomultipliers, detect these photons.

The first limitation in PET imaging is noise, driven by the number of detected 511 keV photons. This is determined by the density of the scintillator, the count-rate capabilities of the scanner, and the amount of radiation injected into the patient. The second limitation is spatial resolution, influenced by the variability in estimating the interaction point of the 511 keV photon in the scintillator. This variability is affected by the optics of the scintillator, the number of emitted optical photons, and the performance of the photomultiplier tubes and associated electronics. These factors define the noise and resolution characteristics of the PET imaging process.

When two photons are detected within a short-coincidence time window (typically 1–10 ns), this joint detection is called a true-coincidence event for the line of response (LOR) joining the two detectors. More precisely, the parallelepiped joining the two detector elements is called a tube of response. The total number of true-coincidence events detected by the two detector elements is proportional to the total amount of radiotracer within the tube of response. This principle is central to PET imaging. Based on this relationship, coincidence events can be processed to accurately reconstruct the distribution of the radioisotope. For time-of-flight (TOF) PET imaging systems, the differential timing of the two photons' detection is used to localize the annihilation along the LOR.

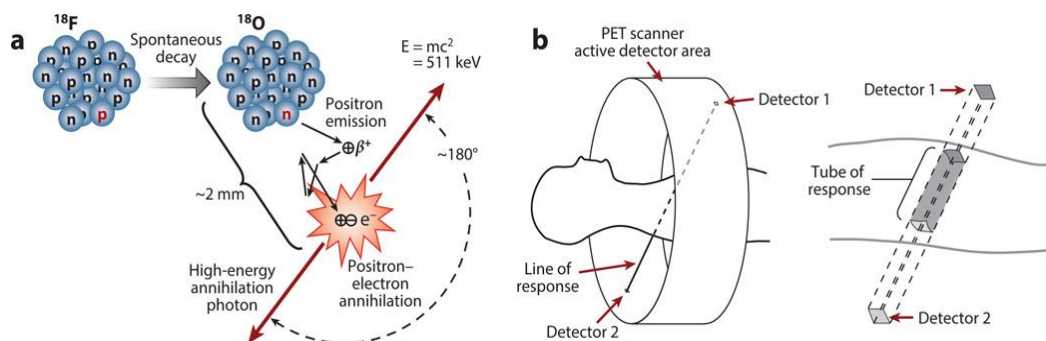


Figure 2.22: Basic PET Imaging physics

However, before accurate imaging can occur, confounding physical effects must be estimated and compensated for. The most important confounding effects are patient-specific and need to be reestimated for each scan; these include attenuation, scattered coincidences, and random coincidences (**Figure 2.23**). Patient motion (e.g., respiration-induced movements) can also be considered a confounding effect.

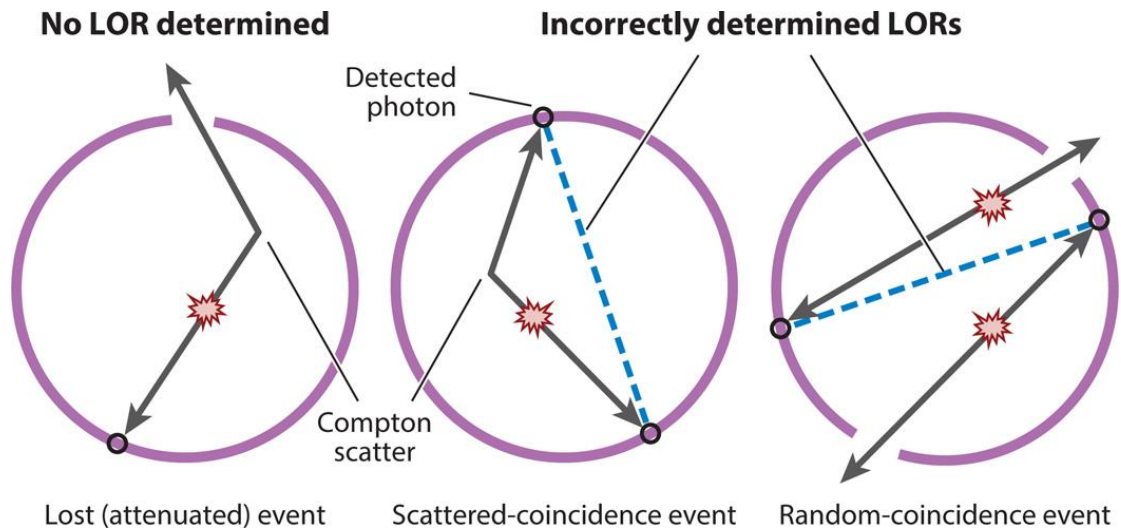


Figure 2.23: Confounding physical effects that cause bias in positron emission tomography (PET) coincidence imaging

In practice, a biologically functional compound is labeled with a positron-emitting radioisotope and injected into the patient or animal. The radiotracer preferentially accumulates in areas where the compound is metabolized. The biodistribution of the radiotracer changes over time, and this dynamic information can sometimes be used to analyze the image. (18)

CHAPTER 3rd

NUCLEAR CARDIOLOGY

3.1 Introduction

Clinical nuclear medicine studies play a crucial role in the noninvasive examination of cardiac physiology and function. The widespread utilization of nuclear cardiovascular examinations enables the sensitive identification and diagnosis of various cardiac abnormalities, along with determining the functional repercussions of disease. There are two main types of radionuclide imaging procedures that form the core of cardiovascular nuclear imaging. These procedures aim to evaluate myocardial perfusion and viability, as well as regional and global ventricular function. Through extensive experience in appropriate clinical contexts, these procedures have demonstrated their worth as valuable noninvasive tools for clinically assessing cardiac disease across a diverse patient population. Particularly noteworthy, gated single-photon emission computed tomography (GSPECT) allows for the simultaneous evaluation of coronary perfusion and left ventricular (LV) function in a single study. Meanwhile, PET imaging offers quantitative improvements to assessments of myocardial perfusion and viability at reduced patient doses. Moreover, the advent of hybrid imaging with SPECT/CT and PET/CT has facilitated image attenuation correction, thereby eliminating many common artifacts and bolstering the specificity of results.

3.2 Anatomy and Physiology

Understanding the anatomy and physiology of the heart is paramount due to its primary function as a pump. Each chamber's volume can be quantified as the end-diastolic volume (EDV), representing the volume of blood within the chamber at the end of diastole when it's fully filled. Although the EDVs of the left and right ventricles differ, stroke volumes (the amount of blood ejected by each ventricle during systole) must normally be equal, ranging from 80 to 100 mL. Cardiac output, the volume of blood pumped by either ventricle in a minute, is calculated by multiplying stroke volume by heart rate. Clinically, the ejection fraction, which considers both EDV and stroke volume, is a commonly used measurement. It represents the percentage of EDV ejected by a ventricle during systole.

In systole, the left ventricle (LV) typically undergoes a 20% shortening along its long axis and a 40% shortening along its short axis, with its walls moving inward. The apical portion of the LV experiences the least inward movement, while the anterior wall contributes the most to LV pump function. The septum thickens slightly and moves toward the LV center. Nuclear medicine techniques assess wall motion by observing ventricular wall segments in tangent. Abnormalities in regional wall motion

are usually categorized as hypokinetic (reduced wall motion), akinetic (absent wall motion), or dyskinctic, where a segment moves paradoxically outward during systole, indicating prior myocardial injury or a cardiac aneurysm.

During diastole, the myocardium relaxes initially without volume change but with a rapid decline in LV pressure, termed isovolumic relaxation. As LV pressure falls below the left atrium, the mitral valve opens, initiating the early rapid-filling phase, followed by diastasis, characterized by passive filling decline until the onset of atrial contraction, concluding diastole.

Coronary arteries supply the heart muscle, with major branches including the left anterior descending (LAD) and circumflex coronary arteries. The LAD supplies the anterior interventricular septum and anterolateral LV wall, while the circumflex artery nourishes the left atrium and posterolateral LV wall. The right coronary artery supplies the right atrium, right ventricle, inferior LV wall, and part of the interventricular septum, with dominance determined by which artery supplies the posterior descending coronary artery.

Normal coronary blood flow is approximately 0.6 to 0.8 mL/min/g of myocardium, increasing during exercise or pharmacological stress. Blood flow is highest during diastole when vessels are least constricted by surrounding cardiac muscle. Narrowing of coronary artery diameter below 50% has minimal clinical impact on blood flow, while narrowing approaching 70% becomes hemodynamically significant, especially during exercise. Significant narrowing at rest typically requires 90% or greater constriction.

3.3 SPECT Myocardial Perfusion Imaging

SPECT myocardial perfusion imaging stands as the cornerstone of cardiac examinations in clinical nuclear medicine, primarily aiming to assess myocardial blood flow adequacy, especially during exercise or pharmacologic stress, for coronary artery disease (CAD) detection and evaluation. While principles remain consistent, imaging protocols vary among the radiopharmaceuticals employed. Options include technetium-99m (^{99m}Tc)-labeled agents, thallium-201 (^{201}Tl) chloride, or positron-emitting radiopharmaceuticals. The forefront technique is SPECT with electrocardiogram (ECG) gating (GSPECT), which yields tomographic images reflecting regional perfusion alongside LV functional parameters, offering an enriched physiological evaluation of the heart.

Diagnostic assessment of occlusive coronary disease via radionuclide imaging involves detecting relatively reduced myocardial perfusion beyond the site of vascular obstruction compared to surrounding normally perfused myocardium. Successful imaging relies on various factors, notably the degree and hemodynamic significance of stenosis under conditions of heightened myocardial metabolic demand, such as exercise. As severe stenosis might not manifest detectable blood flow abnormalities at rest, stress—either through exercise or pharmacologic means—is typically necessary to create a discernible flow differential visible on myocardial perfusion imaging.

During exercise, the heart predominantly augments coronary blood flow to meet increased oxygen demands by rapidly dilating vessels. This ability to elevate blood flow from baseline to maximal levels is termed coronary reserve. In the presence of a fixed coronary stenosis, coronary reserve diminishes during stress, leading to apparent relative defects in myocardial perfusion images within areas supplied by the stenosed artery. Although stenoses up to 90% of arterial diameter may not significantly reduce blood flow detectable at rest, myocardial perfusion imaging reliably identifies stenoses of 50% or more under maximal myocardial stress conditions. Comparing baseline and stress perfusion enables the identification of areas with reduced coronary reserve, indicating stenoses and consequent stress-induced ischemia, irrespective of the radiopharmaceutical or stress method employed.

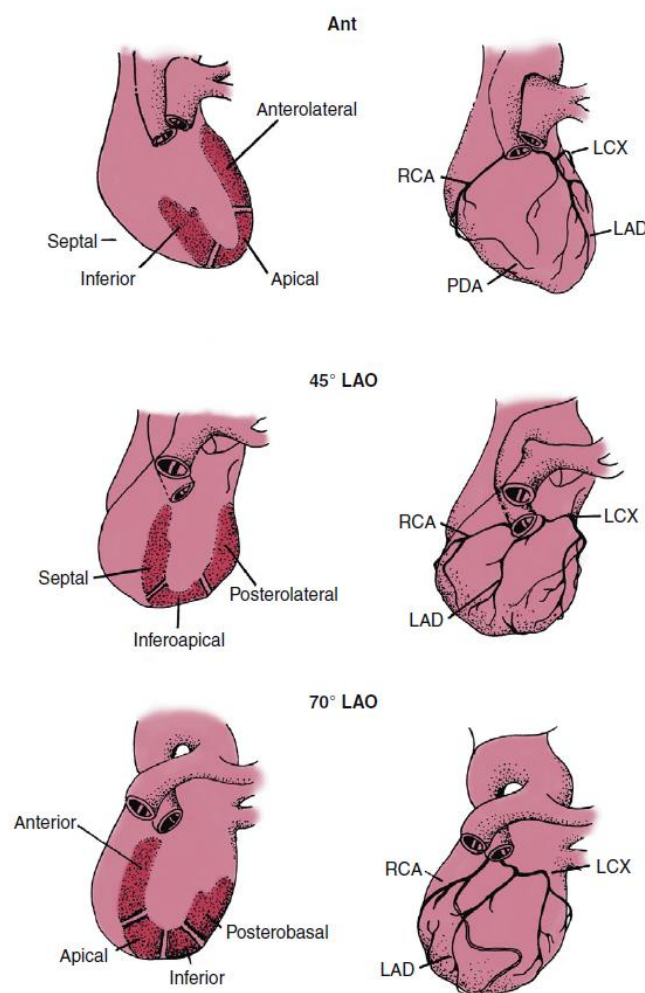


Figure 3.1: Schematic representation of the left ventricular walls and the associated blood supply (19)

3.4 Cardiac Scintigraphy Radiopharmaceuticals

The utilization of radiopharmaceuticals in myocardial perfusion imaging has evolved over time. While ^{201}Tl was the pioneering agent and remains in use across various clinical settings, there's a prevailing preference for $^{99\text{m}}\text{Tc}$ labeled radiopharmaceuticals due to their advantageous properties. These differences in biokinetics among radiopharmaceuticals significantly influence imaging protocols, impacting aspects such as timing and image acquisition sequences. Understanding the behavior of these radiopharmaceuticals is crucial for devising examination protocols and interpreting resulting images.

Thallium-201, a cyclotron-produced radionuclide, boasts a relatively long physical half-life, facilitating convenient storage and imaging over several hours. However, its extended half-life increases patient radiation exposure and imposes limits on the administered dose. Thallium's biokinetics are akin to potassium, involving initial distribution based on blood flow and subsequent redistribution mediated by ongoing extraction and washout processes.

On the other hand, technetium-99m labeled radiopharmaceuticals, overcoming technical limitations of ^{201}Tl , offer several advantages such as ready availability, larger administered activity, and superior image resolution. Unlike ^{201}Tl , technetium-labeled agents do not undergo significant redistribution, remaining fixed in myocardial distribution post-injection.

Technetium-99m sestamibi and tetrofosmin are commonly used examples, both characterized by minimal redistribution over time. Sestamibi, a lipophilic cationic isonitrile, demonstrates advantageous fixed distribution, enabling delayed imaging without loss of sensitivity. Tetrofosmin, a cationic diphosphine, also exhibits little redistribution, facilitating imaging within a short timeframe post-injection.

Emerging radiopharmaceuticals labeled with Tc-99m and other radioisotopes hold promise for providing more specific information on myocardial perfusion and viability status. For instance, I-123 BMIPP, a labeled fatty acid, represents one such promising avenue for SPECT imaging, offering potential advancements in this field. (20)

3.5 Specialized Cardiac SPECT Systems

Advanced cardiac SPECT cameras have emerged as a result of the widespread use of myocardial perfusion imaging, the high radiation doses associated with conventional SPECT technology, and the potential for imaging enhancements in cardiac-specific applications. These innovative cameras offer improved count sensitivity, which can lead to dose reduction or increased patient throughput with standard doses, sometimes coupled with enhanced resolution. Rapid imaging capabilities also mitigate patient discomfort and movement, thereby reducing motion-related image artifacts. Departing from traditional orbiting SPECT cameras, newer designs incorporate detector arrays, either fixed or with limited rotation, featuring curved sodium iodide detectors or solid-state detectors like cadmium zinc telluride (CZT), along with specialized

collimators. These advancements enable significant reductions in scan times, from 10 to 15 minutes per acquisition down to 2 to 5 minutes.

Moreover, alongside hardware improvements, there have been strides in image reconstruction software tailored to the characteristics of these cameras. These software advancements, termed resolution recovery algorithms, target the reduction of image noise and the enhancement of spatial resolution. Leveraging iterative reconstruction techniques instead of traditional filtered back projection, these programs address factors inherent in SPECT imaging that degrade image quality, particularly in settings of shorter imaging times and reduced counting statistics. While more intricate and time-intensive, iterative back projection holds the potential to produce transaxial images of equal or superior quality compared to those generated by traditional SPECT imaging methods. (21)

3.6 Cardiac Imaging Protocols

Imaging procedures for myocardial perfusion are predominantly conducted through SPECT, with or without gated acquisition, using either ^{201}Tl or $^{99\text{m}}\text{Tc}$ -labeled radiopharmaceuticals. SPECT imaging involves varied acquisition and processing protocols depending on the specific radiopharmaceutical utilized. Despite these differences, SPECT imaging demands technical precision. Adherence to quality-control measures and familiarity with established study protocols are imperative for ensuring procedural standardization and consistently accurate outcomes.

For exercise Thallium SPECT imaging, patients typically undergo an initial post-exercise set of myocardial images followed by an identical set of delayed redistribution images. The procedure begins with the administration of 2 mCi (74 MBq) of thallium intravenously at peak exercise, with imaging initiated within the first 10 to 15 minutes post-exercise. The patient is positioned on the imaging table, with specific acquisition protocols varying among facilities. Redistribution images are acquired 3 to 4 hours later to assess myocardial perfusion at rest, typically utilizing the same instrument employed for post-exercise imaging. Patient positioning and additional thallium administration before the second set of images aim to ensure optimal redistribution conditions.

In contrast, the exercise Technetium-99m radiopharmaceutical SPECT imaging protocol necessitates separate stress and rest injections of $^{99\text{m}}\text{Tc}$ sestamibi or $^{99\text{m}}\text{Tc}$ tetrofosmin to distinguish fixed from reversible defects. Various imaging protocols, including 1- and 2-day approaches, are employed. The 1-day protocol, commonly utilized for patient convenience, involves stress and rest examinations performed on the same day. Dosage adjustments and meticulous patient preparation are crucial to mitigate interfering activities and optimize imaging quality.

Dual-isotope imaging, employing separate ^{201}Tl and $^{99\text{m}}\text{Tc}$ sestamibi/tetrofosmin SPECT acquisitions, offers an efficient alternative, allowing the entire examination to be completed within 90 minutes. This protocol involves a rest ^{201}Tl study followed by

a stress ^{99m}Tc sestamibi or tetrofosmin study, minimizing interference between isotopes and enhancing specificity in detecting perfusion defects.

Regarding patient absorbed dose considerations, myocardial perfusion imaging entails relatively high radiation doses. However, strategies such as using $\text{Tc-}^{99\text{m}}$ radiopharmaceuticals, implementing lower administered dose protocols, and employing stress-only acquisitions can help reduce patient doses. Additionally, advancements in imaging technologies, such as PET myocardial perfusion imaging and innovations in SPECT such as the CZT detectors, hold promise for further dose reduction in the future.

Radiopharmaceutical	Protocol	Stress Dose (mCi)	Rest Dose (mCi)	Effective Dose (mSv)
$\text{Tc-}^{99\text{m}}$ sestamibi	Stress-Rest	27.5	10	11.3
	Stress only	27.5	0	7.9
	2-day	25	25	15.7
$\text{Tc-}^{99\text{m}}$ tetrofosmin	Stress-Rest	27.5	10	9.3
	Stress only	27.5	0	6.6
	2-day	25	25	12.8
Tl-^{201}	Stress-redistribution	3.5	0	22
	Stress-reinjection	3	1.5	31.4
$\text{Tl-}^{201}/\text{Tc-}^{99\text{m}}$ sestamibi	Stress-Rest	25	3.5	29.2
Rb-^{82} PET		50	50	13.5
N-^{13} ammonia PET		15	15	2.4
F-^{18} FDG PET		0	0	7.0

Table 3.1: Myocardial Perfusion Imaging: Patient Dose by Protocol (the doses between stress and rest may be the other way around if the stress acquisition is initially acquired) (19)

3.7 Myocardial SPECT Image Processing and Display

Myocardial SPECT image processing involves reformatting post-stress and rest images into oblique planes. Due to the heart's oblique axis of symmetry, standard cross-sectional views are insufficient. Therefore, images are reconstructed in three planes: short-axis (SA), vertical long-axis (VLA), and horizontal long-axis (HLA). Reconstruction relies on identifying the heart's long axis, allowing the computer to generate tomographic images in three orthogonal planes relative to the heart's orientation. Typically, slices are 1 to 2 pixels thick with a 64×64 or 128×128 matrix.

Computer processing enhances SPECT image quality through background subtraction, contrast enhancement, and image filtering, aiming to improve contrast and remove unwanted activity and noise. Various filters like Butterworth, Hamming, and Hanning are available, selected based on interpreter preferences. Care is taken to avoid overprocessing, which could distort data and induce artifacts.

In medical imaging, specifically for myocardial perfusion imaging (MPI), the two most commonly employed methods for image reconstruction are **Filtered Back-Projection (FBP)** and **Iterative Reconstruction**. Each of these techniques has its own strengths, weaknesses, and applications, and understanding their differences is crucial for optimizing image quality, particularly in nuclear cardiology.

- **Filtered Back-Projection (FBP)**

FBP has historically been the most widely used image reconstruction technique in clinical settings, especially in cardiac single-photon emission computed tomography (SPECT). It is classified as an **analytical reconstruction method**, which means it uses direct mathematical formulas to reconstruct images. The popularity of FBP stems from its **simplicity** and **speed**, making it an attractive option for time-sensitive clinical environments.

FBP works by back-projecting raw projection data collected during the scan. In a typical 2D acquisition, each row of projections represents the sum of all counts along a straight line through the object being imaged. These projections are organized based on the angle at which they are acquired and form what is known as a **sinogram**. The back-projection process redistributes these counts to each point along the line from which they were originally detected, for all pixels and at all angles.

However, one major drawback of FBP is that it assumes uniform distribution of the projection data, which often results in **blurring** and **star artefacts** in the final image. These artefacts arise because FBP does not account for various physical processes that occur during data acquisition, such as **attenuation**, **scatter**, or the physical properties of the imaging system. To mitigate these issues, a **filtering step** is applied to the data before back-projection. This involves the use of a **window filter** in the frequency domain, often utilizing the **fast Fourier transform (FFT)**, which helps reduce artefacts and enhances image clarity. Despite these efforts, FBP's inability to model the complexities of emission tomography has led to its gradual decline in favor of more sophisticated reconstruction techniques.

- **Iterative Reconstruction**

Iterative reconstruction, in contrast to FBP, is a more advanced technique that provides greater flexibility and accuracy. It is based on **algebraic reconstruction techniques (ART)** and allows for the incorporation of more accurate models of image formation. Unlike FBP, which makes assumptions based on the Radon transform, iterative methods can model important physical processes such as **attenuation**, **scatter**, **collimator response**, and even **statistical noise**. These capabilities make iterative reconstruction particularly valuable in emission tomography, where the complexities of the imaging process cannot be easily captured by simple analytical models.

The process of iterative reconstruction begins with an initial guess of the activity distribution within the object, which is often generated using FBP. The system then generates synthetic projections from this guess and compares them with the actual measured projections. The differences between the synthetic and measured projections are used to refine the initial guess, and this process is repeated multiple

times, hence the term "iterative." The goal is to minimize the differences between the calculated projections and the measured data until they fall below a predefined threshold.

There are several different iterative algorithms, with **Maximum Likelihood Expectation Maximization (MLEM)** being one of the earliest and most well-known. MLEM assumes that the noise in the projection data follows a Poisson distribution, which is a more realistic representation of the noise encountered in nuclear medicine imaging. However, MLEM is computationally intensive and can take a long time to converge, making it less practical for routine clinical use.

To address this, an accelerated version of MLEM known as **Ordered Subsets Expectation Maximization (OSEM)** has become the most widely used iterative technique in clinical practice. OSEM divides the projection data into subsets and updates the image estimate after processing each subset, significantly reducing the overall reconstruction time. This reduction in computational demand has made iterative reconstruction more feasible in routine clinical environments, particularly with the advancements in computer processing power over recent years.

New Trends in Image Reconstruction: Resolution Recovery and Noise Suppression

Although FBP and iterative reconstruction have been the standard in medical imaging, there have been significant efforts to further enhance image quality, reduce noise, and improve spatial resolution in MPI. One of the most important recent advancements is the incorporation of **Resolution Recovery (RR)** algorithms into the iterative reconstruction process.

RR algorithms address one of the major limitations of traditional imaging systems: **distance-dependent blurring**. As the distance between the detector and the object being imaged increases, blurring becomes more pronounced, degrading image quality. RR compensates for this effect by integrating the physical characteristics of the imaging system, such as the **point spread function (PSF)**, into the reconstruction algorithm. This enables more accurate modeling of how the system records photon counts from different locations within the object.

The **collimator detector response (CDR)** is a critical component of resolution recovery. It accounts for the design of the collimator (e.g., hole length, diameter, septa thickness) and the intrinsic properties of the detector (e.g., crystal thickness, intrinsic resolution). These physical parameters are stored in a look-up table within the reconstruction software and are used to correct for the blurring effects that occur as photons pass through the collimator and reach the detector. By incorporating these factors into the reconstruction process, RR can improve both the **signal-to-noise ratio (SNR)** and **spatial resolution** of the final image, resulting in clearer, more diagnostic images.

Additionally, modern iterative reconstruction algorithms often include **noise suppression (NS)** techniques, which further enhance image quality by reducing the impact of statistical noise. This is particularly important in MPI, where the inherently low count rates can lead to noisy images. By simultaneously addressing both

resolution recovery and noise suppression, newer iterative methods are able to produce images that are superior to those obtained using traditional FBP, both in terms of clarity and diagnostic accuracy.

Clinical Impact and Future Trends

The introduction of these advanced reconstruction techniques has significant implications for clinical practice. One of the key benefits of these newer methods is the potential for **shorter acquisition times**. Traditional MPI scans typically require 15-20 minutes for both stress and rest acquisitions, which can lead to patient motion artefacts and increased radiation exposure. However, with the improved SNR and resolution offered by RR and NS, it may be possible to acquire equivalent diagnostic images in **half the time**, reducing both the likelihood of artefacts and the patient's exposure to radiation.

In summary, while **Filtered Back-Projection** remains a useful and fast method for image reconstruction, its limitations in handling complex physical phenomena have led to the rise of **Iterative Reconstruction** techniques. **OSEM** has emerged as the dominant method, combining the accuracy of iterative techniques with the efficiency required for clinical use. Looking forward, the integration of **Resolution Recovery** and **Noise Suppression** algorithms represents a promising step toward even better image quality, reduced scan times, and improved patient outcomes in nuclear cardiology. (22)

Following processing, myocardial slices are displayed to facilitate stress and redistribution/rest image comparison. Corresponding slices between image sets must be accurately displayed for comparison. The image orientation is standardized to convention, usually automated by manufacturer-supplied software. Interpretation involves manipulating image intensity and contrast on computer screens or viewing stations.

In the context of cardiac scintigraphy, the terms **bullseye plot** and **polar map (2D)** are often used interchangeably, as they both represent similar techniques for displaying myocardial perfusion data. These representations condense three-dimensional (3D) data obtained from myocardial SPECT images into a two-dimensional (2D) display, providing a comprehensive visualization of the left ventricular myocardium, which resembles the heart as viewed from its apex.

Nevertheless, subtle differences exist in their usage and interpretation:

- **Bullseye Plot:** This term emphasizes the visual analogy of the plot, resembling a target or "bullseye" with concentric circles. It is widely used in clinical settings due to its straightforward presentation of myocardial perfusion, depicting the heart's various regions—such as the apex, septal wall, and lateral wall—within a circular image. The bullseye plot allows for easy visual comparison between stress and rest images, facilitating the assessment of perfusion defects' reversibility. Additionally, color coding helps in identifying areas of reduced perfusion, ischemia, or infarction.

- **Polar Map (2D):** While functionally similar to the bullseye plot, the term polar map tends to be more technical, referring to the mathematical transformation of 3D cardiac data into a 2D polar coordinate system. This term is often used in research or quantitative analysis, where more precise segmentation of the myocardium (e.g., 17- or 20-segment models) is necessary. The polar map is commonly used for semiquantitative comparisons, where patient data are compared to a normal database to identify perfusion deficits.

Additionally, both representations provide a valuable summary of myocardial perfusion patterns. However, interpretations must account for potential distortions: perfusion defects at the heart's base may appear exaggerated, while centrally located defects may be underrepresented. These visual tools complement traditional image interpretation by summarizing the patient's perfusion status in an accessible format, supporting both diagnostic and treatment decisions.

In conclusion, while both the bullseye plot and polar map serve the same fundamental purpose of visually representing myocardial perfusion, the bullseye plot is more frequently used in clinical practice due to its intuitive visual format, whereas the polar map is favored for its technical precision, particularly in research. Their complementary roles help summarize complex myocardial perfusion data in a form that aids clinicians in diagnosing and managing coronary artery disease.

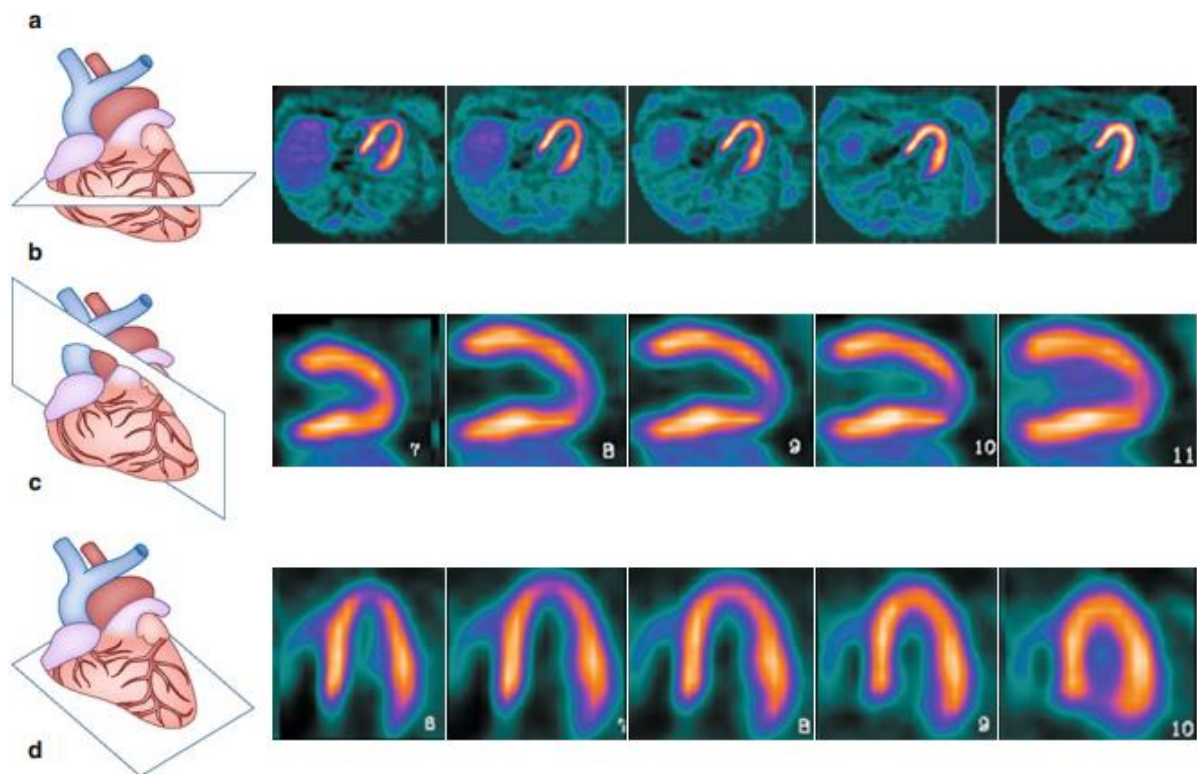


Figure 3.2: Short-axis (SA), vertical long-axis (VLA), and horizontal long-axis (HLA) myocardial views (23)

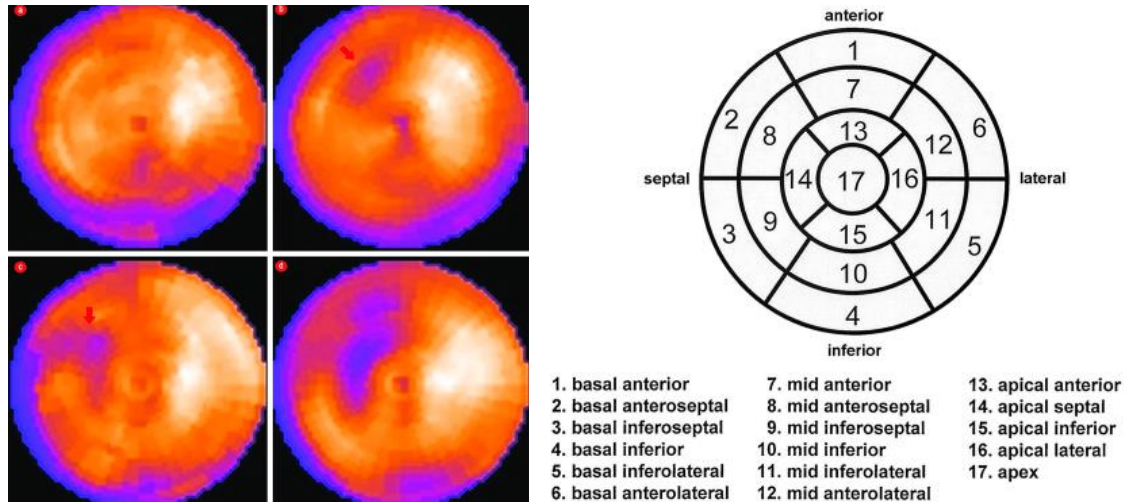


Figure 3.3: Bull's eye display of myocardial perfusion (24)

3.8 Approach to Analyzing Images

The principles for interpreting SPECT myocardial perfusion images are mostly similar to those for qualitative interpretation of thallium and Tc-99m labeled agents, with a few differences. A systematic approach to ensure consistent interpretation includes:

- Proper alignment of post-stress and rest tomographic slices.
- Examination for motion and attenuation artifacts, with sinogram or rotating cine images reviewed if necessary.
- Evaluation of LV myocardium for perfusion defects, considering size, severity, location, and reversibility.
- Estimation of LV cavity size and any transient enlargement.
- Assessment of lung and right ventricular activity, and adjacent splanchnic activity.
- Correlation with stress ECG findings and adequacy of stress.
- Incorporation of ancillary patient information like medical history, clinical findings, prior angiography, or perfusion studies.
- For GSPECT studies: evaluation of LV ejection fraction (LVEF) and correlation of wall motion with perfusion abnormalities.

Alignment of Images

Ensuring proper alignment of reconstructed stress and rest slices is crucial for accurate comparison of myocardial perfusion. Misalignment can lead to false impressions of perfusion abnormalities' nature and reduce examination accuracy.

Artifacts

As tomographic images are highly processed, it's essential to ensure they're free of artifacts. Suspected artifacts require careful examination of raw data, including rotating cine displays, to detect patient motion, soft-tissue attenuation, or interfering activity. Thorough knowledge of SPECT imaging artifacts is critical.

Attenuation Artifacts

Significant soft-tissue attenuation can create false fixed defects, particularly in the anterior or lateral walls. Other sources like intense liver or bowel activity can mask perfusion areas or induce apparent defects. Attenuation correction methods can improve specificity but require careful interpretation due to potential differences between corrected and uncorrected images.

Motion Artifacts

Patient motion can cause artifactual defects, with the appearance depending on direction, degree, and timing. Motion-correction software can salvage studies with mild motion artifacts. Vigorous exercise may induce artifacts like cardiac creep, which can be avoided with delayed image acquisition.

Technical Artifacts

Errors in image reconstruction or equipment quality control can produce significant artifacts. Incorrect selection of the LV's long axis or imaging system malfunctions can lead to overestimation or underestimation of activity, affecting interpretation.

Normal Appearance and Variants

Normal myocardial perfusion studies may show slight activity variations, especially at the LV apex and certain anatomical regions. Focal hot spots near papillary muscles can sometimes mimic defects but are usually artifacts. An appreciation of normal variants aids in distinguishing true abnormalities.

Abnormal Scans

Visual Analysis

Abnormal radiopharmaceutical distribution in the myocardium can indicate stress-induced ischemia or permanent damage. Reversible defects disappear or diminish between stress and rest studies, while fixed defects show no significant change. Reverse redistribution, less common, indicates prior infarction or artifact.

Description of Myocardial Perfusion Abnormalities

Myocardial perfusion defects should be described based on size, severity, location, and reversibility. Differentiation between reversible and fixed defects

is crucial, as fixed defects may represent viable myocardium rather than scar tissue. PET imaging or thallium studies can help differentiate.

Lung Activity

Excessive lung activity post-exercise correlates with transient LV dysfunction and high-risk CAD. Increased lung activity may indicate submaximal exercise or CAD severity, impacting prognosis.

Transient Ischemic Dilatation

Transient LV cavity dilatation post-stress suggests stress-induced diffuse subendocardial ischemia rather than true cavity dilatation. It correlates with high-risk CAD and a worse prognosis.

Right Ventricular Activity

Transient right ventricular defects suggest right CAD. Persistent right ventricular activity on rest or redistribution imaging may indicate pathology like ventricular hypertrophy or increased workload.

Splanchnic Activity

Splanchnic activity can indicate exercise adequacy, with intense activity suggesting suboptimal exercise. Understanding activity patterns aids in image interpretation.

Quantitative Analysis

Quantitative analysis complements visual interpretation, allowing objective assessment of perfusion changes. Semiquantitative approaches like scoring systems help assess defect size, severity, and reversibility, aiding in disease progression or treatment evaluation. (19)

3.9 SPECT with Gated Acquisition (GSPECT)

GSPECT represents the latest advancement in myocardial perfusion imaging and is widely used in clinical practice. It incorporates all the information from myocardial perfusion tomography discussed earlier, along with relevant data on regional and global left ventricle (LV) function. Unlike non-gated myocardial SPECT imaging, which captures data without considering the cardiac cycle, GSPECT synchronizes data collection with the patient's ECG. This synchronization reduces or eliminates the negative impact of ventricular wall motion on image quality.

GSPECT allows for a cinematic display of myocardial images throughout the cardiac cycle, enabling assessment of wall motion alongside perfusion abnormalities. Key LV parameters measured with GSPECT include LV ejection fraction (LVEF) and absolute LV volumes (end-systolic and end-diastolic). However, it is not suitable for

evaluating right ventricular (RV) function due to limitations in visualizing the RV myocardium. While GSPECT can be performed with ^{201}Tl using multidetector cameras, non-redistributing $^{99\text{mTc}}$ -labeled myocardial perfusion agents are preferred due to better imaging characteristics and more reliable measurement of LV functional parameters.

Recent studies comparing LV functional parameters obtained via GSPECT using different software programs showed significant variations in LV volumes and LVEF. These differences underscore the importance of consistent software usage for sequential studies and highlight the need for each lab to establish its own normal values for LV parameters.

The technique of gating to the cardiac ECG cycle resembles that used in gated blood pool ventriculography but produces a dynamic image of the contracting myocardium instead of the blood pool chamber. Automated computer software detects the epicardial and endocardial edges of the myocardium to define the LV walls throughout the cardiac cycle, facilitating measurement of LV volume changes and LVEF calculation.

GSPECT acquisitions are typically obtained post-stress and take about 20 to 30 minutes. The data is usually acquired as 8 to 16 frames per cardiac cycle and displayed in an endless-loop cine format for visual analysis. Although a 16-frame acquisition offers better temporal resolution, it requires longer acquisition times compared to an 8-frame acquisition. It's important to note that an 8-frame acquisition may yield a slightly lower calculated ejection fraction than a 16-frame acquisition.

While GSPECT provides valuable insights into LV function, it has limitations in patients with small hearts, where it may overestimate LVEF. Arrhythmias can also impact gating accuracy, with severe arrhythmias necessitating non-gated myocardial perfusion imaging.

Data Display and Interpretation GSPECT generates coregistered sets of post-stress and rest slices of the myocardium similar to non-gated perfusion studies. Additionally, it allows for a closed cine loop of cardiac wall motion, enabling correlation of myocardial perfusion defects with wall motion abnormalities in the same region. Wall motion abnormalities are assessed visually and categorized as hypokinetic, akinetic, or dyskinctic.

Automated software programs provide quantitative indices of regional wall motion and wall thickening, enhancing the analysis. LV parameters like LVEF and volumes are also automatically calculated, adding further clinical significance to the results.

Clinical Applications of GSPECT plays a crucial role in several clinical scenarios, including the identification of attenuation artifacts, enhanced detection of multivessel coronary artery disease (CAD), risk assessment in CAD patients, evaluation of myocardial viability, follow-up after revascularization procedures to assess LV wall motion improvement, and differentiation between ischemic and nonischemic cardiomyopathy. (25)

3.10 Exercise Stress Procedure

Exercise is typically the preferred method for stressing patients during myocardial perfusion imaging. The standard exercise protocol remains consistent regardless of the radiopharmaceutical used.

Patients are advised to fast for 4 to 6 hours before the exercise test. This fasting period reduces splanchnic blood flow, which in turn lowers uptake in the bowel and liver. To ensure an adequate stress examination, patients should discontinue calcium-channel blockers and β -blockers if possible, for a sufficient duration before the test. Long-acting nitrates should also be avoided on the day of testing. Additionally, patients are encouraged to abstain from caffeinated beverages for at least 24 hours before the examination, allowing for a potential shift to vasodilator pharmacologic stress using dipyridamole, adenosine, or regadenoson if needed.

The most common stress method in myocardial perfusion imaging is a multistage treadmill exercise test, often following a Bruce or modified Bruce protocol. This protocol involves a gradual increase in treadmill speed and grade to incrementally raise stress levels.

Timing during exercise is crucial. Regardless of the radiopharmaceutical used, it should be injected at peak stress, usually via a pre-established intravenous line or heparin lock. Ideally, patients continue exercising for about 30 seconds to 1 minute post-injection, allowing the radiopharmaceutical sufficient time to localize in the myocardium during peak exercise conditions. The determination of peak stress varies but is typically considered maximal when certain conditions are met, such as chest pain or significant ECG changes, reaching 85% of predicted maximum heart rate, or exceeding a specific heart rate-blood pressure product value.

Maximal stress yields optimal myocardial-to-background ratios for imaging and provides the most sensitive evaluation of myocardial perfusion. Failure to achieve maximal stress is a common reason for false-negative results, but even submaximal exercise studies offer higher sensitivity than stress ECG alone for detecting coronary artery disease. In some cases, intentionally submaximal exercise tests may be conducted for specific evaluations, such as assessing residual stress-induced ischemia post-myocardial infarction.

3.11 SPECT Clinical Applications

Coronary Artery Disease

The clinical applications of SPECT imaging in diagnosing coronary artery disease (CAD) are well recognized. SPECT imaging, particularly stress and rest or redistribution myocardial perfusion scans, is highly sensitive and specific for detecting CAD. Its sensitivity increases with the severity of stenosis and the extent of the disease. Compared to exercise electrocardiography, SPECT imaging offers significantly higher sensitivity (80% to 90%) for detecting stress-induced ischemia.

It's especially useful for patients with nondiagnostic exercise ECGs due to various reasons like baseline abnormalities or inadequate stress.

Diagnostic stress myocardial perfusion imaging is most beneficial for patients with suspected CAD who have inconclusive exercise ECG results or an intermediate probability of disease. However, while SPECT imaging is sensitive and specific for CAD diagnosis, it may be less effective in determining the extent of the disease, especially in cases of balanced, symmetric three-vessel CAD. Additional functional data from GSPECT can enhance the assessment of CAD severity, especially in detecting multivessel CAD and left main CAD.

In terms of prognosis and risk stratification, stress myocardial perfusion imaging is valuable for assessing the risk of future cardiac events in patients with known CAD. Various factors such as the number and size of reversible defects, extent of fixed defects, and LV functional parameters like LVEF and ESV are important prognostic indicators. Additionally, SPECT imaging aids in evaluating the hemodynamic significance of coronary stenosis, assessing myocardial viability, and determining the success of revascularization procedures post-myocardial infarction or coronary interventions like bypass grafting or angioplasty.

Overall, SPECT imaging, especially when combined with GSPECT functional data, plays a crucial role in diagnosing, risk-stratifying, and managing patients with CAD, offering valuable insights into disease severity, prognosis, and treatment outcomes.

Non-Coronary Diseases

Patients with mitral valve prolapse but no confirmed CAD may occasionally exhibit exercise-induced perfusion defects, the cause and significance of which are uncertain and need investigation to rule out ischemia. However, a normal exercise myocardial perfusion study in these patients indicates the absence of CAD.

Individuals with valvular aortic stenosis, despite lacking CAD, might experience angina-like symptoms. Approximately 40% to 50% of these patients could show reversible perfusion defects, likely due to reduced perfusion in coronary arteries associated with severe aortic stenosis. Therefore, interpreting post-exercise perfusion abnormalities in aortic stenosis patients requires caution. Similarly, patients with aortic regurgitation but no CAD may display stress-induced reversible defects in the heart's apex. However, the presence of defects in other ventricular regions necessitates ruling out CAD.

Left Bundle-Branch Block (LBBB) makes ECG stress testing inconclusive for CAD diagnosis, leading to the use of radionuclide myocardial perfusion imaging for noninvasive diagnosis. LBBB patients might show reversible septal or anteroseptal perfusion abnormalities during intense exercise without CAD, likely due to asynchronous septal relaxation conflicting with diastolic coronary filling. Thus, while reversible septal defects during exercise in LBBB patients are uncertain, reversible defects elsewhere in the heart still indicate transient ischemia. Pharmacologic stress using adenosine or dipyridamole is a viable alternative to exercise stress, particularly for LBBB patients, as it reduces false positives.

Hypertensive individuals often undergo myocardial perfusion imaging due to their increased CAD risk. Longstanding hypertension leading to myocardial hypertrophy can cause a relative increase in septal wall activity on stress and redistribution images, potentially creating a false impression of a fixed lateral wall defect, especially in certain imaging angles. This phenomenon may also occur in patients with idiopathic subaortic stenosis, highlighting the importance of considering hypertension or subaortic stenosis history in such imaging studies. (19)

3.11 PET Cardiac Imaging

PET cardiac imaging has experienced significant growth in availability and application, evolving from a rarely used tool to a widely utilized technology over the past decade. Its inherent advantages over SPECT imaging contribute to its attractiveness in myocardial imaging. These advantages encompass better spatial resolution (2 to 3 mm compared to SPECT's 6 to 8 mm), higher myocardial count rates leading to better quality images, and superior quantitative capabilities. PET's ability to assess wall motion and left ventricular (LV) function, akin to gated-SPECT, is further enhanced in PET/CT by built-in attenuation correction, significantly reducing false-positive studies caused by attenuation artifacts.

In the realm of myocardial perfusion imaging, PET aligns with SPECT's principles, particularly in the diagnosis of coronary artery disease (CAD). Comparative studies consistently demonstrate PET's superiority, showcasing higher sensitivity (96% versus 85%), specificity (80% versus 65%), and overall diagnostic accuracy (90% versus 80%) when compared to SPECT. The utilization of radiopharmaceuticals such as Rb-82 in PET imaging allows for faster study completion times than traditional SPECT methods, presenting a notable advantage in clinical settings.

PET imaging further extends its utility by enabling the quantification of absolute myocardial perfusion using N-13 ammonia, a capability that proves beneficial in detecting balanced ischemia in patients with three-vessel coronary stenosis, even in the absence of visually detectable regional perfusion defects. However, it is worth noting that these absolute quantification studies are primarily performed for research purposes at present.

The range of radiopharmaceuticals available for PET imaging, including $^{13}\text{NH}_3$, H_2^{15}O , and Rb-82, each with its own set of characteristics and limitations, underscores the versatility of PET technology in myocardial assessment. Protocols for PET myocardial perfusion imaging, particularly with Rb-82, have been well-established, offering efficient studies with pharmacologic stress, given the short half-life of Rb-82 necessitating pharmacologic stress over physical exercise.

Beyond myocardial perfusion assessment, PET also plays a crucial role in evaluating myocardial viability, especially using F-18 FDG. This capability allows for the identification of chronically ischemic yet viable myocardium, aiding in distinguishing

hibernating myocardium from scars and guiding appropriate patient management decisions.

While PET imaging holds significant promise and advantages over traditional SPECT methods, it also presents challenges such as higher costs, complex procedures, and potential motion artifacts that require careful consideration and management. Nonetheless, PET/CT has expanded its applications, even venturing into areas like aortic dissection evaluation, where it provides valuable insights into differentiating acute from chronic dissections and influencing treatment strategies based on distinct FDG uptake patterns. (19)

CHAPTER 4th

CARDIAC PHANTOM CONSTRUCTION

4.1 Introduction to 3D Printing

Three-dimensional (3D) printing, also known as additive manufacturing, encompasses a variety of processes used to create three-dimensional objects through the successive layering of materials under computer control. This transformative technology allows for the fabrication of objects with intricate geometries and customized properties, which can be difficult or impossible to achieve with traditional manufacturing techniques. 3D printing begins with a digital 3D model, typically created using computer-aided design (CAD) software, which serves as the blueprint for the physical object. The model is then sliced into thin horizontal layers, which the 3D printer builds sequentially, from the bottom up, to form the final product.

The advent of 3D printing has revolutionized many industries, including aerospace, automotive, healthcare, and consumer goods, by enabling rapid prototyping, reducing material waste, and allowing for on-demand production. Its ability to produce complex and highly customized parts has opened up new possibilities for innovation and design, making it an invaluable tool for engineers, designers, and manufacturers alike. This technology not only streamlines the production process but also significantly reduces the time and cost associated with developing new products and bringing them to market.

4.2 History of 3D Printing

The history of 3D printing dates back to the early 1980s, marking a significant milestone in the evolution of manufacturing technologies. The concept was first introduced by Dr. Hideo Kodama of the Nagoya Municipal Industrial Research Institute, who applied for a patent in 1980 for a rapid prototyping system. Although Kodama's application did not proceed to commercialization, his work laid the foundation for subsequent developments in the field. In 1984, Charles "Chuck" Hull of 3D Systems Corp. took the technology a step further by inventing stereolithography (SLA), a process that uses ultraviolet light to cure photopolymer resin layer by layer. Hull's invention allowed for the creation of three-dimensional objects directly from digital data, marking the birth of modern 3D printing technology.

The late 1980s and early 1990s saw further advancements with the development of new 3D printing techniques. Selective laser sintering (SLS), invented by Dr. Carl Deckard at the University of Texas, utilized a laser to fuse powdered materials,

expanding the range of materials that could be used in 3D printing. Around the same time, Scott Crump, co-founder of Stratasys, introduced fused deposition modeling (FDM), a method that extrudes thermoplastic filament through a heated nozzle. These innovations significantly broadened the applications of 3D printing and paved the way for its widespread adoption.

Throughout the 2000s, 3D printing technology continued to evolve, with improvements in precision, speed, and material diversity. The introduction of desktop 3D printers made the technology accessible to hobbyists and small businesses, democratizing manufacturing and fostering a culture of innovation. By the 2010s, 3D printing had entered the mainstream, with significant reductions in cost and advancements in software and hardware making it a viable option for a wide range of industries. Today, 3D printing is used for everything from prototyping and tooling to the production of end-use parts, and its impact continues to grow as new materials and techniques are developed. (26)

4.3 Basic methods of 3D Printing

3D printing encompasses a diverse array of technologies, each with its unique advantages, disadvantages, and material compatibilities. Understanding the different methods is crucial for selecting the right technology for specific applications. The primary methods of 3D printing include:

4.3.1 Stereolithography (SLA)

Stereolithography (SLA) 3D printing, a leading resin-based additive manufacturing technique, is recognized for its precision, isotropy, and the ability to produce watertight prototypes and functional parts. This technology excels in creating components with intricate details, advanced material properties, and superior surface finishes, making it a critical tool in various industries.



Figure 4.1: Form 1+ SLA 3D Printer

Overview of Stereolithography (SLA) 3D Printing

Stereolithography, also known as vat photopolymerization or resin 3D printing, is an additive manufacturing process where liquid resin is cured into solid plastic using a light source. Among various 3D printing technologies, SLA is distinguished by its remarkable speed, resolution, accuracy, and smooth surface finish. Additionally, the diversity of materials available for SLA, including resins with optical, mechanical, and thermal properties comparable to traditional thermoplastics, enhances its utility across numerous applications. Recent advancements in hardware, software, and material sciences have significantly increased the accessibility and affordability of SLA technology, transforming approaches to prototyping, testing, and small-scale production.

SLA 3D printed parts are now integral to many industries, serving as end-use products, industrial components, manufacturing aids, tooling, and more. The smooth surface finish, tight tolerances, and watertightness of SLA parts make them particularly suitable for applications requiring high precision, such as multi-part assemblies, consumer-grade products, and final design evaluations.

The increased accessibility and affordability of SLA technology have enabled even small businesses to incorporate high-quality 3D printing in-house. This shift has resulted in reduced operational costs, improved efficiency, and the opportunity to explore innovative business models. The SLA process involves curing light-sensitive resins with a light source—a method that has evolved from its initial top-down configurations to more efficient techniques, such as inverted stereolithography. This evolution has allowed for more efficient layer curing and larger print sizes, expanding the scope of SLA's applications.

In SLA printing, thermoset resins are solidified through polymerization, a process initiated by light. Over the last decade, several resin 3D printing techniques have been developed, differentiated primarily by their light sources, including laser-powered SLA, digital light processing (DLP), and masked stereolithography (MSLA). Regardless of the specific method, the SLA printing process generally involves straightforward steps: post-printing processes such as washing the part to remove excess resin and post-curing to optimize material properties are essential. Additional post-processing techniques, such as coloring, coating, or plating, can further enhance the printed part for specific applications.

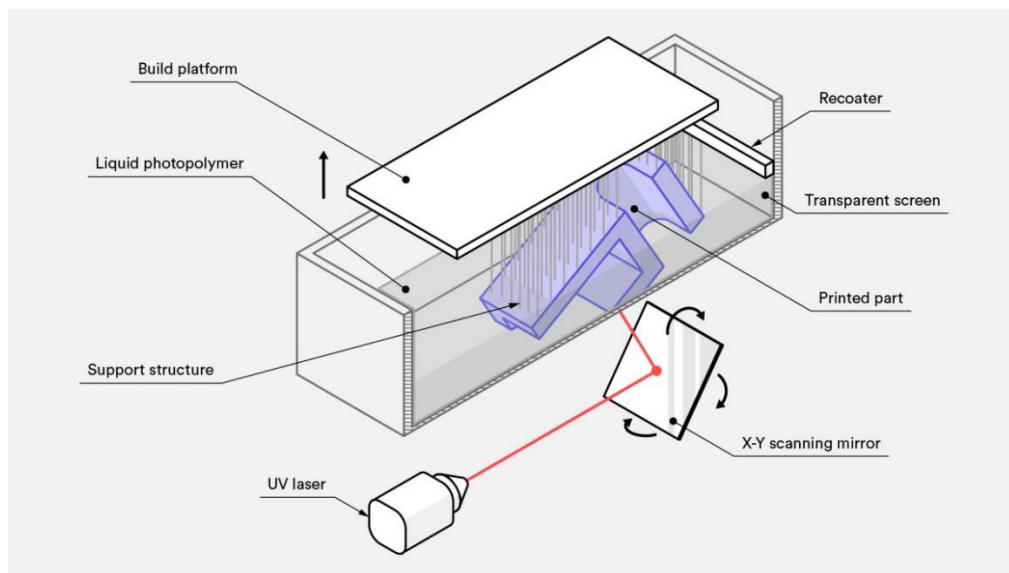


Figure 4.2: Schematic SLA 3D printing illustration

The Impact of Desktop SLA 3D Printers

The development of desktop SLA printers marked a significant turning point in the industry, offering high-resolution 3D printing in a more compact and cost-effective format. The introduction of the first inverted stereolithography solutions democratized access to advanced 3D printing technology. Subsequent advancements, including a wider range of materials and improved print quality, have made SLA 3D printing accessible to professionals across diverse fields such as engineering, product design, and manufacturing, as well as specialized sectors like dental and jewelry.

As the range of applications for SLA 3D printing has expanded, the technology has become one of the most established plastic 3D printing processes, alongside fused deposition modeling (FDM) and selective laser sintering (SLS).

In recent years, innovations in SLA have continued to advance the technology. The introduction of low-force stereolithography techniques, for example, has improved surface quality and print accuracy by reducing the mechanical forces exerted on parts during printing. Such advancements have also facilitated the use of production-ready materials, including soft, flexible resins and highly rigid materials.

SLA 3D Printing Workflow

1. Design

The process begins with the design of the model using CAD software or 3D scan data, which is then exported in a 3D printable file format, typically STL or OBJ. This design is imported into print preparation software, where print settings are adjusted, and the model is sliced into layers.

2. Print

The sliced model is sent to the printer, which cures the resin layer by layer to create the part. Inverted SLA printers typically feature removable resin tanks and build platforms, facilitating easy material changes and preparation for new prints. Advanced systems often include automatic material refills, allowing for unattended printing.

3. Post-Process

Once printing is complete, the part is removed from the build platform, usually requiring scraping. The printed part is then washed in a solvent, such as isopropyl alcohol, to remove any uncured resin. A post-curing process may be necessary to enhance the material's strength and performance. Final steps include removing supports, sanding, and any additional post-processing, such as machining, painting, or coating, depending on the application.

Advantages of SLA 3D Printing

SLA 3D printing is preferred by professionals for its ability to rapidly produce parts with fine features, smooth surfaces, high precision, accuracy, isotropy, watertightness, and material versatility.

- **Speed and Throughput**

Among 3D printing technologies, SLA is one of the fastest, with significant advances in hardware and materials driving industry-leading print speeds. For example, parts can be built at speeds up to 100 mm per hour, with most prints completed in a few hours. This rapid production capability allows for multiple iterations within a single day, enabling a level of throughput that rivals traditional manufacturing methods like injection molding.

- **Material Versatility**

SLA resins offer a wide range of properties, from soft and flexible to highly rigid, with some resins containing secondary materials like glass or ceramic. While not directly comparable to traditional thermoplastics such as nylon or ABS, these resins exhibit similar mechanical and aesthetic properties, making them suitable for a diverse array of applications.

- **Accuracy and Precision**

The high accuracy and precision of SLA 3D printing are essential in industries where exact specifications are critical, such as manufacturing and dentistry. The accuracy of SLA printing is influenced by factors such as the quality of the light source, the precision of the components, and the properties of the material used. Consistent printing conditions minimize errors due to thermal expansion and contraction, ensuring reliable and repeatable results.

- **Fine Features and Smooth Surface Finish**

SLA technology is particularly well-suited for creating parts with fine details and smooth surface finishes, often requiring minimal post-processing. The surface quality of SLA-printed parts can closely resemble that of traditionally manufactured components, making it an ideal choice for end-use products and rapid tooling.

- **Isotropy**

SLA printing produces highly isotropic parts, characterized by uniform strength in all directions. This isotropy results from the chemical bonding that occurs between resin layers during the printing process, leading to parts with consistent and predictable mechanical properties, which is critical for functional applications.

- **Watertightness**

SLA printing produces parts that are continuous and watertight, a feature particularly valuable in applications involving fluid or air flow. Watertightness is crucial in industries such as automotive, biomedical research, and consumer product design, where controlled flow and pressure resistance are necessary. SLA technology enables the production of watertight enclosures and parts capable of withstanding pressurized environments, challenging the misconception that 3D printed parts are inherently porous.

SLA 3D Printing Materials

The materials used in SLA 3D printing offer a wide array of optical, mechanical, and thermal properties, comparable to those of standard, engineering, and industrial thermoplastics. These include resins specifically formulated for particular needs, such as electrostatic discharge or flame

retardancy, as well as those mimicking the properties of traditional plastics like ABS or PEEK. Additionally, some SLA resins enable the production of parts with characteristics similar to silicone, polyurethane, or ceramic. SLA technology also provides the broadest selection of biocompatible materials, greatly expanding its applications in medical and end-use products.

The choice of SLA materials varies by manufacturer and printer, with each offering a unique range of options tailored to specific applications, from mass-customized consumer goods to surgical tools and dental appliances.

General Purpose Resins

These resins are designed for consistency and speed across a variety of industries, with options ranging from matte greyscale resins for design prototypes to clear resins for transparent models. Advanced general-purpose resins offer improved performance, enabling faster production without sacrificing quality. (27)

4.3.2 Fused Deposition Modeling (FDM)

Fused Deposition Modeling (FDM) 3D printing, also referred to as Fused Filament Fabrication (FFF), represents a prominent additive manufacturing (AM) process within the material extrusion category. This technique constructs parts in a layer-by-layer manner by selectively depositing melted thermoplastic material along a predefined path. The process employs thermoplastic polymers, typically provided in filament form, to create the final physical structures.

FDM is the most widely adopted 3D printing technology globally, constituting the largest installed base of 3D printers across various industries. It is often the first technology that comes to mind when discussing 3D printing. This chapter delves into the fundamental principles and essential characteristics of this widely used additive manufacturing process.



Figure 4.3: Creality Ender 3 S1 PLUS FDM 3D printer

Working Principles of FDM 3D Printing

FDM 3D printers operate by depositing melted filament material onto a build platform in a sequential, layer-by-layer fashion, ultimately forming the complete part. The process initiates with the upload of digital design files to the printer, which then translates these files into physical dimensions. The materials utilized in FDM printing encompass various thermoplastics, including ABS, PLA, PETG, and PEI, which are fed into the machine as filament threads through a heated nozzle.

The printing process begins with loading a spool of thermoplastic filament into the printer. Once the nozzle attains the required temperature, the filament is fed through an extrusion head and nozzle. This extrusion head is mounted on a three-axis system, enabling movement across the X, Y, and Z axes. The printer extrudes the melted material in thin strands, depositing them layer by layer along the predetermined path defined by the digital design. As each layer is deposited, the material undergoes cooling and solidification. In certain configurations, cooling fans attached to the extrusion head facilitate the cooling process.

Multiple passes are required to fill an area, analogous to shading a shape with a marker. After the completion of a layer, either the build platform descends or the extrusion head ascends, depending on the specific printer configuration, allowing the subsequent layer to be initiated. This process continues iteratively until the part is fully formed.

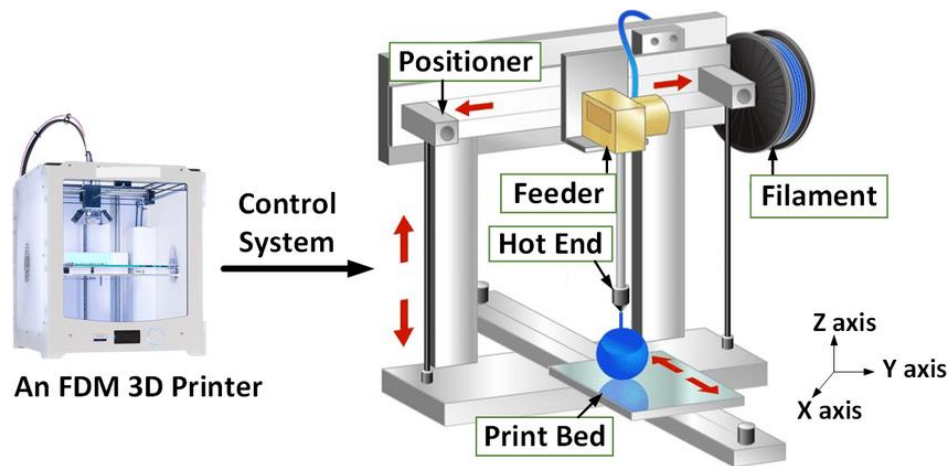


Figure 4.4: Schematic illustration of typical FDM 3D printer (28)

Print Parameters for FDM 3D Printers

Most FDM systems provide the capability to adjust various process parameters, such as nozzle and build platform temperatures, build speed, layer height, and cooling fan speed. While designers typically do not need to directly manage these settings, as they are often handled by an AM operator, it is important to consider factors such as build size and layer height.

For example, the standard build size of a desktop 3D printer is approximately 200 x 200 x 200 mm, whereas industrial machines can achieve build sizes up to 1,000 x 1,000 x 1,000 mm. When utilizing a desktop machine for larger parts, it may be necessary to divide the model into smaller sections, which can then be reassembled post-printing.

The typical layer height in FDM printing ranges from 50 to 400 microns. Shorter layers yield smoother surfaces and more accurately capture curved geometries, although using taller layers can expedite the printing process and reduce associated costs.

Distinctions Between Desktop and Industrial FDM Printers

FDM printers are generally categorized into two primary types: industrial (professional) and prototyping (desktop) machines. Each category is associated with distinct applications and benefits, with the primary distinction between them being the scale of production.

Industrial FDM 3D printers are substantially more expensive than their desktop counterparts, with costs starting at \$50,000 or more. These machines are engineered for high efficiency and power, rendering them suitable for producing tooling, functional prototypes, and end-use parts. Additionally, industrial FDM printers possess the capability to complete larger production runs more rapidly than desktop machines. They are designed for repeatability

and reliability, often producing identical parts with minimal human intervention.

In contrast, desktop FDM printers are more affordable and are typically employed in consumer or at-home applications. These machines require frequent maintenance and calibration by the user and are generally less robust, making them less suitable for large-scale production.

The following **Table 4.1** summarizes the key differences between typical industrial and desktop FDM machines:

Property	Industrial FDM	Desktop FDM
Standard accuracy	± 0.3% (lower limit ± 0.2 mm)	± 0.5% (lower limit: ± 1.0 mm)
Typical layer thickness	0.18 - 0.5 mm	0.10 - 0.25 mm
Minimum wall thickness	1 mm	0.8 - 1 mm
Maximum build envelope	Large (e.g., 900 x 600 x 900 mm)	Medium (e.g., 200 x 200 x 200 mm)
Common materials	ABS, PC, ULTEM	PLA, ABS, PETG
Support material	Water-soluble/Break-away	Same as part (typically)
Production capabilities	Low/Medium	Low
Machine cost	\$50,000+	\$500 - \$5,000

Table 4.1: Industrial and Desktop FDM 3D printer comparison

Characteristics of FDM 3D Printing

While FDM printers exhibit variation in their extrusion systems and the quality of parts produced, several characteristics are common across all FDM processes.

Warping: Warping is a prevalent defect in FDM printing, resulting from differential cooling rates of various sections of the printed part. As the material cools, dimensional shrinkage occurs, leading to internal stresses that can lift layers, causing warping. Preventative measures include close monitoring of build platform and chamber temperatures, as well as enhancing adhesion between the part and the build platform. Design considerations, such as minimizing large flat surfaces and incorporating fillets at sharp corners, can also mitigate the risk of warping.

Layer Adhesion: The adhesion between deposited layers is critical in FDM printing. As molten thermoplastic is extruded, it presses against the previously printed layer, causing it to re-melt and bond with the new layer. However, this process also results in the deformation of the extruded material into an oval shape, contributing to the characteristic wavy surface of FDM parts. Small

features, such as holes or threads, may require post-processing due to this deformation.

Support Structure: Certain part geometries necessitate the use of support structures in FDM printing, typically printed in the same material as the part itself. These supports can be challenging to remove; therefore, designing parts to minimize the need for support structures is advisable. High-end FDM printers may offer dissolvable support materials, although the use of these materials increases the overall cost of printing.

Infill and Shell Thickness: FDM parts are often not printed as solid objects but rather with a low-density internal structure known as infill, surrounded by a solid outer perimeter referred to as the shell. The thickness of the shell and the density of the infill significantly impact the strength and print time of the part. Desktop FDM printers typically default to a 20% infill density and a 1 mm shell thickness, balancing strength and speed for quick prints.

The following **Table 4.2** summarizes the primary characteristics of FDM 3D printing:

Property	FDM
Materials	Thermoplastics (PLA, ABS, PETG, PC, PEI, etc.)
Dimensional Accuracy	$\pm 0.5\%$ (lower limit ± 0.5 mm) - desktop; $\pm 0.15\%$ (lower limit ± 0.2 mm) - industrial
Typical Build Size	200 x 200 x 200 mm - desktop; 900 x 600 x 900 mm - industrial
Common Layer Thickness	50 to 400 microns
Support	Not always required (dissolvable available)

Table 4.2: Basic properties of FDM 3D printers

Common Materials for FDM 3D Printing

A key advantage of FDM technology, both desktop and industrial, lies in its compatibility with a wide range of materials. These materials include standard thermoplastics such as PLA and ABS, engineering-grade materials like PA, TPU, and PETG, and high-performance thermoplastics including PEEK and PEI.

For desktop FDM printers, PLA is the most commonly used material due to its ease of use and ability to produce parts with fine details. ABS is preferred for applications requiring higher strength, ductility, and thermal stability, although it is more prone to warping, particularly on machines without a heated chamber. PETG offers a balance between ease of use and material strength, making it a suitable alternative to ABS for desktop printing.

Industrial FDM machines primarily utilize engineering thermoplastics, including ABS, polycarbonate (PC), and ULTEM. These materials often contain additives that enhance their properties, making them ideal for industrial applications requiring high impact strength, thermal stability, chemical resistance, and biocompatibility.

The following **Table 4.3** compares the most common FDM materials:

Material	Characteristics
ABS	+ Good strength + Good temperature resistance - More susceptible to warping
PLA	+ Excellent visual quality + Easy to print with - Low impact strength
Nylon (PA)	+ High strength + Excellent wear and chemical resistance - Low humidity resistance
PETG	+ Food Safe + Good strength + Easy to print with
TPU	+ Very flexible - Difficult to print accurately
PEI	+ Excellent strength-to-weight + Excellent fire and chemical resistance - High cost

Table 4.3: Properties of the most common FDM materials

Post-Processing for FDM 3D Printing

FDM 3D printed parts can be refined to a high standard through various post-processing methods, including sanding, polishing, priming and painting, cold welding, and vapor smoothing. (29)

4.3.3 Selective Laser Sintering (SLS)

Selective Laser Sintering (SLS) is categorized under powder bed fusion (PBF) technologies. The process involves the use of a high-powered laser to selectively sinter fine polymer powder particles into a solid form based on a three-dimensional CAD model. The technology's high resolution, efficiency, and material versatility make it particularly well-suited for a diverse array of

applications, ranging from rapid prototyping to the production of end-use parts with intricate geometries.



Figure 4.5: PROTOFAB SLS600 SLS 3D printer

Operational Process of SLS 3D Printing

The SLS process entails the sequential fusion of thin layers of powdered material, typically around 0.1 mm thick, which are uniformly spread across the build area using a counter-rotating leveling roller. The entire process is conducted within a sealed chamber filled with nitrogen or another inert gas, minimizing oxidation and degradation of the powder.

Step 1 – Preheating the Powder:

The powder on the build platform is preheated to just below its melting point or glass transition temperature using infrared heaters positioned above the build area.

Step 2 – Printing of SLS 3D Parts at High Temperature:

Once the powder layer is formed and preheated, a focused CO₂ laser beam scans the powder bed, selectively sintering the material according to the CAD design. The surrounding unsintered powder remains in place, providing support for subsequent layers and eliminating the need for additional support structures. Following the completion of each layer, the build platform is lowered according to the layer thickness specified in the slicing software, and

a new powder layer is evenly distributed and leveled. This process is repeated until the entire part is fabricated.

Step 3 – Cooling and Post-Processing of SLS 3D Parts:

Upon the completion of the printing process, the fabricated parts are carefully extracted from the powder bed, and any remaining loose powder is removed. Further post-processing techniques, such as dyeing, bead blasting, vapor polishing, or media tumbling, may be employed to enhance the surface finish or improve the mechanical properties of the parts.

Material Considerations for SLS 3D Printing

SLS technology is compatible with a wide range of thermoplastic powders, with the most commonly used materials including polyamide (Nylon), polypropylene, and thermoplastic elastomers (TPEs). These materials are generally classified into two categories:

- **Rigid Materials:** This category includes PA 12 (available in various forms, such as regular, glass-filled, flame retardant, food grade, and aluminum-filled), PA 11 (regular and food grade), and Polypropylene (PP).
- **Flexible Materials:** This category includes Flex TPU.

Nylon PA 12 is particularly notable for its excellent mechanical properties, including toughness, tensile strength, and impact resistance, making it a standard material in SLS applications.

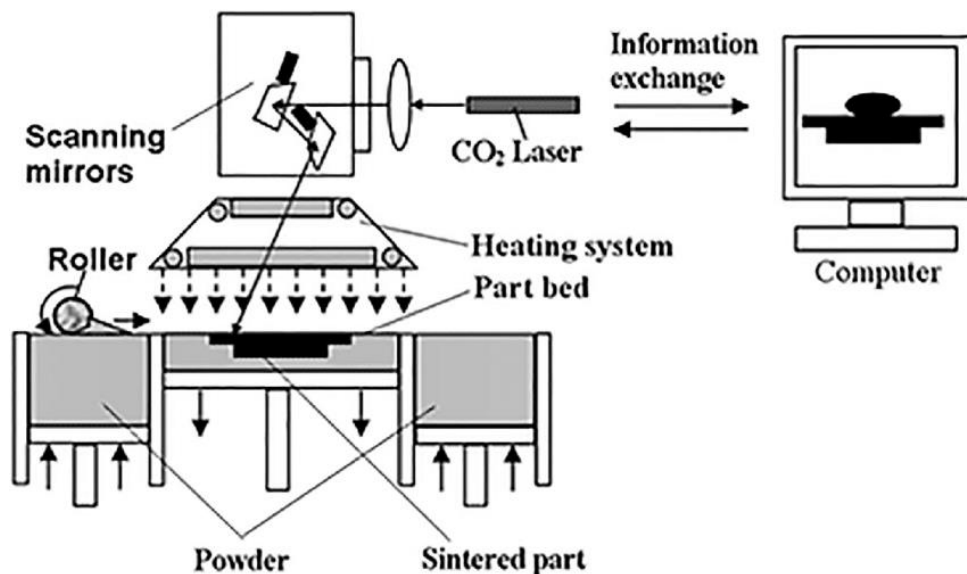


Figure 4.6: Schematic SLS 3D printing illustration (30)

Advantages of SLS Technology in 3D Printing

SLS technology is recognized as one of the most reliable, precise, and efficient methods for prototyping, small batch production, and industrial-grade applications. Several unique advantages contribute to the widespread adoption of SLS:

- **Elimination of Support Structures:** SLS technology, being a powder bed fusion process, inherently does not require additional support structures for complex designs. The unsintered powder supports hollow spaces, overhangs, and thin features during the printing process, offering designers substantial freedom in their design choices.
- **Suitability for Complex Designs:** SLS is particularly well-suited for producing parts with intricate internal components and channels without compromising design integrity. This capability makes SLS a superior choice for complex designs that would otherwise necessitate multiple parts if alternative technologies, such as Fused Deposition Modelling (FDM), were employed.
- **High-Speed Printing:** SLS is one of the fastest 3D printing technologies available, as the polymer powders require minimal laser exposure to achieve sintering. Unlike other technologies, where speed often results in a compromise in resolution, SLS maintains high resolution even at accelerated printing speeds.
- **Enhanced Dyeing and Coloring:** The porous surface of SLS-printed parts makes them particularly amenable to dyeing. The hot bath dyeing process is highly effective, as the porous structure facilitates efficient color absorption.
- **Superior Mechanical Properties:** SLS parts exhibit strong interlayer adhesion, resulting in isotropic properties, meaning that tensile strength, hardness, and elongation are consistent across all axes. This makes SLS parts a viable alternative to traditional injection-molded plastic components, offering good chemical resistance as well.

Disadvantages of SLS Technology in 3D Printing

Despite its many advantages, SLS technology also presents certain limitations:

- **Porosity and Brittleness:** While SLS parts possess good tensile strength, they are generally less flexible and more prone to brittleness. The porosity that enhances dyeing capabilities also compromises the structural integrity of the parts, making SLS prints more suitable for prototypes than for functional, load-bearing components.
- **Significant Shrinkage:** SLS parts are subject to considerable shrinkage during the cooling process, leading to potential dimensional inaccuracies. The shrinkage rate can be as high as 3% to 4%, which is greater than that of other 3D printing methods. This phenomenon must

be carefully considered during the design phase to prevent warping or distortion, particularly at sharp edges and corners.

- **Increased Waste Generation:** The SLS process generates a substantial amount of waste due to the preheating requirement for the powder in the build chamber. Preheating can cause partial fusion of powder grains outside the fabricated part, diminishing the quality of the remaining powder. Consequently, SLS produces more waste compared to other technologies, such as HP Multi Jet Fusion (MJF), which does not require powder preheating. Additionally, loose nylon powder can pose respiratory hazards, necessitating appropriate protective measures. (31)

4.3.4 Digital Light Processing (DLP)

Digital Light Processing (DLP) 3D printing is distinguished by its superior precision and efficiency, stemming from its foundational digital light projector technology. This innovative method has significantly transformed the realms of model creation and prototyping, enabling unprecedented levels of detail and accuracy. DLP 3D printing employs a vat polymerization technique where a digital micromirror device (DMD) projects light to cure photopolymer resin in a vat. The DMD comprises thousands of micromirrors that pivot to precisely direct UV light onto the resin, enabling the creation of highly detailed parts with exceptional surface smoothness, often surpassing other 3D printing technologies.



Figure 4.7: Flashforge DLD 3D printer

Operational Mechanism of DLP 3D Printing

The process begins with the creation of a digital model, which is then sliced into thin horizontal layers. Each layer represents a cross-sectional area of the model. The DLP projector displays these layers onto the resin's surface, causing localized curing and solidification of the resin. As each layer solidifies, the build platform incrementally moves to allow the application of a new resin layer. This sequence is repeated until the object is fully formed.

Key Components in DLP 3D Printing

- **Voxel:** A voxel, or volumetric pixel, represents the smallest unit of a 3D print, analogous to pixels in digital images. Each voxel in DLP printing corresponds to a point in three-dimensional space, crucial for achieving high resolution and detailed internal structures.
- **Digital Light Projector Screen:** This component, utilizing a DMD with numerous mirrors, projects the light patterns required to cure the resin.
- **Vat:** The vat holds the liquid photopolymer resin, with a transparent bottom that allows UV light to pass through and cure the resin. Proper maintenance of the vat is essential for consistent print quality.
- **Build Platform:** This is the surface on which the resin cures and the object is formed. It moves incrementally to accommodate each new layer of resin.
- **Elevator:** This mechanism controls the vertical movement of the build platform, ensuring accurate layer positioning and UV exposure.

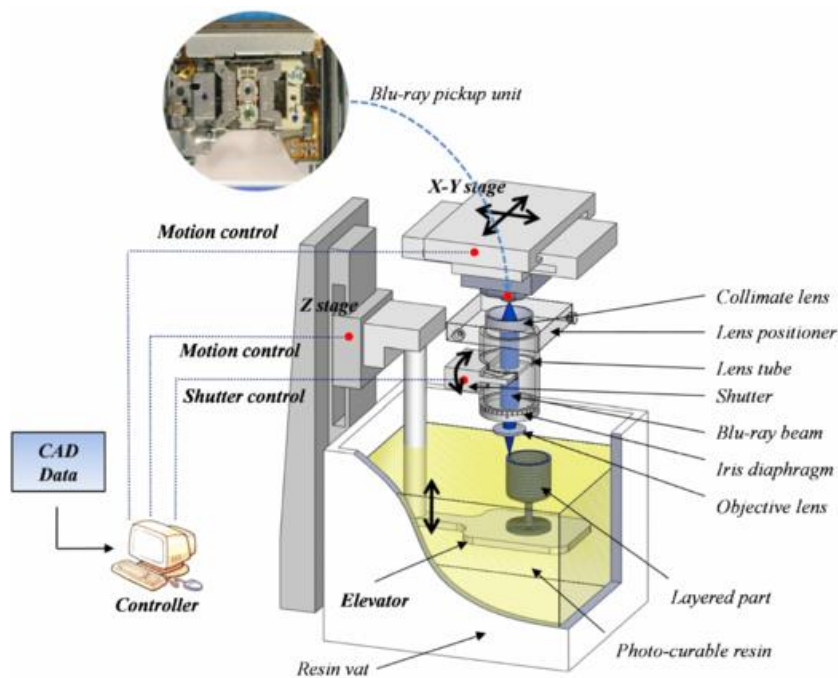


Figure 4.8: Schematic DLP 3D printing illustration

Stages of a Typical DLP 3D Printing Process

1. **Design Creation and Preparation:** A digital model is developed and sliced into layers using 3D modeling software.
2. **Resin Tank Preparation:** The resin tank is filled with photopolymer resin, ready for the printing process.
3. **Build Platform Calibration:** Calibration ensures proper adhesion and alignment of layers.
4. **Layer-by-Layer Printing:** The DLP projector cures each layer of resin, with the build platform moving to accommodate new resin.
5. **Build Plate Movement:** The platform moves incrementally to position each new resin layer.
6. **Repeating the Exposure Process:** The projection and curing process continues until the object is fully printed.
7. **Washing:** The printed object is washed to remove uncured resin.
8. **Curing:** The object undergoes UV curing to enhance mechanical properties and stability.
9. **Support Removal and Finishing:** Supports are removed, and the object may be sanded or finished for improved surface quality.
10. **Quality Inspection and Testing:** The final object is inspected for defects and tested to ensure it meets specifications.

Technical Characteristics of DLP 3D Printing

- **Printing Speed:** DLP printers offer rapid printing speeds, often producing parts faster than other methods by curing entire layers in a single exposure.
- **Layer Height:** The technology supports precise layer heights between 25 and 100 microns, crucial for detailed parts.
- **Surface Finish:** DLP printers achieve superior surface finishes due to precise curing control.
- **Resolution:** The use of DMDs allows for high-resolution prints with intricate details and smooth surfaces.
- **Support Material:** Effective design and planning are essential for using support structures without compromising the final part's aesthetics.

Post-Processing Requirements

- **Washing:** Post-processing typically involves washing with solvents such as isopropyl alcohol (IPA) or specialized cleaning solutions to remove uncured resin.
- **Curing:** Post-washing, the object is cured under UV light to solidify the resin fully.
- **Support Removal and Finishing:** Supports are removed, and additional finishing processes may be applied to enhance appearance.

- **Quality Inspection and Testing:** The final step involves inspecting the part for defects and conducting necessary mechanical tests.

Material Options for DLP 3D Printing

DLP printing utilizes various photopolymer resins, each tailored for specific applications:

- **Standard Resin:** Versatile and suitable for general prototyping.
- **Tough Resin:** Mimics the strength of ABS plastic, ideal for stress-resistant parts.
- **Flexible Resin:** Provides flexibility for applications requiring bendability.
- **High-Temperature Resin:** Withstands elevated temperatures, suitable for heat-resistant components.
- **Durable Resin:** Offers impact resistance and a glossy finish for high-stress parts.
- **Castable Resin:** Used for investment casting in jewelry, burns cleanly without residue.
- **Water Washable Resin:** Simplifies post-processing by allowing washing with water.
- **Dental Resin:** Biocompatible and designed for dental applications.
- **Ceramic-Filled Resin:** Combines ceramic and polymer properties for high-temperature resistance and stiffness.
- **Clear Resin:** Ideal for applications requiring transparency.

Advantages and Disadvantages of DLP 3D Printing

Advantages:

- **High Resolution and Detail:** Achieved through precise control over UV light.
- **Speed:** Faster than other methods due to simultaneous layer curing.
- **Efficiency:** Minimal material waste and energy consumption.
- **Versatility:** Supports a wide range of resins for various applications.
- **Dimensional Accuracy:** Suitable for applications requiring high precision.

Disadvantages:

- **Limited Material Options:** Compared to other technologies like Fused Filament Fabrication (FFF).
- **Size Constraints:** Build volume may be limited, especially in desktop models.
- **Cost of Materials:** High-quality resins can be expensive.
- **Sensitivity to Light and Oxygen:** Resins may degrade if not handled properly.

- **Messiness:** Post-processing can be cumbersome, involving resin spills and solvent handling.

Applications of DLP Printing

DLP 3D printing is utilized across various industries:

- **Jewelry Making:** Produces intricate molds for metal casting.
- **Dental Industry:** Creates accurate dental models and appliances.
- **Medical Sector:** Manufactures customized prosthetics and anatomical models.
- **Prototype Development:** Facilitates rapid prototyping for product design.
- **Education and Research:** Provides hands-on experience and experimental capabilities.
- **Entertainment and Art:** Enables the creation of detailed figurines and art pieces.

Cost Considerations

- **Resin Costs:** Vary by type, with standard resins costing \$50 to \$100 per liter and specialized resins like dental and castable options ranging from \$100 to \$300 per liter.
- **Printer Costs:** Desktop DLP printers range from \$1,000 to \$5,000, while professional models can exceed \$10,000.
- **Example:** The Raise3D DF2, priced at \$4,999, exemplifies a high-performance DLP printer suitable for precision tasks in prototyping and low-volume production.

Selecting a DLP Printer

Consider the following factors when choosing a DLP printer:

- **Resolution and Precision:** Important for detailed prints.
- **Build Volume:** Affects the size of printable objects.
- **Material Compatibility:** Ensures versatility for different projects.
- **Print Speed:** Impacts productivity.
- **Post-Processing Requirements:** Consider ease of cleaning and curing.
- **Cost and Budget:** Includes initial and ongoing expenses.

DLP vs. SLA Printing

While both DLP and SLA use UV light to cure resins, they differ fundamentally:

- **Resolution and Precision:** SLA generally offers higher resolution.
- **Speed:** DLP is faster due to simultaneous layer curing.
- **Suitability for Large Prints:** SLA maintains detail better for large objects.
- **Durability:** SLA prints may exhibit higher precision and strength.

- **Ease of Use:** DLP printers are often more user-friendly. (32)

4.3.5 Multi Jet Fusion (MJF)

3D printing has significantly transformed the production of objects and prototypes, with Multi Jet Fusion (MJF) emerging as a prominent technology due to its efficiency, precision, and cost-effectiveness. This section delves into the MJF 3D printing process, exploring its operational principles, design considerations, and strategies for optimizing both quality and cost.

The MJF 3D Printing Process

The MJF process integrates inkjet printing with powder fusion techniques. The process begins with a thin layer of thermoplastic powder, typically around 0.1mm in thickness, being evenly distributed across the build platform. This powder serves as the foundation material for the printed object, with layer thickness adjusted according to the required detail and strength of the final product.

An inkjet carriage subsequently moves across the build platform, selectively depositing a fusing agent on the powder, which enables targeted melting and fusion of the particles. This selective fusion ensures that only the intended areas of the powder layer bond together, while the remaining areas remain unaffected. Additionally, a detailing agent is applied along the perimeter to precisely control fusion boundaries.

Following the application of these agents, the build platform is lowered, and a new powder layer is applied, repeating the process until the entire object is fabricated. The result is a strong and durable product, with the capacity to incorporate complex geometries due to the precise application of the fusing agent. This capability makes MJF particularly suitable for diverse applications, including prototyping, manufacturing, and medical use, offering a superior surface finish compared to other thermoplastic 3D printing methods such as Fused Deposition Modelling (FDM) and Selective Laser Sintering (SLS).

One of the key advantages of MJF is its speed. The ability to print an entire build layer simultaneously enhances the efficiency of the process, making it an attractive option for projects with stringent deadlines or requiring high-volume production. This combination of speed and low input costs positions MJF as one of the most cost-effective 3D printing technologies currently available.

Designing for MJF: Key Considerations

Designing for MJF technology necessitates careful attention to specific factors to optimize the final output. Essential guidelines include:

- **Support Structures:** Although MJF supports overhangs and complex geometries, incorporating ribs and gussets is recommended for larger and flat shapes to prevent warping.

- **Wall Thickness:** Maintaining a minimum wall thickness of 0.5mm is critical to ensure structural integrity.
- **Clearance:** A minimum clearance of 0.5mm between moving parts is advised to prevent interference during printing.
- **Orientation:** The orientation of the object on the build platform impacts surface finish and strength; printing at an angle typically yields the best results.
- **Hollowing:** To minimize material usage and reduce costs, hollowing out parts with walls over 1/8" thickness is recommended.
- **Injection Molding Guidelines:** Adhering to traditional design principles, such as consistent wall thickness and the use of fillets and ribs, can enhance part quality in MJF printing.

By following these design principles, one can fully leverage the capabilities of MJF technology to produce high-quality, functional, and durable components.

Cost Optimization in MJF Printing

While MJF is renowned for its high-quality outputs, several strategies can further enhance its cost-effectiveness:

- **Batch Printing:** Combining multiple objects into a single print run maximizes build volume utilization, reducing material waste and overall costs.
- **Hollowing:** Reducing internal material in designs lowers material consumption, directly contributing to cost savings.
- **Material Selection:** Choosing the appropriate material for each project, balancing performance requirements with cost, is crucial for optimizing overall expenses.

These strategies not only help manage costs but also open up new possibilities for exploring the full potential of MJF technology. (33)

4.4 Advantages and Disadvantages of 3D Printing Methods

3D Printing Method	Advantages	Disadvantages
SLA	+ High resolution and accuracy + Smooth surface finish + Wide range of materials with different properties	- Expensive materials - Brittle parts - Post-processing requirements
FDM	+ Cost-effective and widely available materials + Robust and reliable technology	- Lower resolution - Visible layer lines - Material limitations - Warping issues
SLS	+ No support structures needed + High durability and strength	- High cost - Rough surface finish

	+ Capable for complex geometries	- Post-processing requirements
DLP	+ High resolution and detail + Faster printing times + Wide range of available resins	- Resin brittleness - Post-processing requirements - Projector maintenance and calibration
MJF	+ Excellent mechanical properties + High speed and efficiency + Fine details + Smooth surface finish	- High cost - Limited material options - Processing options requirements

Table 4.4: 3D printing methods advantages and disadvantages

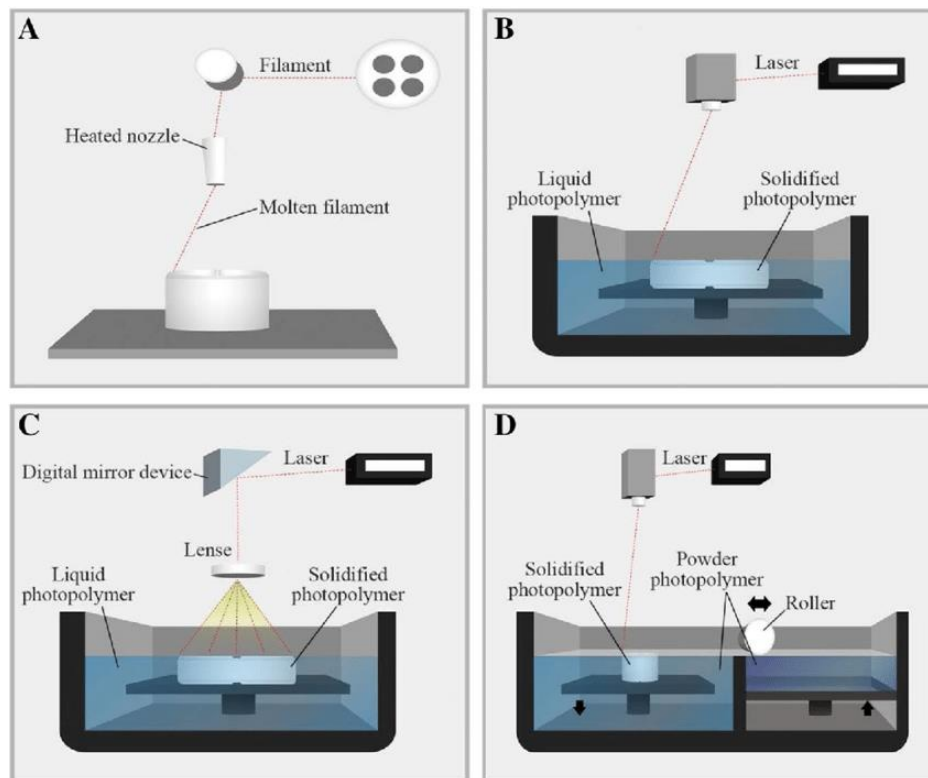


Figure 4.9: Schematic DLP 3D printing illustration (A FDM printer, B SLA printer, C DLP printer, D SLS printer) (34)

4.5 3D Printing in Medicine

The American Society for Testing and Materials (ASTM) International Committee F42 has standardized the term additive manufacturing (AM) to describe methods that create physical objects from three-dimensional (3D) digital data through a process of joining materials layer by layer, as opposed to subtractive manufacturing techniques. Commonly referred to as 3D printing, AM involves computer-automated manufacturing (CAM) processes that fabricate 3D objects from computer-aided design (CAD) models. This method, which can utilize various materials such as

powders, plastics, ceramics, metals, liquids, or even living cells, is highly versatile, precise, and cost-effective for small-scale production, allowing for the consistent manufacture of customized components. Furthermore, 3D printing facilitates rapid production and enables collaboration between medical professionals and researchers by allowing them to share and recreate physical objects with high accuracy.

The technology, history, and operation of 3D printers have been well-documented elsewhere. This thesis focuses on the medical applications of 3D printing, presenting recent research and discussing its implications. The research is categorized into distinct medical applications, each of which is briefly outlined below:

Surgical Planning:

3D printing has emerged as a valuable tool in surgical planning, particularly for complex organs such as the brain or heart, and anatomical structures like the pelvis or spinal cord. By creating 3D models, surgeons can study affected organs prior to surgery, explore various approaches, and gain hands-on experience, ultimately reducing operation time and improving surgical outcomes.

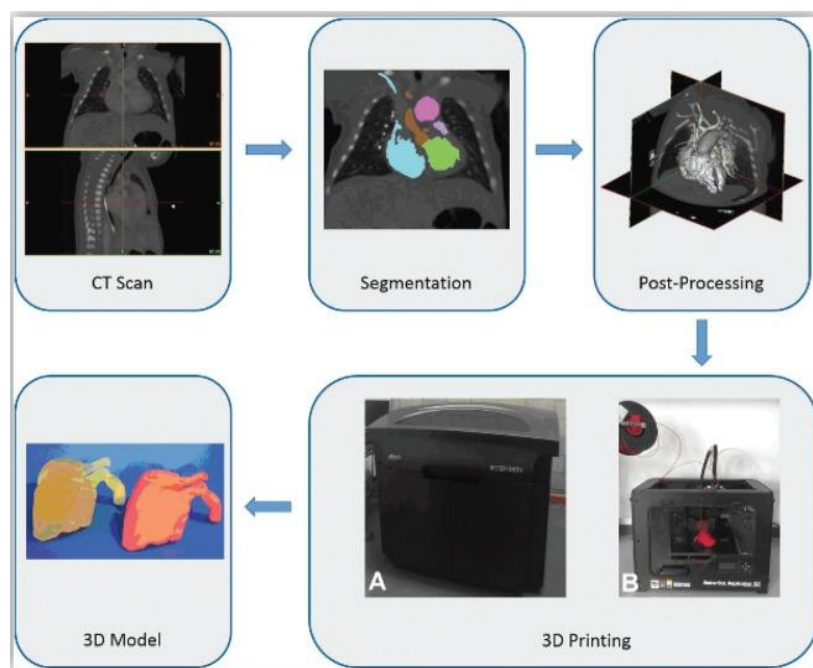


Figure 4.10: Steps of 3D printing a personalized organ (35)

Prosthetics:

Recent advancements in 3D-printed, patient-specific prostheses have enabled many individuals with disabilities—whether due to accidents or congenital deformities—to lead normal lives. High-quality imaging and 3D printing technology have facilitated the creation of precise anatomical prosthetics for various medical applications, significantly impacting fields such as dentistry.



Figure 4.11: Personalized 3D printed skull patch by Protolabs

Medical Education and Training:

The use of cadaveric materials for training novice medical professionals has raised ethical and cost concerns. 3D printing offers a novel alternative by reproducing accurate anatomical structures from high-resolution CT imaging, providing valuable training tools, especially in cases where cadaver use is impractical. Additionally, 3D printing allows for the reproduction of anatomical models in various sizes, enhancing training opportunities.

Medical Research:

Advances in 3D printing technology have enabled the creation of cell structures for toxicity testing and the development of new treatments for diseases and tumors. The ability to print tissues that closely replicate the cellular arrangement of natural tissues accelerates the research process and improves the accuracy of preclinical testing.

Organ Printing:

While 3D printing is already used to produce human organ and tissue structures for research, its potential extends to printing organs for transplantation or even printing organs in-situ during surgery. Although this technology is still in its early stages, it holds the potential to revolutionize medicine by making organ transplants and synthetic artificial organs obsolete.



Figure 4.12: Personalized 3D printed soft tissue by Geetech

Drug Delivery:

3D printing is poised to transform drug delivery by enabling the production of personalized medications. Drugs can be printed in specified doses with multiple release layers, allowing for customized treatment regimens. Additionally, 3D-printed drug delivery devices that fit precisely to a patient's anatomy are under development.

The wide-ranging applications of 3D printing in medicine highlight its transformative impact. Given the rapid pace of innovation, a comprehensive review of all applications is challenging. However, this thesis examines recent developments (from 2014 to the present) across the defined categories to illustrate the current state of the art.

Latest Developments by Application:

Surgical Planning:

Recent studies have demonstrated the utility of 3D printing in surgical planning for complex conditions, such as congenital heart defects and pelvic fractures. By creating accurate 3D models from CT scan data, surgeons can improve preoperative planning, reduce operation time, and enhance surgical outcomes.

Prosthetics:

3D printing has enabled the production of cost-effective, patient-specific prosthetics, including those for cranial implants and tissue-mimicking materials. These innovations have the potential to revolutionize prosthetic design and fabrication, offering improved esthetic and functional outcomes for patients.

Medical Education and Training:

Researchers have developed cost-effective methods for creating realistic and deformable 3D-printed models for medical training, including brain models. These

models provide valuable training tools for surgical planning and medical education, offering an alternative to traditional cadaveric materials.

Medical Research:

Advancements in 3D printing have facilitated the creation of more accurate models for studying diseases such as cancer. The integration of microfluidics with 3D bioprinting is a growing area of interest, with the potential to create complex tissue structures and advance the development of functioning artificial organs.

Organ Printing:

While the printing of full-scale biological organs remains a distant goal, recent progress in bioprinting heart valves and “mini-livers” demonstrates the potential of 3D printing in organ fabrication. Challenges remain, particularly in achieving the necessary structural integrity for functional organs.

Drug Delivery:

3D printing offers significant promise for personalized drug delivery systems, enabling the creation of customized drug delivery devices and tablets with controlled release profiles. As 3D printing technology matures, its application in pharmaceuticals is likely to expand, bringing new possibilities for personalized medicine.

Future Challenges:

For many surgical procedures, 3D-printed models enhance preoperative planning and improve patient outcomes. The ability to produce patient-specific prosthetics, realistic anatomical models for training, and complex tissue structures for research underscores the transformative potential of 3D printing in medicine. However, the printing of full-scale, functional biological organs remains an aspirational goal. While progress has been made in bioprinting cells and simple tissue structures, further advancements in hydrogel matrices, printing techniques, and microfluidic integration are needed to achieve robust artificial organs. Meanwhile, the potential for 3D printing to revolutionize drug delivery is increasingly clear, with personalized drug delivery systems and custom tablet geometries becoming a practical reality.

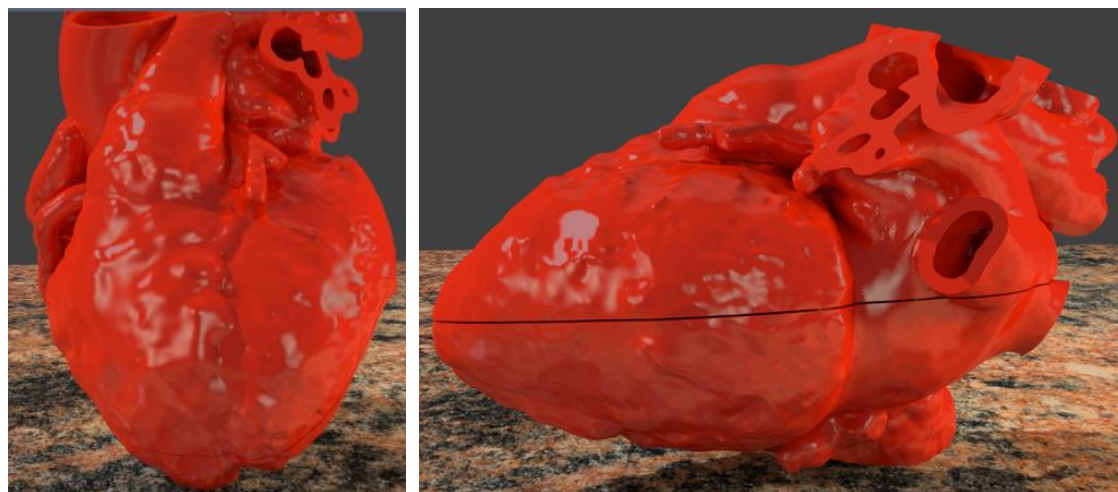
In summary, 3D printing is a powerful tool with the capacity to transform numerous aspects of medicine. While significant advances have been made in surgical planning, prosthetics, medical education, and research, the field continues to evolve, with promising developments in personalized drug delivery and organ printing on the horizon. (35)

4.6 Development of the Cardiac Phantom

The development of a cardiac nuclear medicine phantom was motivated by the prominence of cardiac scintigraphy as the most frequently performed scintigraphy examination. Additionally, in Greece, the only single-photon emission computed tomography (SPECT) systems utilizing the cutting-edge cadmium zinc telluride (CZT) technology are dedicated exclusively to cardiac applications. This unique landscape necessitated the creation of a cardiac phantom to facilitate a comparative analysis between traditional sodium iodide (NaI) crystal photomultiplier tube (PMT) SPECT systems and the innovative CZT-based systems. The following section delineates the comprehensive process undertaken to design, modify, and fabricate the cardiac phantom, from the initial conceptualization to the final 3D-printed model.

Selection of the Heart Model

The initial step in developing the cardiac phantom involved selecting a realistic human heart model that could serve as an accurate anatomical basis for the phantom. A suitable heart design was procured from [Embodi3D](#), a reputable repository for 3D anatomical models derived from high-resolution medical imaging. The chosen model was a two-piece hollow heart, meticulously reconstructed from a high-quality computed tomography (CT) scan. This bifurcated design allowed for the printing of the heart in two separate halves, facilitating detailed anatomical studies and the visualization of internal structures. Alternatively, the two halves could be fused to create a single, cohesive heart model. The model featured a cut plane along the heart's axis, providing a clear four-chamber view that includes the right and left ventricles, right and left atria, superior vena cava (SVC), inferior vena cava (IVC), pulmonary arteries, and pulmonary veins.



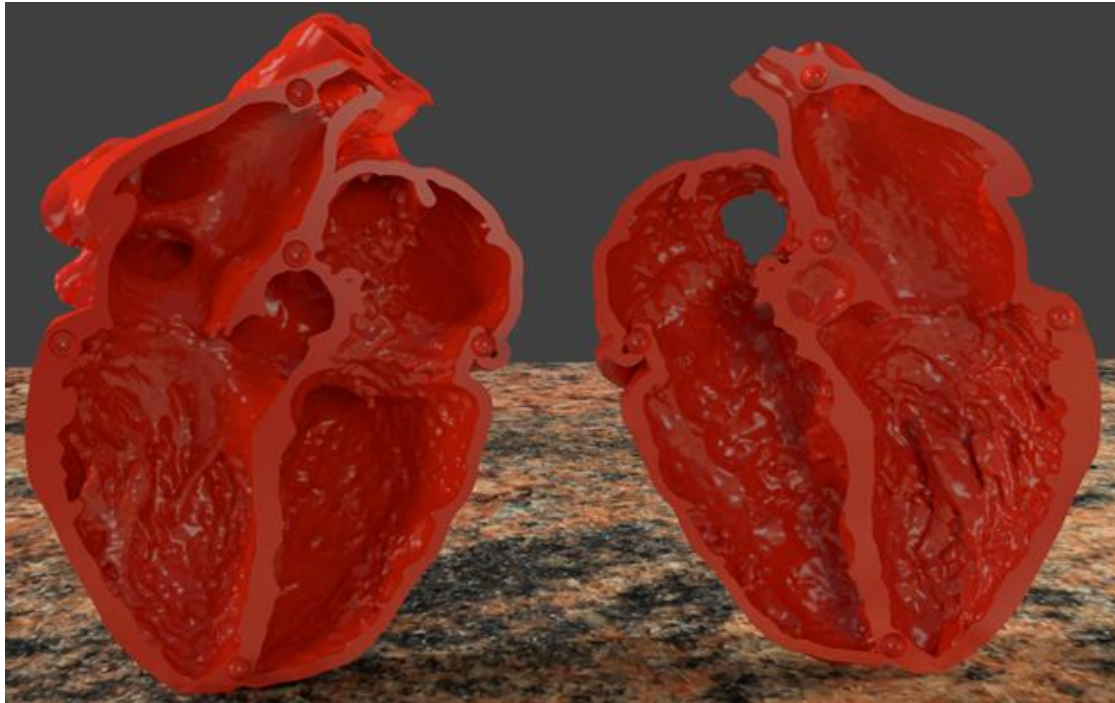


Figure 4.13: Two piece hollow heart model derived from a high quality CT scan

Design Modification and Customization

To tailor the selected heart model for its intended application in cardiac scintigraphy, several modifications were necessary. The software tool Meshmixer was employed to process the original .stl file and customize the model accordingly. The modification process encompassed the following key steps:

1. **Removal of Atria:** In cardiac scintigraphy, the primary focus is on the right and, predominantly, the left ventricles. Consequently, both the left and right atria were excised from the original model to streamline the phantom's anatomy and enhance its relevance to scintigraphic imaging.

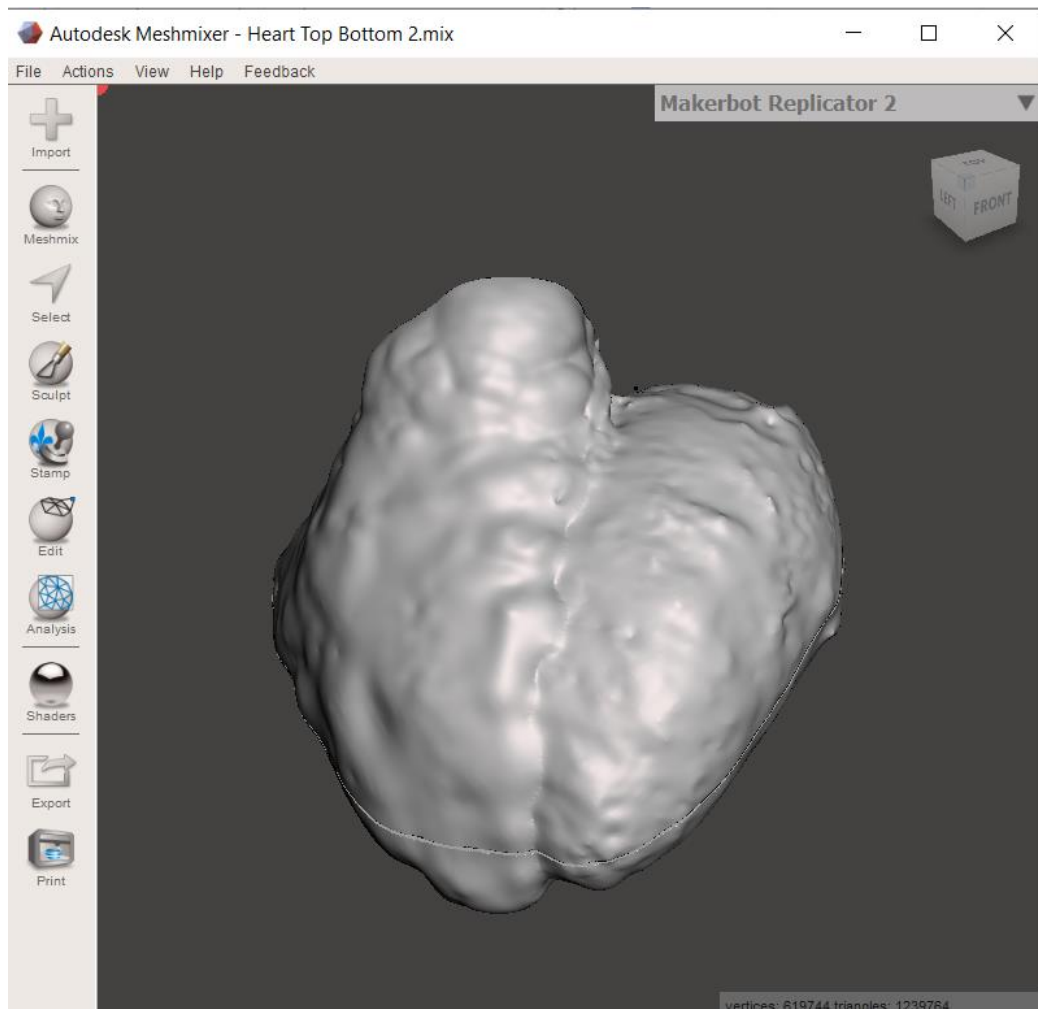


Figure 4.14: Two piece hollow heart model without the atria's

2. **Fusion of Heart Halves:** The two separate halves of the heart model were meticulously fused to form a solid structure comprising only the two ventricles. This fusion was critical in creating a robust and unified phantom suitable for repeated imaging and testing.
3. **Smoothing Geometries:** Both the inner and outer geometries of the fused heart model were smoothed to eliminate any irregularities or artifacts that could interfere with imaging accuracy. This step ensured that the phantom closely resembled the anatomical and surface characteristics of a natural human heart.
4. **Elimination of Coronary Arteries:** The coronary arteries were removed from the model to simplify the phantom's internal structure, focusing solely on the ventricular chambers, which are of primary interest in scintigraphic examinations.

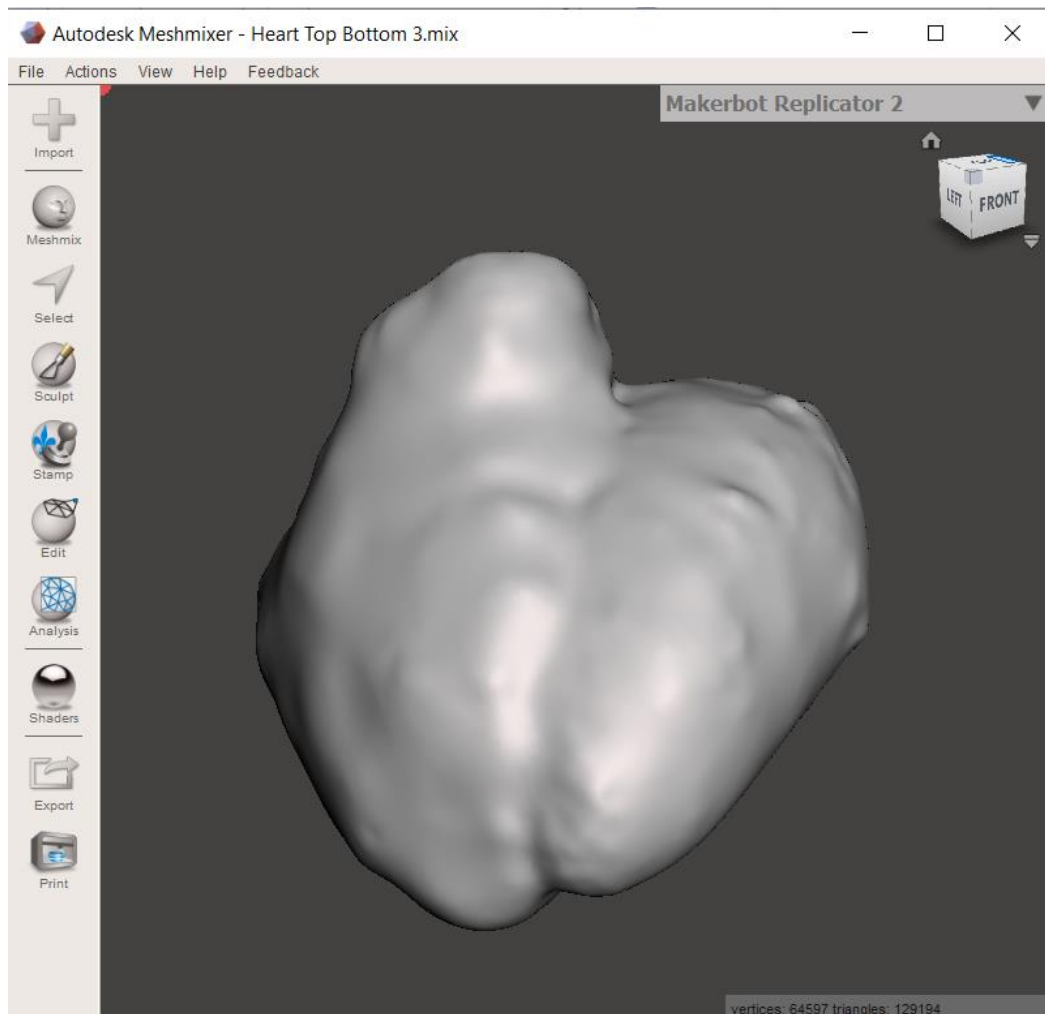


Figure 4.15: One piece smoothed heart model without coronary arteries and the atrias

5. **Creation of Void Spaces:** Utilizing Meshmixer's offset feature, regions corresponding to the cardiac muscle were transformed into void spaces surrounded by a 5 mm thick wall. This modification was designed to accommodate the injection of water mixed with the desired radiopharmaceutical. When the phantom is placed under a SPECT system, these void spaces filled with the radiopharmaceutical solution simulate the physiological distribution of the tracer, thereby producing images that closely mimic those obtained from actual patients.

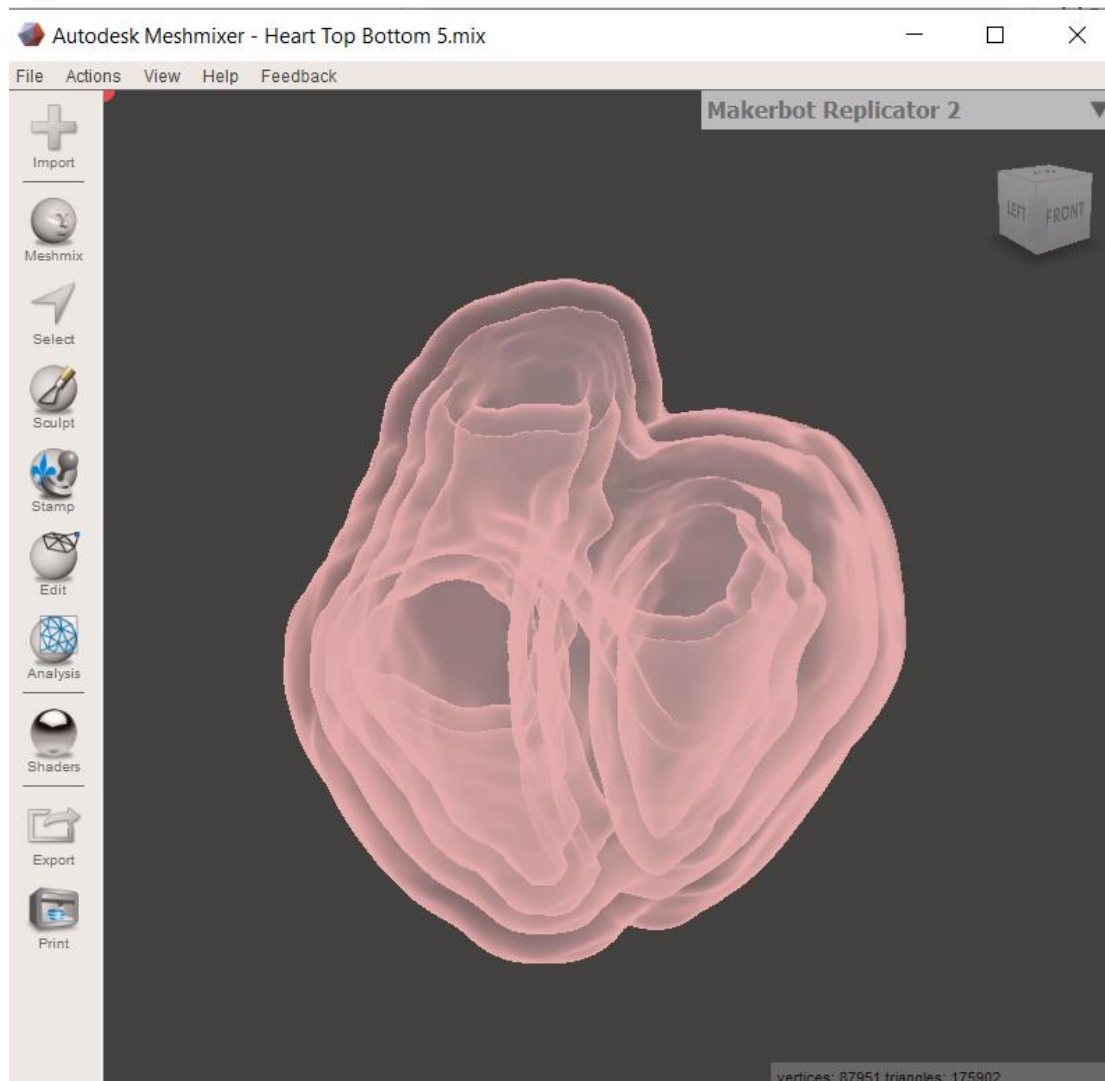


Figure 4.16: One piece hollow ventricular heart phantom

- 6. Incorporation of Artificial Blockages:** To enable the simulation of pathological conditions such as heart attacks, two strategically placed holes were introduced into the phantom. A 7 mm diameter hole was positioned on the top of the phantom for the liquid filling, and a 16 mm diameter hole was located on the left ventricle, which allows for the insertion of blockages, thereby creating artificial infarctions that can be used to evaluate the performance of different SPECT technologies under simulated pathological conditions.

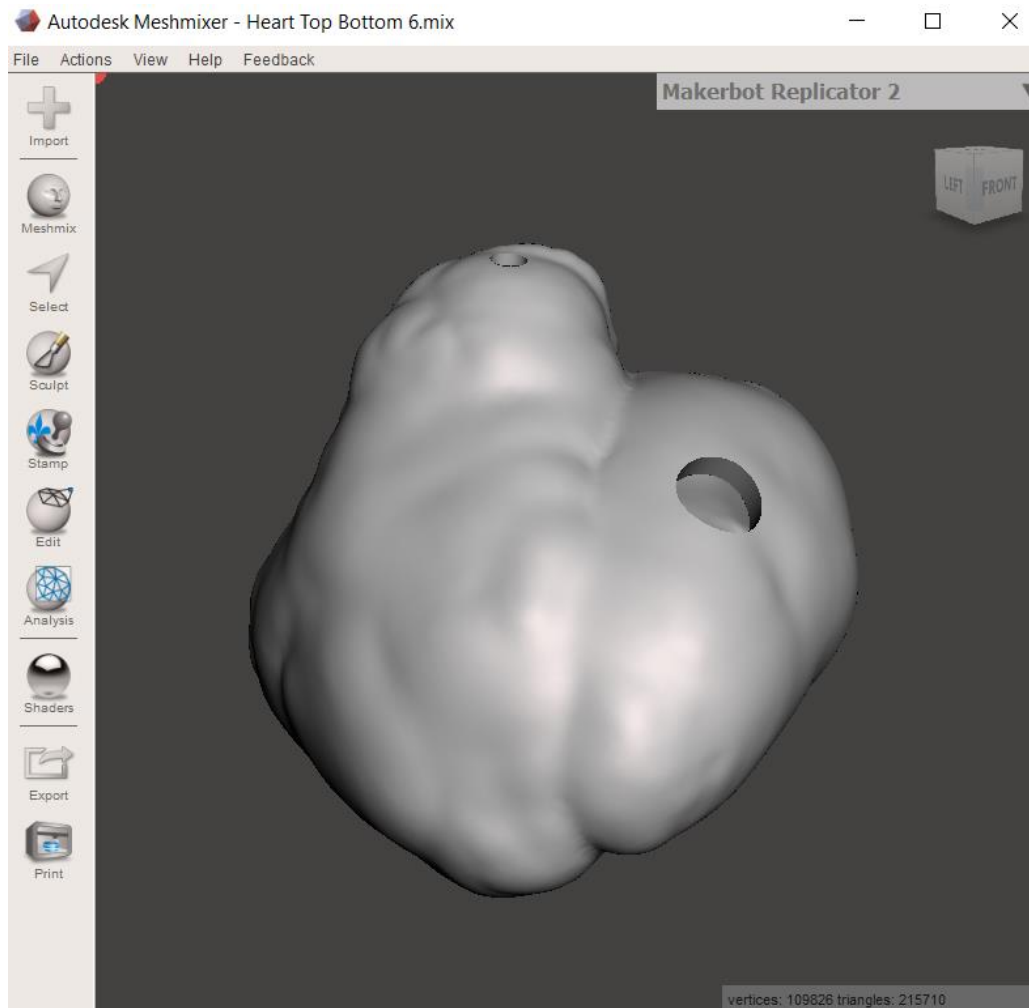


Figure 4.17: One piece hollow ventricular heart phantom with two holes

Construction of Artificial Blockages

To facilitate the simulation of myocardial infarctions and other pathological conditions, specific plugs were created for the two aforementioned holes in the phantom. The first plug, designed for the hole at the top of the phantom, was used primarily for filling the phantom with the radiopharmaceutical solution. The second plug, for the hole in the left ventricle, was crucial for introducing artificial blockages.

In addition to these, five similar plugs were designed specifically for the left ventricle to simulate varying degrees of blockage. The first of these plugs was a simple plug without any attachments, serving as a control. The second plug had a 1.5 mm diameter silicone cylinder placed at its center, simulating a small blockage. The third plug featured a 5 mm diameter cylinder, representing a moderate blockage. The fourth plug incorporated an 8.5 mm diameter cylinder, simulating a more significant obstruction. Finally, the fifth plug was designed with a 12 mm diameter cylinder, creating a scenario of severe blockage.

These varying plug designs allowed for the creation of different blockage sizes within the phantom, providing a versatile tool for assessing the ability of SPECT systems to detect and evaluate myocardial infarctions of varying severity. By testing the phantom with these different plugs, we could simulate a range of clinical scenarios and evaluate the performance of different imaging technologies in detecting and characterizing these blockages.

3D Printing Process

With the design of the cardiac phantom finalized, the next step was to transition the digital model into a physical object through 3D printing. The material chosen for this purpose was clear resin, selected primarily for its optical transparency. This transparency allows for direct visualization of the internal blockages and void spaces within the phantom, which is essential for validating their placement and ensuring accurate simulation of the conditions being studied.

Beyond its optical properties, clear resin offers several other significant advantages. One of the most important is that resin is inherently waterproof, ensuring that the phantom's walls can contain the added radiopharmaceutical solution without any risk of leakage. This waterproof characteristic is crucial for maintaining the integrity of the phantom during imaging procedures, where any leakage could compromise the results.

Additionally, the 3D printing method chosen for this project—stereolithography (SLA)—is particularly well-suited for creating detailed and precise models without the need for internal supports in the void areas of the phantom. Internal supports could interfere with the even diffusion of the radiopharmaceutical, potentially creating artifacts in the acquired images. By using SLA printing with clear resin, we were able to produce a phantom that not only maintains structural integrity and optical clarity but also ensures uniform distribution of the radiopharmaceutical within the void spaces, leading to more accurate and artifact-free imaging results.



Figure 4.18: Final 3D printed cardiac phantom with 4 silicone plugs-blockages

CHAPTER 5th

CARDIAC PHANTOM IMAGING

5.1 General Framework of Cardiac Phantom Imaging

This chapter provides a comprehensive analysis of the nuclear imaging procedures performed on the cardiac phantom developed in this study. A key objective of this chapter is to compare and evaluate the performance of three distinct SPECT systems, each representing a different technological generation in nuclear medicine. This comparison will highlight the advances made in SPECT imaging over the years, with a particular focus on cardiac scintigraphy.

The SPECT systems used in this study include:

1. **SMV DS7 single round head SPECT with Oasis Mirage software:** A legacy analog system from the 1990s, this system which can still be found today in many healthcare sights, has historically been one of the foundational technologies in nuclear medicine and was once widely used for a variety of diagnostic procedures, including cardiac scintigraphy. It offers a baseline for comparison with more modern systems.

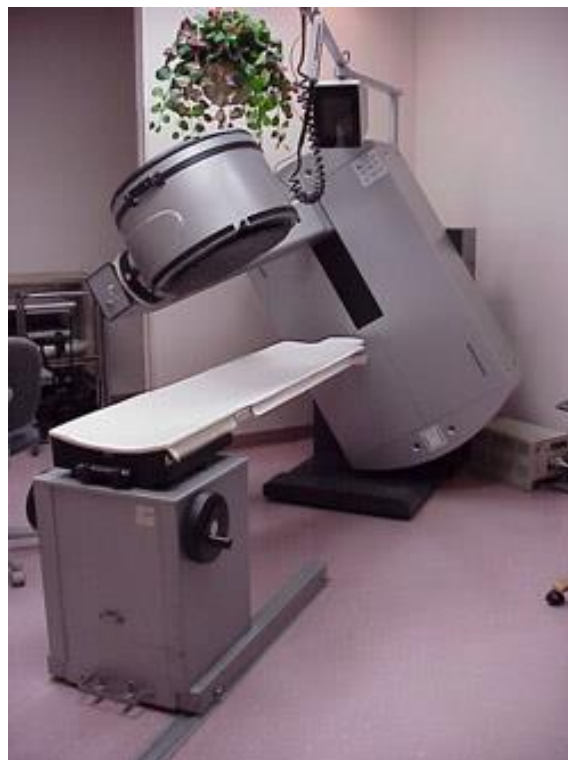


Figure 5.1: SMV DS7 SPECT system

2. **MiE ECAM Dual Head SPECT with SCINTRON software:** Representing a more modern and efficient dual-head system, this technology offers significant improvements in terms of acquisition speed, spatial resolution, and overall image quality. It is widely used in contemporary nuclear medicine settings, making it an ideal candidate for comparison with both older and more advanced technologies.



Figure 5.2: MiE ECAM Dual Head

3. **Spectrum-Dynamics D-SPECT CARDIO 9 column CZT system:** A state-of-the-art, cardiology-specific system, this device utilizes 9 Columns of cadmium zinc telluride (CZT) technology, which represents the cutting edge in SPECT imaging. Its high sensitivity, exceptional image quality, and ability to operate in ultra-low dose environments position it as the most advanced system in this comparison.



Figure 5.3: Spectrum Dynamics D-SPECT Cardio

To facilitate a thorough comparison between these systems, we conducted a series of acquisitions designed to simulate realistic cardiac imaging scenarios. For the **SMV DS7** and **MiE ECAM Dual Head** systems, we performed 20 acquisitions each. These acquisitions were divided into two main categories:

1. Half of the acquisitions simulated a realistic patient heart activity during a typical cardiac scintigraphy procedure, intended to represent the conditions under which these systems are most commonly used.
2. The other half involved a simulation of the cardiac phantom with an activity level approximately 15 times greater than that of a typical patient study. This high-activity simulation allowed for an assessment of the systems' capacity to handle higher radioactivity levels and provided insight into their dynamic range and resolution capabilities.

For the **D-SPECT Cardio** system, which is capable of imaging with ultra-low dose protocols, we performed a total of 15 acquisitions. These were further categorized into three distinct activity levels:

1. Five acquisitions were performed with ultra-low heart activity to assess the system's performance under minimal radiopharmaceutical exposure.
2. Five acquisitions simulated realistic heart activity, comparable to the patient-level simulations conducted on the other two systems.
3. The remaining five acquisitions simulated the high-activity phantom experiment, aligning with the tests performed on the other systems to allow for a direct comparison of the systems' ability to image highly active regions of the phantom.

Each of these experimental conditions and acquisition protocols will be thoroughly discussed in section 5.3, where detailed analyses of the imaging results, data collection methodologies, and post-processing techniques will be presented. By analyzing the performance of these three distinct systems, we aim to assess the technological advancements that have occurred in SPECT imaging over the past few decades, particularly in the context of cardiac scintigraphy.

5.2 Overview of SPECT Systems Employed

This section provides a detailed description of the three SPECT systems utilized for the imaging experiments in this study. Each system represents a distinct era in the development of nuclear imaging technology, offering a unique perspective on how advancements in hardware and software have influenced image quality, acquisition efficiency, and diagnostic accuracy in cardiac scintigraphy. The systems used in this study range from older analog systems with sodium iodide (NaI) detectors to state-of-the-art cadmium zinc telluride (CZT) technology, enabling a comprehensive evaluation of the evolution of SPECT systems.

SMV DS7 Single Round Head SPECT with Oasis Mirage Software

The SMV DS7 is a single-head, analog SPECT system developed in the early 1990s. It uses a round detector head equipped with a sodium iodide (NaI) crystal, coupled with photomultiplier tubes (PMTs). This system represents a landmark in SPECT technology from the 1990s, and although it is dated by today's standards, it remains operational in certain clinical settings.

In terms of its technical capabilities, the SMV DS7 provides an **intrinsic spatial resolution** (full width at half maximum, FWHM) of 6.6 mm in the uniform field of view (UFOV) and 8.3 mm at a 10 cm distance when using a low-energy all-purpose (LEAP) collimator. The **extrinsic spatial resolution** (full width at tenth maximum, FWTM) measures 11 mm at 10 cm, which is consistent with SPECT systems from that era. The **system sensitivity** is around 200 counts per minute per microcurie (cpm/ μ Ci) with the LEAP collimator. The **intrinsic energy resolution** for 140 keV gamma rays is less than 9.9%, which is a reasonable performance for older NaI-based systems.

The **detector crystal** in the SMV DS7 is 9.5 mm thick and has a diameter of approximately 50 cm. The system is equipped with **61 photomultiplier tubes (PMTs)**, arranged in a hexagonal pattern, which aid in the detection of scintillation events. The system boasts excellent intrinsic linearity, with an **integral UFOV linearity** of 0.3 mm and a **differential UFOV linearity** of 0.15 mm, ensuring accurate event localization across the detector surface. Uniformity is similarly well-controlled, with an **uncorrected intrinsic uniformity** of 0.03% integral in UFOV and 0.02% differential.

The Oasis Mirage software used with this system, while somewhat limited by modern standards, allows for basic acquisition and processing of images. The **single-head design**, although slower and less efficient than dual-head systems, still provides valuable information about cardiac perfusion and is used as a baseline reference in this study. Its performance in terms of image resolution, sensitivity, and acquisition time forms an important benchmark against more advanced systems.

MiE ECAM Dual Head SPECT with SCINTRON Software

The **MiE ECAM Dual Head SPECT** system, equipped with **SCINTRON software**, represents a significant improvement over the SMV DS7 in both hardware and software capabilities. The dual-head design allows for faster acquisition times and improved spatial resolution due to the simultaneous collection of data from two angles. This design enhances the system's sensitivity and reduces patient scanning time, making it more suitable for modern clinical environments.

In terms of performance specifications, the MiE ECAM achieves an **intrinsic spatial resolution** of 3.8 mm (**FWHM**) in the central field of view (CFOV) and 4.1 mm in the UFOV at a count rate of 75,000 counts per second (cps). The **FWTM** is measured at 7.8 mm in the UFOV. The system's **energy resolution** (FWHM) for 140 keV gamma rays is less than 9.9% in the UFOV, which is typical of high-quality NaI detector-based systems.

The **intrinsic uniformity** of the ECAM system is excellent, with an **integral flood field uniformity** of 2.9% in the CFOV and a **differential uniformity** of 2.5%, ensuring high image quality and minimal artifacts during acquisition. Additionally, the system demonstrates strong **spatial linearity**, with a **differential UFOV linearity** of less than 0.2 mm. These characteristics contribute to the overall accuracy and reliability of the system for both planar and tomographic imaging.

The **LEHR (Low Energy High Resolution) collimator** used in this system further enhances the spatial resolution, achieving 8.7 mm (**FWHM**) with scatter in the CFOV. The **system sensitivity** with this collimator is ≥ 202 cpm/ μ Ci, which, along with the dual-head design, allows for efficient and effective image acquisition even in low-count scenarios. This makes the MiE ECAM particularly well-suited for handling a wide range of clinical applications, from low-dose imaging to high-activity studies, as well as for conducting comparative analyses in this study.

The **SCINTRON software** offers advanced image processing capabilities, including sophisticated reconstruction algorithms that improve spatial resolution and image contrast. It supports a variety of post-processing techniques, allowing for enhanced interpretation of cardiac scintigraphy results. The software's flexibility and enhanced processing tools make the MiE ECAM a robust system for both routine diagnostic imaging and research applications, positioning it as a versatile tool in this study's comparison of SPECT systems.

Spectrum-Dynamics CARDIO 9 Column CZT System

The Spectrum-Dynamics CARDIO 9 column CZT system is a state-of-the-art SPECT system designed specifically for cardiac imaging. Unlike the NaI-based systems described above, the CARDIO 9 uses cadmium zinc telluride (CZT) detectors, which offer substantial improvements in both sensitivity and spatial resolution. The CZT technology provides excellent energy discrimination and the ability to operate in ultra-low dose environments, making it ideal for modern clinical practices where reducing patient radiation exposure is a priority.

One of the key advantages of the CARDIO 9 system is its superior spatial resolution compared to traditional NaI detectors. The system is capable of producing high-quality images with shorter acquisition times, which not only enhances patient comfort but also improves the overall efficiency of the clinical workflow. The multi-column CZT detector design ensures that data acquisition is both rapid and highly accurate, providing clinicians with exceptional image quality and diagnostic reliability.

In addition to its hardware advantages, the CARDIO 9 system is supported by advanced software algorithms that enable precise image reconstruction and processing. These algorithms allow for better visualization of cardiac structures, improving diagnostic confidence in the detection of coronary artery disease and other cardiac conditions. The system's capability to perform ultra-low dose protocols without sacrificing image quality is a critical feature, particularly in patient populations where minimizing radiation exposure is essential.

In this study, the CARDIO 9 system will be directly compared to the older NaI-based systems, providing valuable insights into the benefits and limitations of CZT technology in the context of cardiac scintigraphy. The results of this comparison will contribute to the broader understanding of how technological advancements have improved the accuracy and efficiency of cardiac imaging.

5.3 Cardiac Phantom Imaging and Processing Experiment

The imaging experiments conducted in this study were designed to evaluate the performance of three different SPECT systems in imaging a cardiac phantom under simulated clinical conditions. The phantom was constructed to mimic the anatomical structure and physiological function of a human heart, with artificial blockages inserted to simulate coronary artery disease. The experiments were divided into two main variations, each designed to assess the systems' ability to detect varying levels of radioisotope activity and identify artificial blockages within the coronary arteries. A third, unique variation was introduced for the CZT-based SPECT system due to its advanced capabilities for low-dose protocols.

5.3.1 Variation 1: Simulating Realistic Heart Activity

In the first variation of the experiment, the cardiac phantom was filled with a solution of water and **Tc-99m** to emulate the radioactivity levels typically found in a human heart undergoing cardiac scintigraphy. Specifically, the activity was set to approximate **1–2% of the total injected activity**, which corresponds to **$0.35 \pm 3\%$ mCi** at the start of the experiment. This configuration represents a realistic clinical scenario where a patient would have low but detectable levels of Tc-99m in their heart, and the primary challenge was to assess the system's ability to resolve the artificial blockages under these low-activity conditions.

The acquisitions were performed in sequential order based on the size of the blockage, starting with the largest blockage and progressing to the smallest, as follows:

1. **First Acquisition – 12 mm Blockage:** The phantom was initially filled with a solution of **$0.35 \pm 3\%$ mCi** Tc-99m, and the largest blockage (12 mm) was inserted. This acquisition was performed on all three SPECT systems, with acquisition times ranging from **20 to 40 minutes** (except from the CZT system where each acquisition lasted 2 minutes), depending on the system's capabilities. This extended acquisition time is typical in clinical practice for low-activity protocols, allowing for the collection of sufficient counts to produce diagnostically useful images. The prolonged acquisition times were a consideration due to the relatively short **half-life of Tc-99m** (approximately 6 hours), necessitating careful planning to maximize the effective use of the isotope before significant decay occurred.
2. **Second Acquisition – 8.5 mm Blockage:** For the second acquisition, the **8.5 mm blockage** was inserted into the phantom without adding more Tc-99m. By this point, the activity had decayed to approximately **$0.30 \pm 3\%$ mCi** due to the passage of time and the inherent decay of Tc-99m. This step simulated a realistic clinical scenario where no additional radiopharmaceutical is administered, and the imaging system must detect blockages with lower radioisotope activity.
3. **Third Acquisition – 5 mm Blockage:** To maintain the original activity level for the third acquisition, the phantom was refilled with Tc-99m, restoring the activity to **0.35 mCi**. This was necessary to evaluate the system's performance at similar activity levels as in the first acquisition, but with a smaller blockage of **5 mm** inserted into the phantom.
4. **Fourth Acquisition – 1.5 mm Blockage:** After the third acquisition, the **1.5 mm blockage** was inserted into the phantom, but this time, no additional activity was added. As a result, the remaining activity was approximately **$0.30 \pm 3\%$ mCi** at this stage. This acquisition challenged the imaging systems to detect a very small blockage under reduced radiopharmaceutical activity.
5. **Final Acquisition – No Blockage:** The final acquisition was conducted without any blockage, using the **plug without blockage** to simulate a healthy coronary artery. No additional Tc-99m was added, meaning the activity at this stage was around **$0.27 \pm 3\%$ mCi**. This acquisition served as a control,

allowing us to evaluate the system’s baseline imaging performance without the presence of any blockages.

This variation was repeated across the three SPECT systems: **SMV DS7**, **MiE ECAM**, and **Spectrum-Dynamics CARDIO 9 CZT**, providing a comprehensive assessment of their capabilities in imaging a low-activity cardiac phantom with artificial coronary blockages. The acquisition parameters and the general reconstruction recommendations for the following two sub-variations were chosen considering the following **Table 5.1** and **Table 5.2** from the Technologist’s Guideline of **EANM** (European Association of Nuclear Medicine)

Isotope	Protocol	Collimator	Energy	Energy window	Rotation	Nr. projections	Angles	Projection time	Pixel matrix	Zoom
^{99m} Tc	1 day	LEHR or LEGP	140 keV	15–20%	180° <i>(360° if 3-head gamma camera)</i>	64 or 128	3–6°; 45° RAO to 45° LPO	1 st acquisition: 25 s/frame	64×64 or 128×128	1.0 <i>(higher if necessary)</i>
	2 day	2 nd acquisition: 20 s/frame						25 s/frame		
²⁰¹ Tl	1 day	LEGP or LEHR	70 keV	20–30%	180° <i>(static images if necessary)</i>	32 or 64		20–25 s/frame		
			167 keV	20%						

Table 5.1: EANM gamma camera and imaging parameters for myocardial SPECT (22)

Filtered back projection					
		Pre-filter			
		Butterworth		Hanning	
Radioisotope	Activity (MBq)	Cut-off ^a (cm ⁻¹)	Order	Cut-off (cm ⁻¹)	α
^{99m} Tc	296–444	0.3–0.4	6	0.30–0.45	0.5
	888–1332	0.4–0.5	6	0.45–0.60	0.5
Iterative					
MLEM	Iterations: 10–15		No prefiltering needed ^b		
OSEM	Iterations: 2–5; Subsets: 8		No prefiltering needed ^b		

Table 5.2: EANM general reconstruction recommendations for myocardial SPECT (22)

5.3.1.1 Imaging the Real Heart Phantom with Acquisition Parameters: 64x64 Matrix, 64 Projections, 25 Seconds per Projection

In this sub-variation of the experiment, we imaged the cardiac phantom using acquisition parameters recommended by the European Association of Nuclear Medicine (EANM). Specifically, the acquisition matrix was set to **64x64**, with **64 projections** and an acquisition time of **25 seconds per projection**. These parameters are frequently used in clinical practice for cardiac SPECT imaging, as they provide a balance between image resolution, acquisition time, and patient tolerance.

Justification for the Reconstruction Method

Among the two available reconstruction methods—**Filtered Backprojection (FBP) with a Butterworth filter (Fc: 0.40, Order: 6)** and **iterative reconstruction**—the **Filtered Backprojection (FBP)** method was chosen for this experiment. The decision to use FBP is supported by its efficiency and compatibility with the **64x64** matrix, which is relatively low resolution compared to higher matrix sizes used in modern systems. FBP, particularly when combined with a **Butterworth filter**, is a well-established technique that provides adequate image quality while minimizing computational demands. This method is also one of the reconstruction techniques proposed by the **EANM** for cardiac imaging, ensuring standardization and clinical relevance.

The Butterworth filter was configured with a cutoff frequency of **0.40** and an order of **6**, which allowed for effective noise reduction without excessively smoothing out critical anatomical details, such as the blockage regions within the cardiac phantom. This balance between smoothing and detail retention was essential for ensuring that

the images accurately represented the phantom's geometry and the artificial blockages.

Comparison of Heart Phantom and Real Patient Images

To assess the realism of the cardiac phantom, images from a real patient's heart and the cardiac phantom were both acquired using the **SMV DS7** system. These images were processed using the same reconstruction method (FBP with Butterworth) and the same software, **Mirage Process**, to ensure consistency. The three standard cardiac views—**Short Axis**, **Vertical Long Axis**, and **Horizontal Long Axis**—were generated for both the real patient and the cardiac phantom, and are displayed in **Figure 5.4**.

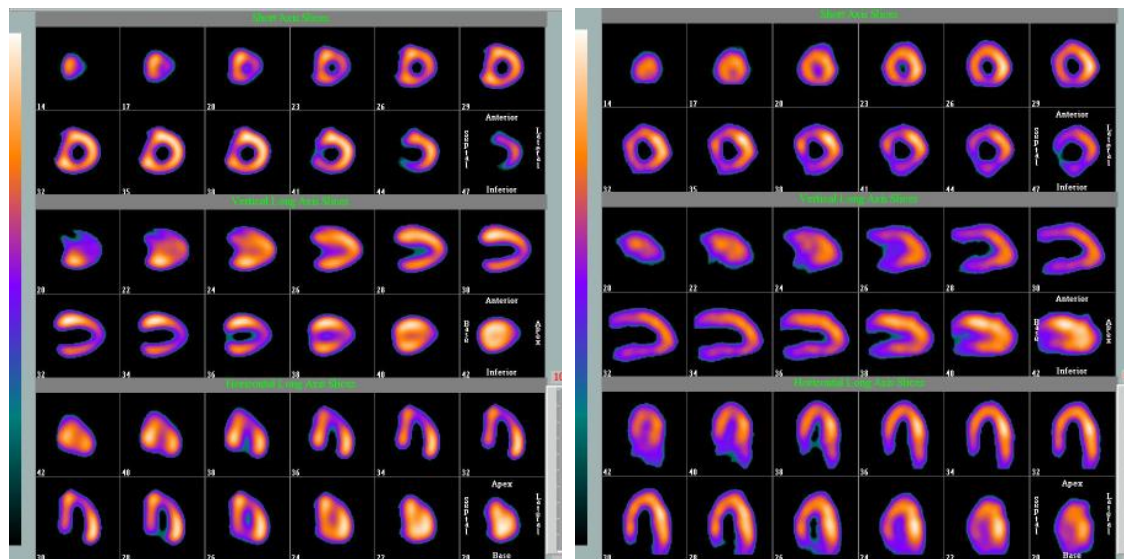


Figure 5.4: Standard cardiac views of the constructed phantom (left) and an actual patient's heart (right)

A visual comparison of these images shows that the cardiac phantom closely mimics the geometry and anatomical structure of a real heart. The phantom's myocardial walls and cavities are well-defined, demonstrating the phantom's suitability for cardiac SPECT imaging experiments. This similarity reinforces the phantom's role in simulating clinical conditions for the purposes of this study.

Imaging the Blockage Variations on SMV DS7

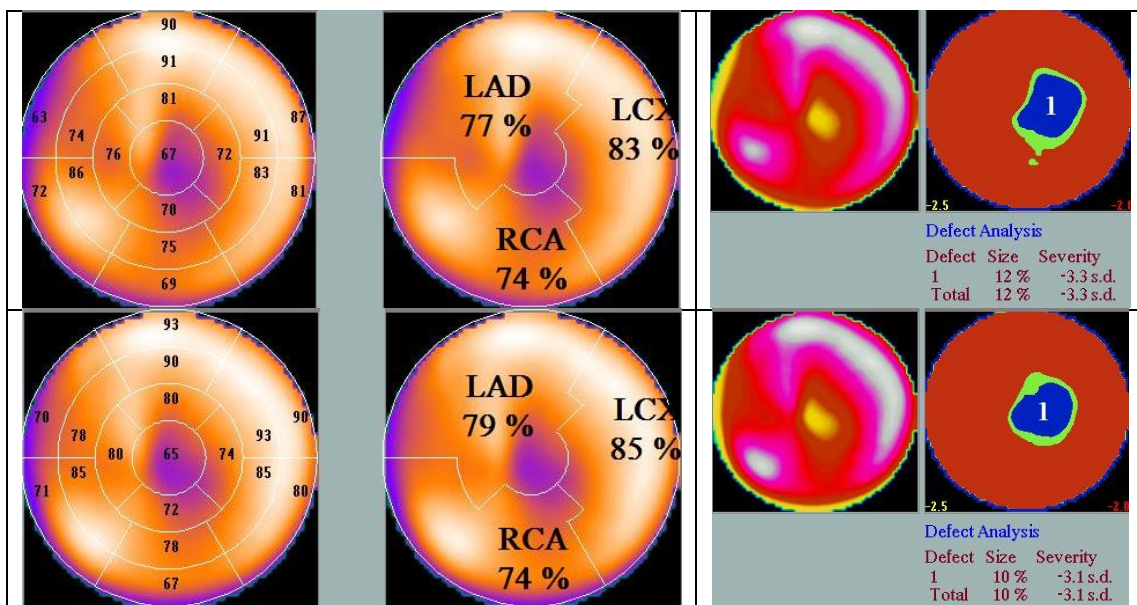
The cardiac phantom was then imaged under five different blockage conditions, ranging from **no blockage** to **1.5 mm**, **5 mm**, **8.5 mm**, and **12 mm** blockages. These acquisitions were performed using the same parameters (64x64 matrix, 64 projections, 25 seconds per projection) and processed with the **Mirage Process** software, ensuring that all images were produced under consistent conditions. The five cases, acquired using the **SMV DS7** system, are shown in **Figure 5.5**. From **Figure 5.5**, a notable decrease in activity is observed across all images, particularly in the apex region, with secondary reductions in areas adjacent to the apex. The most pronounced reduction in

activity is seen in the mainly in the apical and secondarily in the mid-anterior regions when the 12mm blockage is present, as compared to the other cases. This suggests that the 12mm blockage significantly impairs perfusion in these areas.

However, the results from the other blockage sizes do not follow a simple progressive trend. Both the Bull's eye plots and the severity of defects on the 2D polar maps exhibit inconsistent patterns. For instance, in the no blockage and 1.5mm blockage cases, the Bull's eye values for the apical and mid-anterior regions show an increase in activity, contrary to the expected decrease. This is followed by a decrease in activity as the blockage size increases from 1.5mm to 5mm, which aligns with expectations, only for the activity to drop again from 5mm to 8.5mm.

It is important to note that the activity inside the phantom was not constant across all experiments. The first experiment with the 12mm blockage started with 0.35 mCi of Tc-99m, and 30 minutes later, the 8.5mm blockage was tested without adding any additional activity. After another 30 minutes, the experiment with the 5mm blockage was conducted, this time with added activity to restore the total to 0.35 mCi. Subsequently, the experiments with the 1.5mm blockage and the no blockage scenario were carried out in 35-minute intervals, without further adjustments to the activity levels.

This variation in activity levels during the acquisitions must be considered when interpreting the results, as it may have contributed to some of the inconsistencies observed in the perfusion patterns.



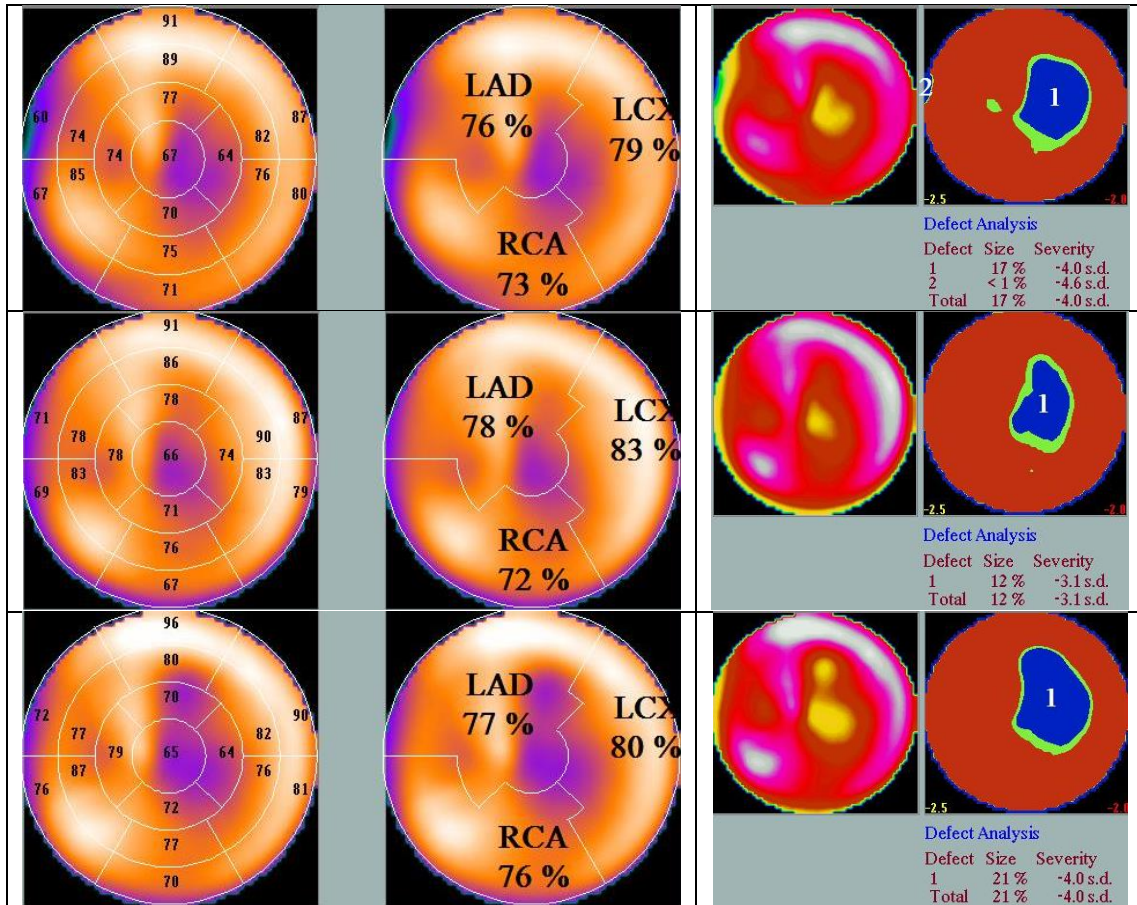


Figure 5.5: Mirage Processing – Bull's eye (left) and 2D polar (right) display for SMV DS7. (1st row: No blockage, 2nd row: 1.5mm blockage, 3rd row: 5mm blockage, 4th row: 8.5mm blockage, 5th row: 12mm blockage)

Imaging the Blockage Variations on MiE ECAM

For the MiE ECAM system, initial attempts were made to process the acquired images using the **Mirage Process** software, as was done with the SMV DS7 system. However, this led to significant image distortion. This issue is likely attributed to **Mirage Process** being an older program not optimized for dual-head SPECT systems, particularly those with detector heads positioned at a **90-degree angle**. This configuration appears to have confused the software, resulting in disfigured images for all **20 acquisitions** (under both real heart and phantom conditions).

To address this issue, processing was conducted using the **SCINTRON** software, the native platform for the MiE ECAM system. SCINTRON, designed specifically for dual-head acquisitions, provided accurate image reconstructions without distortion.

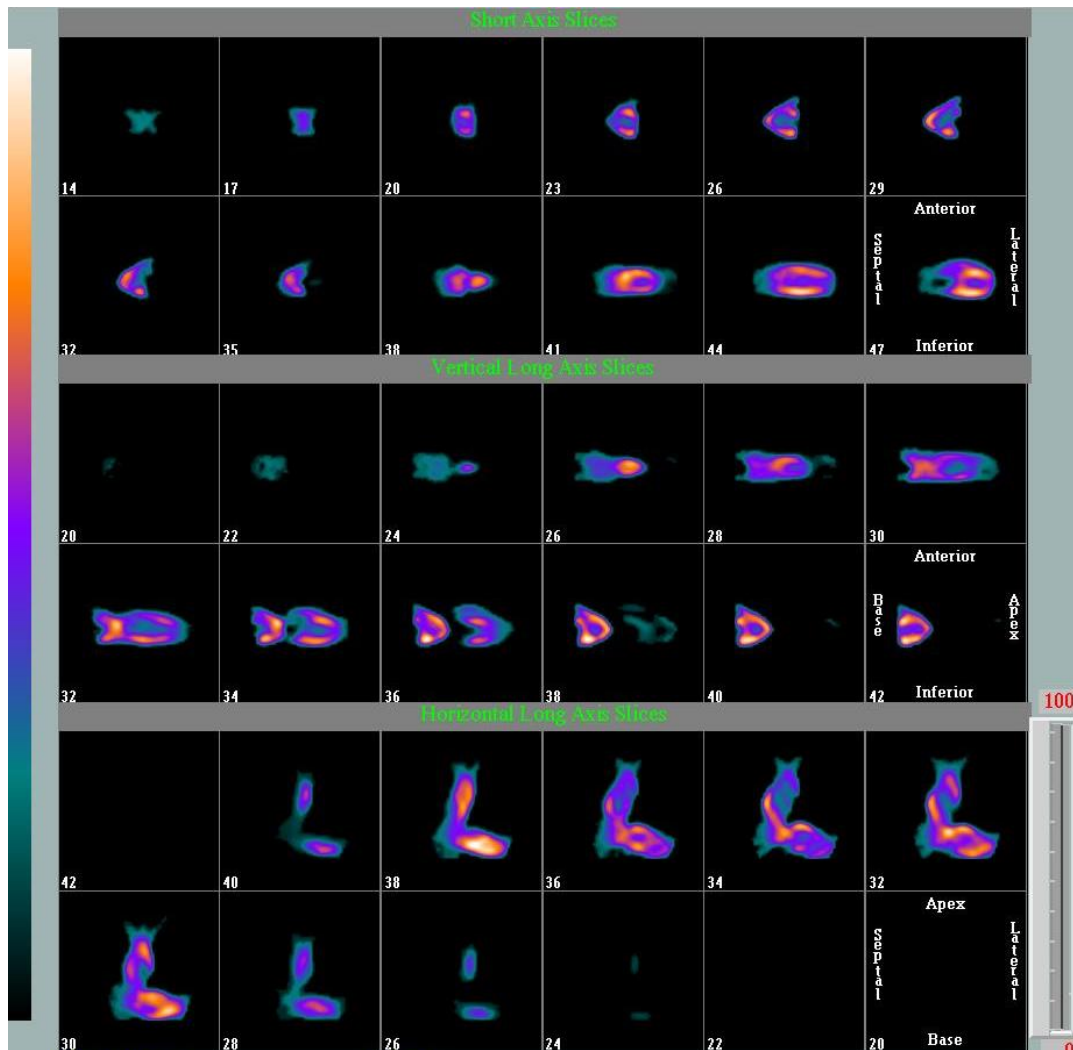


Figure 5.6: Mirage Processing – Disfigured 3 View Images acquired by MiE ECAM Dual Head System

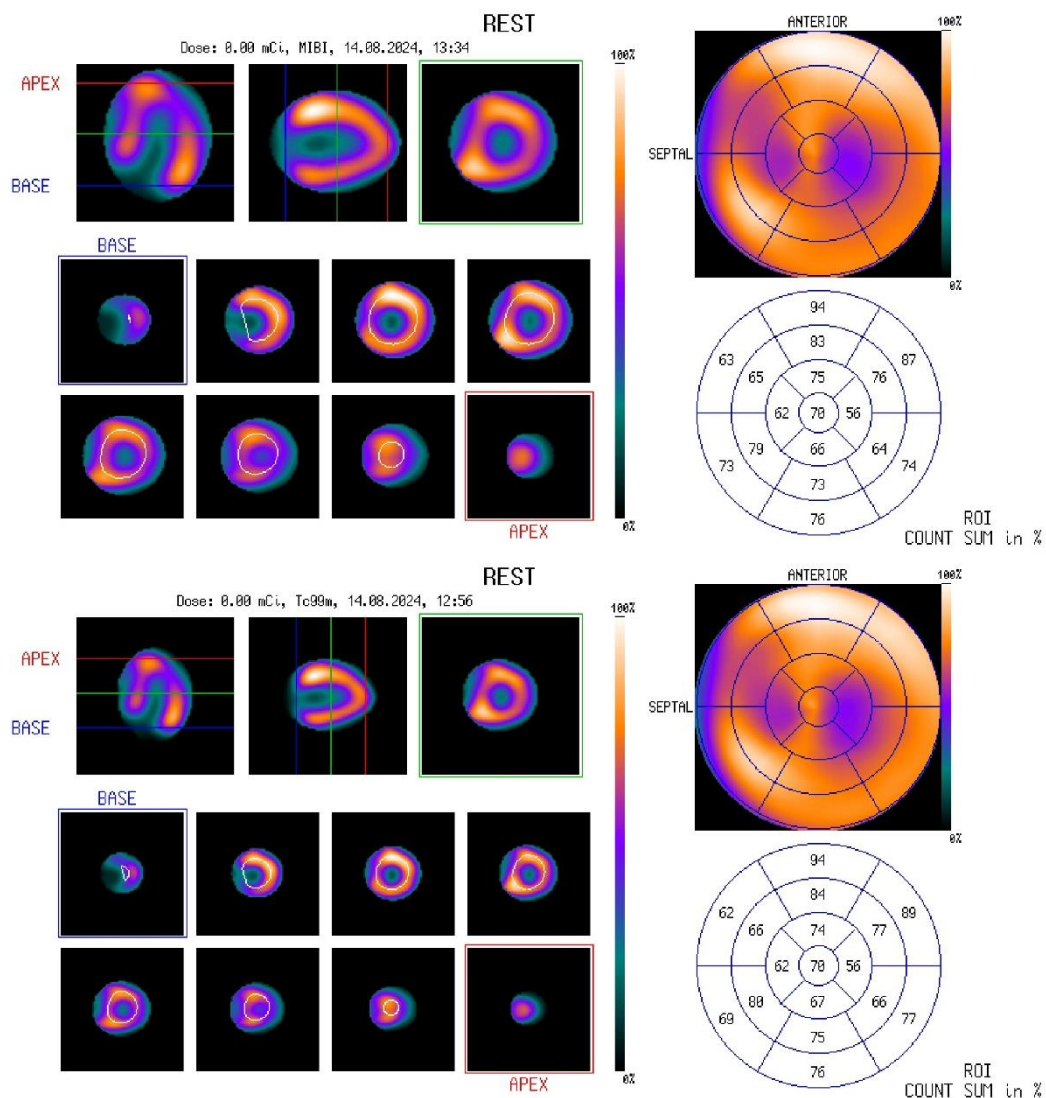
The five blockage cases acquired from the MiE ECAM system, processed with SCINTRON, are displayed in **Figure 5.7**. In the experiment conducted with the dual-head system, the shorter total acquisition time of 13 minutes (due to the use of two detector heads) eliminated the need to add more activity to the phantom between acquisitions, unlike the single-head system. Each acquisition was performed within 20-minute intervals, ensuring that the activity levels remained consistent throughout.

As observed in the previous experiment, the 12mm blockage resulted in a significant reduction, this time only in the mid-anterior region of the Bull's eye plot when compared to the other four cases. This indicates that the 12mm blockage consistently impairs perfusion in this area across different systems.

Additionally, a small but noticeable decrease in activity was observed for the 8.5mm blockage in the same mid-anterior region. Furthermore, a very small yet consistent decrease was observed in the neighboring mid-anterolateral region across all cases, except between the no-blockage and 1.5mm blockage scenarios. This slight decrease may be attributed to the presence of the blockages, suggesting that even smaller blockages could have a subtle impact on perfusion in adjacent regions.

However, unlike the single-head system, the dual-head system exhibited very minimal variation across the remaining blockage sizes (8.5mm, 5mm, 1.5mm, and no blockage), both in the mid-anterior region and throughout the other segments of the heart. This suggests a more stable and reliable performance of the dual-head system, as the inconsistent patterns observed with the single-head system are absent here.

While the lack of variability reduces the likelihood of obtaining inconsistent or misleading results, it also means that only the 12mm blockage produced a significant difference in the perfusion data. The other blockage sizes did not result in noticeable changes, indicating that the dual-head system is less sensitive to smaller blockages under these experimental conditions.



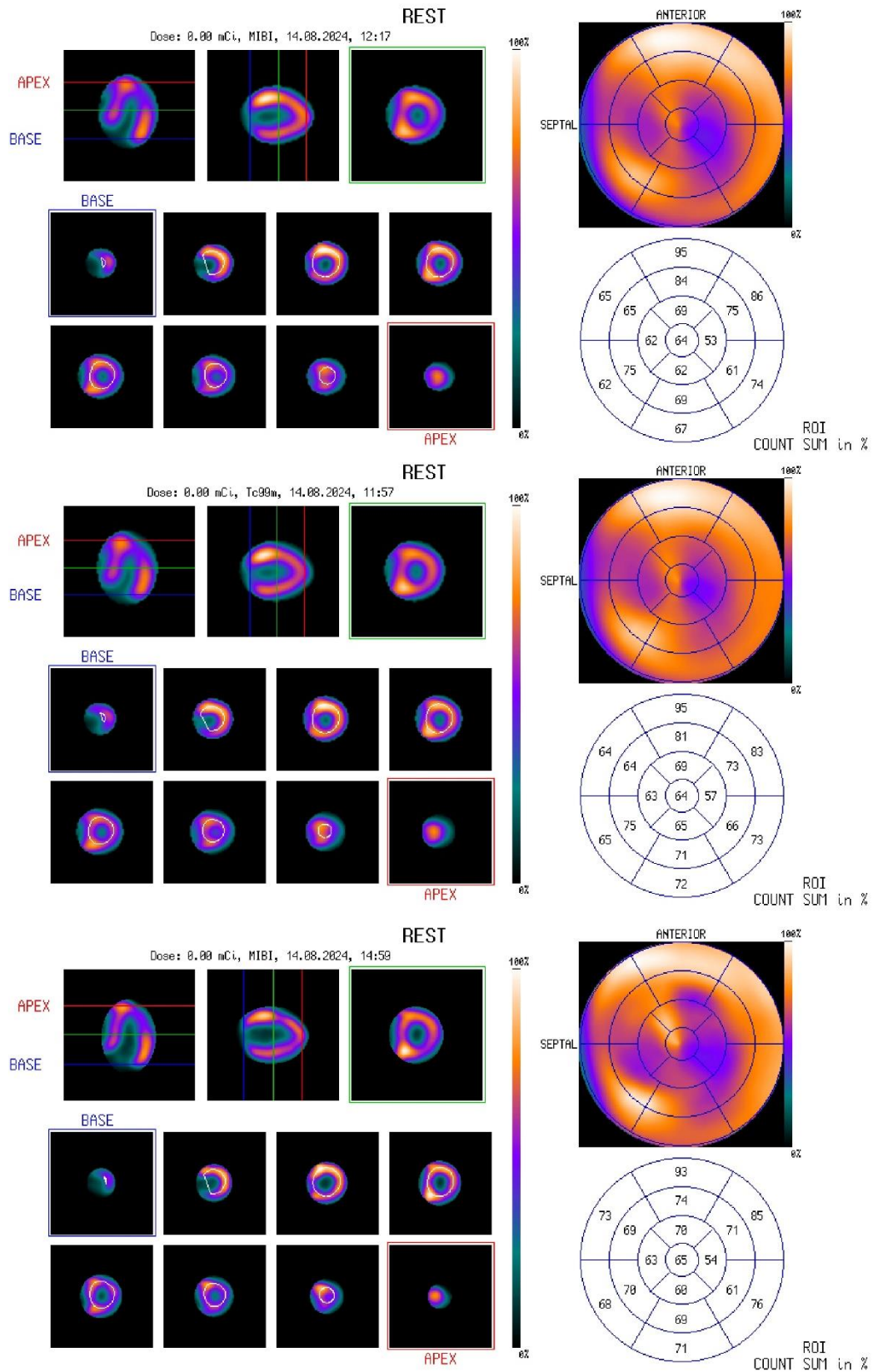


Figure 5.7: Scinttron Processing – 3 View (left) and Bull's eye (right) display for MiE ECAM. (1st row: No blockage, 2nd row: 1.5mm blockage, 3rd row: 5mm blockage, 4th row: 8.5mm blockage, 5th row: 12mm blockage)

5.3.1.2 Imaging the Real Heart Phantom with Acquisition Parameters: 128x128 Matrix, 64 Projections, 25 Seconds per Projection

In this experiment, a different set of acquisition parameters was selected to explore the imaging performance of the systems at higher resolution. Specifically, a **128x128 matrix** was used, with **64 projections** and an acquisition time of **25 seconds per projection**. To process the acquired data, the **iterative reconstruction method** was chosen, employing **9 iterations (the maximum number of iterations for the SCINTRON Processing)** as recommended by the European Association of Nuclear Medicine (EANM). The decision to use iterative reconstruction for this matrix size was based on its ability to handle larger datasets and provide higher image fidelity, especially for matrices like **128x128**, where the number of pixels is significantly increased. Iterative methods are better suited to minimizing image noise and reducing artifacts that may arise in complex reconstructions, such as those involving fine anatomical structures like the heart.

The iterative reconstruction method is particularly advantageous in scenarios where spatial resolution is paramount, as it allows for the detailed recovery of smaller image features, especially when dealing with higher matrix resolutions. Unlike traditional backprojection methods, iterative reconstruction iteratively refines the image estimate, leading to superior contrast resolution and better visual representation of the heart phantom's anatomical features.

As before, the imaging protocol was carried out using five different artificial blockages. The experiment began by imaging the heart phantom with the **12 mm** blockage, followed by the **8.5 mm**, **5 mm**, **1.5 mm**, and finally, no blockage at all. These acquisitions were performed sequentially, with particular attention to maintaining consistency across all experiments to ensure accurate comparisons could later be made.

Imaging of Blockage Variations on SMV DS7 with Mirage Processing

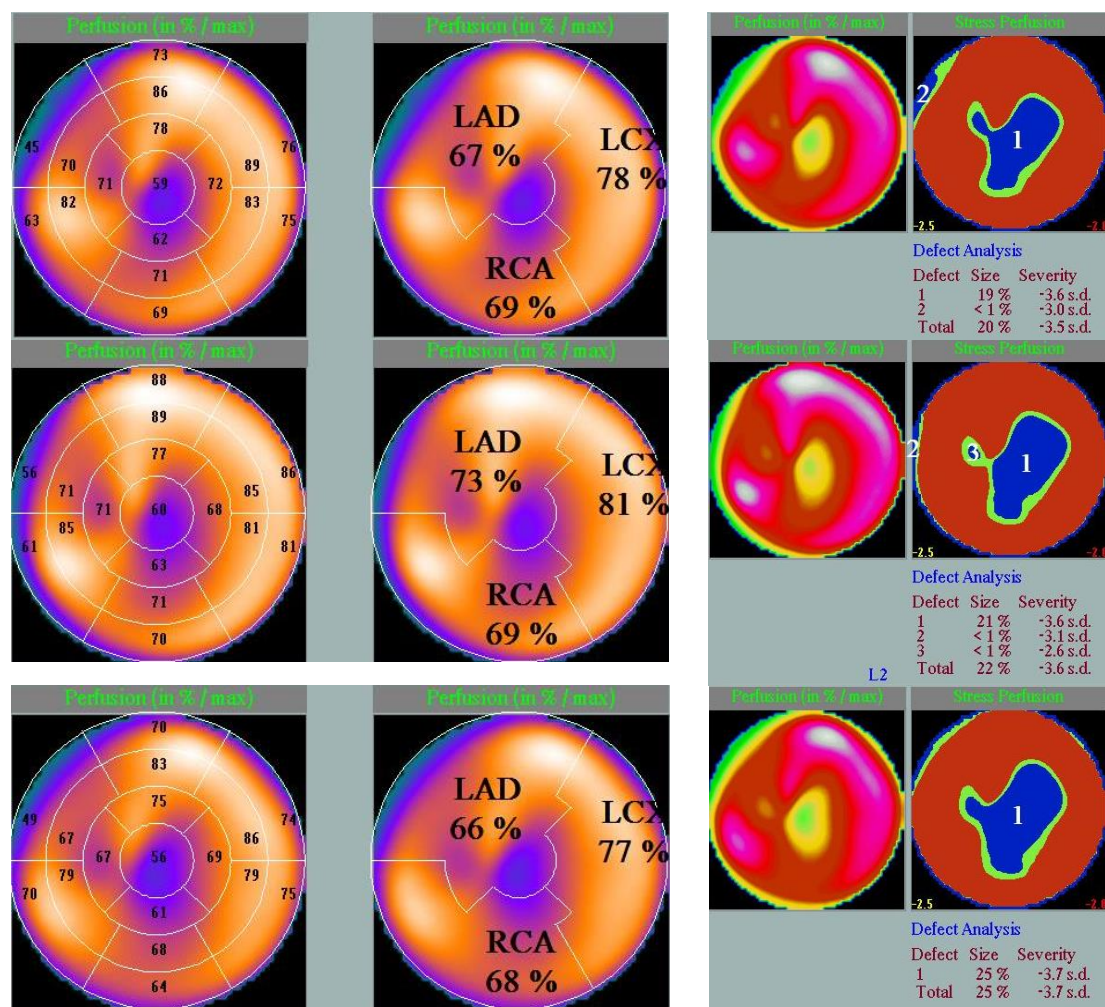
The first set of images was acquired using the **SMV DS7 single-head SPECT system**, with the same acquisition protocol of **128x128 matrix, 64 projections, and 25 seconds per projection**. For the processing of these images, the **Mirage Process** software was used, which, despite its age, was compatible with the single-detector system. The combination of the older hardware and the Mirage software produced images that, while limited by the system's inherent constraints, still provided a valuable reference point for comparison with the more advanced systems.

The Mirage Process software is designed for traditional analog systems like the **SMV DS7**, and it is optimized for single-head SPECT acquisitions, offering relatively basic but functional tools for image reconstruction and analysis. Despite its dated capabilities, Mirage Process allowed for the visualization of the five blockage scenarios, with each one progressively showing the reduction in blockage size and its effect on the image quality. The **12 mm** blockage showed the most pronounced reduction in perfusion, while the smaller **1.5 mm** and no blockage cases revealed more uniform distribution across the myocardium.

Images of the heart phantom were reconstructed using the iterative method, which, despite the older system, still offered a reasonable level of detail in the phantom's geometry. In this experiment, the total acquisition time was slightly over 26 minutes, with 35-minute intervals between each blockage acquisition. Before the acquisition of the 5mm blockage, additional activity was injected into the phantom, bringing the total Tc-99m activity to 0.35 mCi, similar to the procedure followed in the SMV DS7 experiment (5.3.1.1).

As illustrated in **Figure 5.8**, a clear reduction in activity is once again observed in the mid-anterior region of the Bull's eye plot for the 12mm blockage, consistent with previous results. However, as in the earlier experiments, the differences between the other four cases (8.5mm, 5mm, 1.5mm, and no blockage) remain minimal across the Bull's eye values.

Interestingly, the 2D polar maps display a small but progressively increasing severity in these four cases, with one exception: the 8.5mm blockage. This anomaly may suggest that the 8.5mm blockage was faulty, or it could be a result of the reinjected activity just before the acquisition of the subsequent 5mm blockage, which may have influenced the observed results.



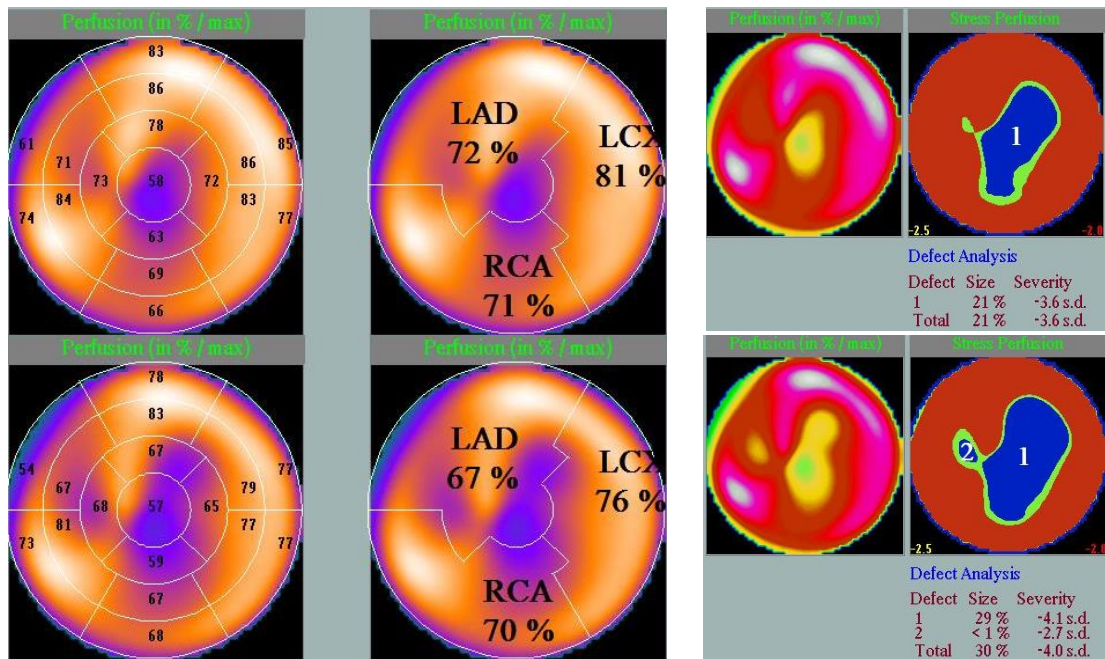


Figure 5.8: Mirage Processing - 3D perfusion (left) and 2D polar (right) display for SMV. (1st row: No blockage, 2nd row: 1.5mm blockage, 3rd row: 5mm blockage, 4th row: 8.5mm blockage, 5th row: 12mm blockage)

Imaging of Blockage Variations on MiE ECAM with SCINTRON Processing

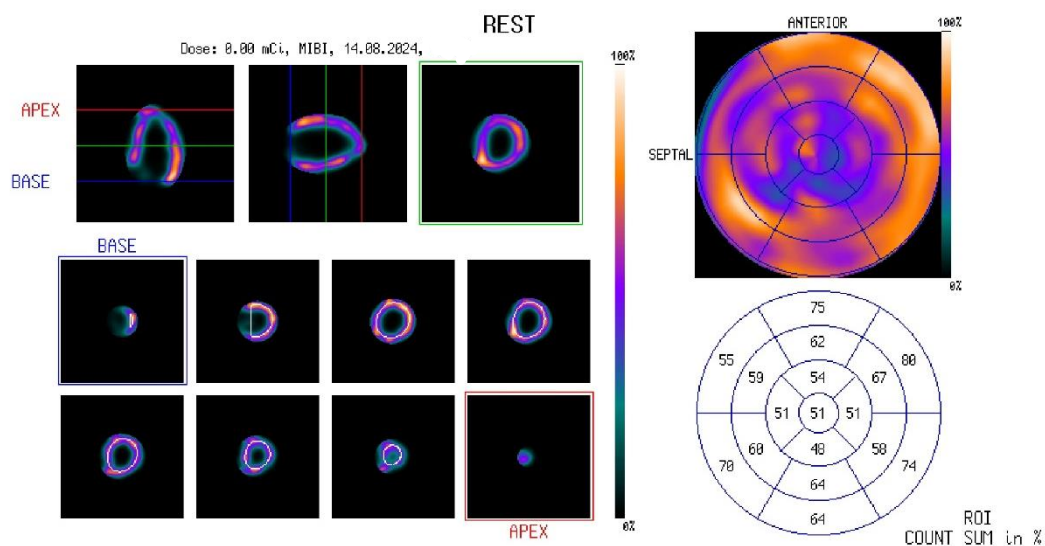
The next set of experiments was performed on the **MiE ECAM dual-head SPECT system**, using the same acquisition protocol of **128x128 matrix, 64 projections, and 25 seconds per projection**. Initially, attempts were made to process the data using **Mirage Process**, but it became clear that the software was incompatible with the dual-head acquisition format of the MiE ECAM. Mirage Process, being an older program, struggled to accurately reconstruct the data acquired from the two heads, especially given the **90-degree acquisition angle**. This caused significant distortions in all the images, rendering them unusable for analysis. The incompatibility was particularly evident in how the software handled the dual-head data input, which likely confused the reconstruction algorithms that were designed for single-head systems.

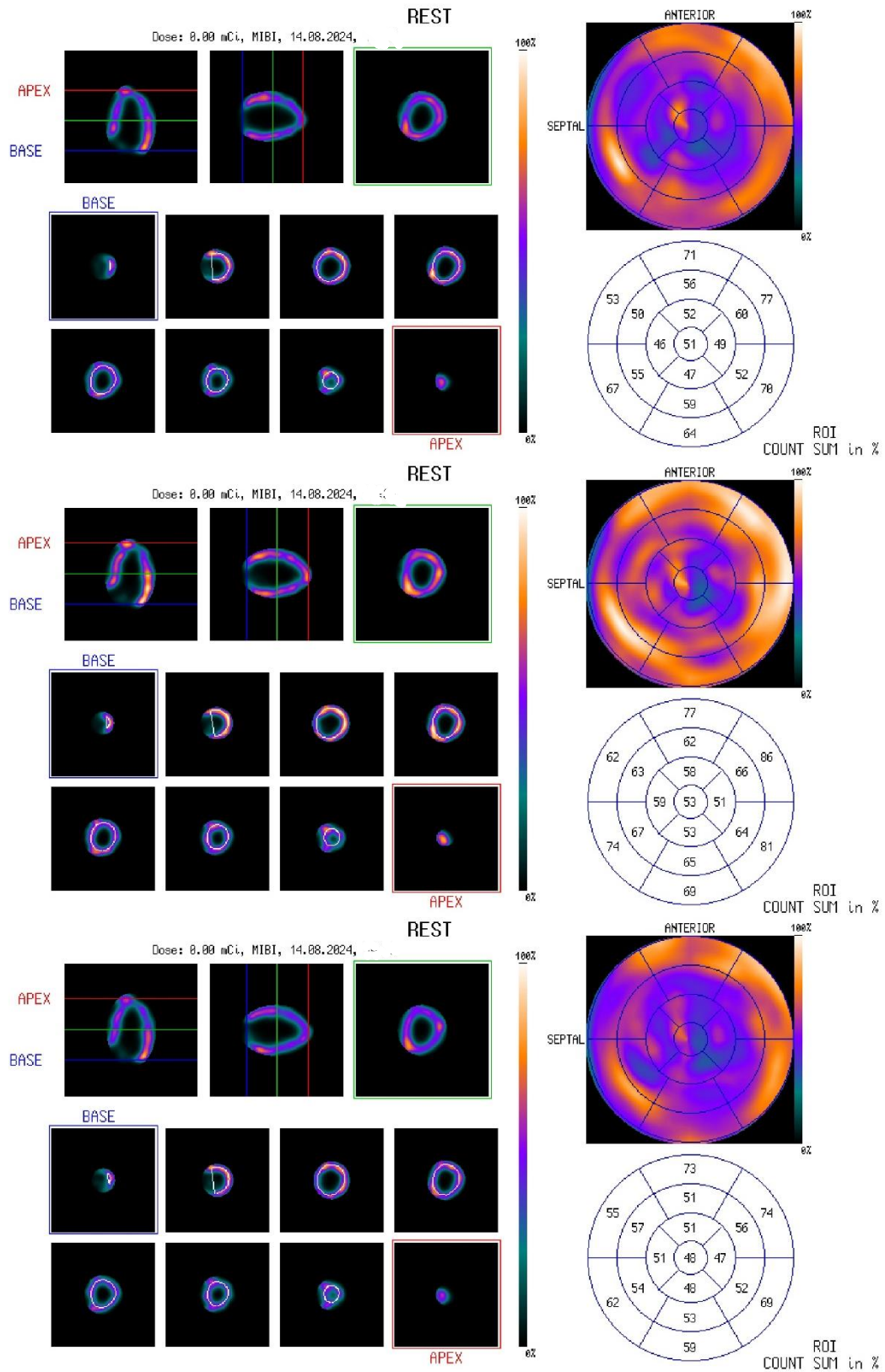
Due to these issues, the **SCINTRON software** was instead used for image processing. SCINTRON, being the native software for the MiE ECAM, was specifically designed to handle dual-head acquisitions, and thus provided a much clearer and artifact-free reconstruction of the data. SCINTRON's advanced image processing capabilities are more suited to modern systems like the MiE ECAM, as it offers improved handling of dual-head geometries and more sophisticated reconstruction algorithms, which are critical when working with larger matrices like **128x128**.

Once again, the five different blockage scenarios were imaged, starting with the **12 mm** blockage and working down to no blockage, maintaining the same acquisition and reconstruction parameters throughout. The resulting images, processed with **SCINTRON**, are displayed in **Figure 5.9**. In this iteration of the dual-head system experiment, the total acquisition time was 13 minutes, with 20-minute intervals between acquisitions. Due to the shorter intervals, no additional Tc-99m activity was injected during the process.

Notably, this is the first experiment where the 12mm blockage did not result in a substantial decrease in the mid-anterior region of the Bull's eye plot, contrasting with the significant reductions observed in previous experiments. Moreover, the Bull's eye images displayed not only artifacts in the apex, which were also present in earlier experiments, but also widespread artifacts throughout the apical and mid-ventricular regions.

When comparing these results with the previous experiment using the same dual-head system, where the only differences were the change in matrix size from 64x64 to 128x128 and the use of iterative reconstruction instead of filtered backprojection, the earlier results were more consistent and aligned with expected perfusion patterns. The current experiment's artifacts and lack of substantial findings in the 12mm blockage case suggest that the change in reconstruction method and resolution may have contributed to these unexpected outcomes, reducing the reliability of this particular dataset.





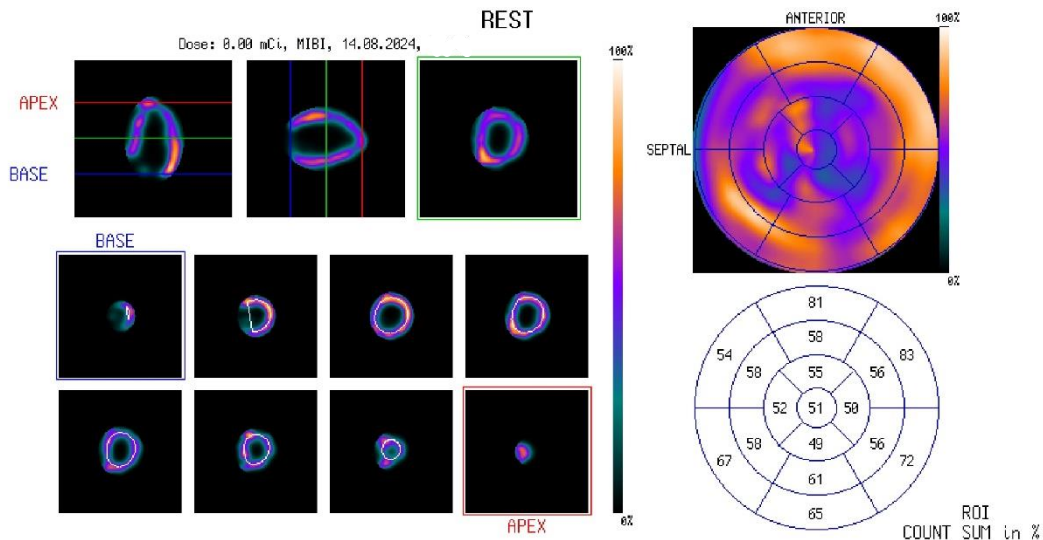


Figure 5.9: Scinticon Processing – 3 View (left) and Bull’s eye (right) display for MiE ECAM. (1st row: No blockage, 2nd row: 1.5mm blockage, 3rd row: 5mm blockage, 4th row: 8.5mm blockage, 5th row: 12mm blockage)

5.3.1.3 Imaging the Real Heart Phantom with Spectrum Dynamics D-SPECT CZT System and Cedars-Sinai QGS Processing

For this phase of the experiment, the heart phantom was imaged using the **Spectrum Dynamics D-SPECT Cardio CZT** system. Unlike the traditional SPECT systems described in the previous sections, the **D-SPECT** utilizes **CZT** technology, fundamentally altering the imaging process. This system features stationary detectors that do not rotate in a conventional manner, but instead move along the z-axis, scanning the patient in a unique way. This design eliminates the need for the rotating detector heads typically used in older systems, resulting in a faster and more efficient imaging process.

Due to this significant difference in technology, it was not possible to select the usual acquisition parameters, such as the **matrix size** or **number of projections**. Instead, the system automatically optimized these parameters based on the total acquisition time. For this experiment, the total acquisition time was set to **120 seconds**, replicating a typical rest study for a patient injected with the same amount of Tc-99m activity as in the other systems used in this study. The short acquisition time was made possible by the system's highly sensitive CZT detectors, which provide superior image quality with a significantly reduced scan duration.

The images obtained from the **D-SPECT CZT** system were processed using **Cedars-Sinai Medical Center's Quantitative Gated SPECT (QGS)** software, a highly regarded tool for analyzing cardiac SPECT images. **QGS** was employed for its ability to offer detailed quantification of heart volumes and perfusion, essential for evaluating the performance of the heart phantom under various blockage conditions.

As can be seen in the acquired **Figure 5.10** of the phantom below the image quality is pristine.

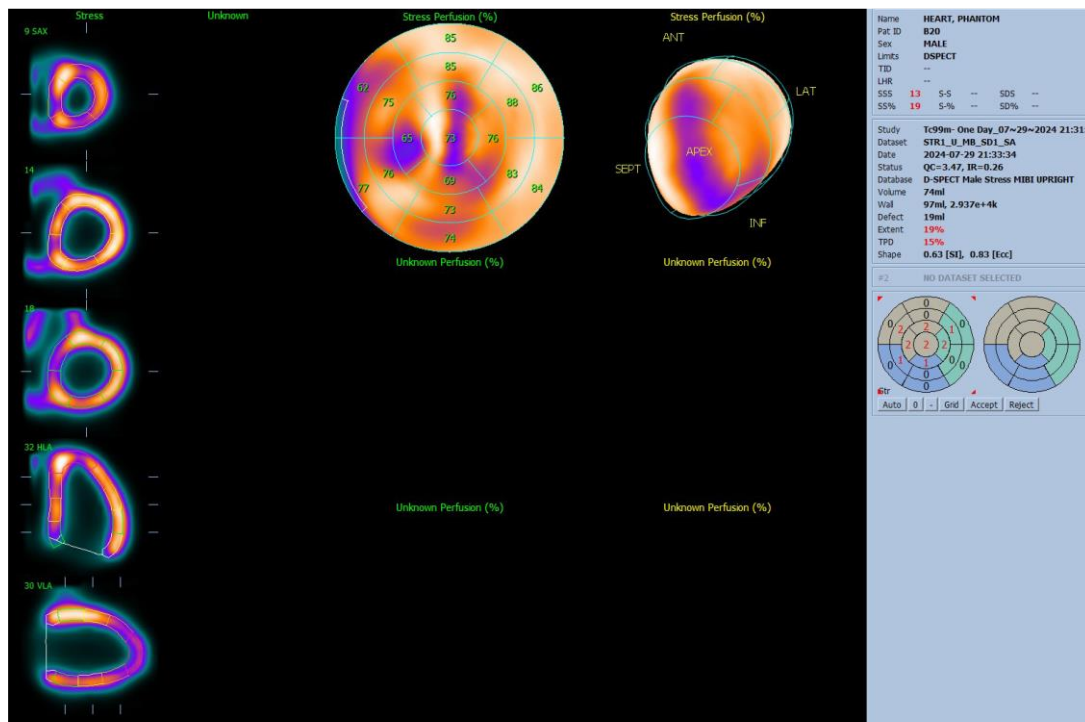
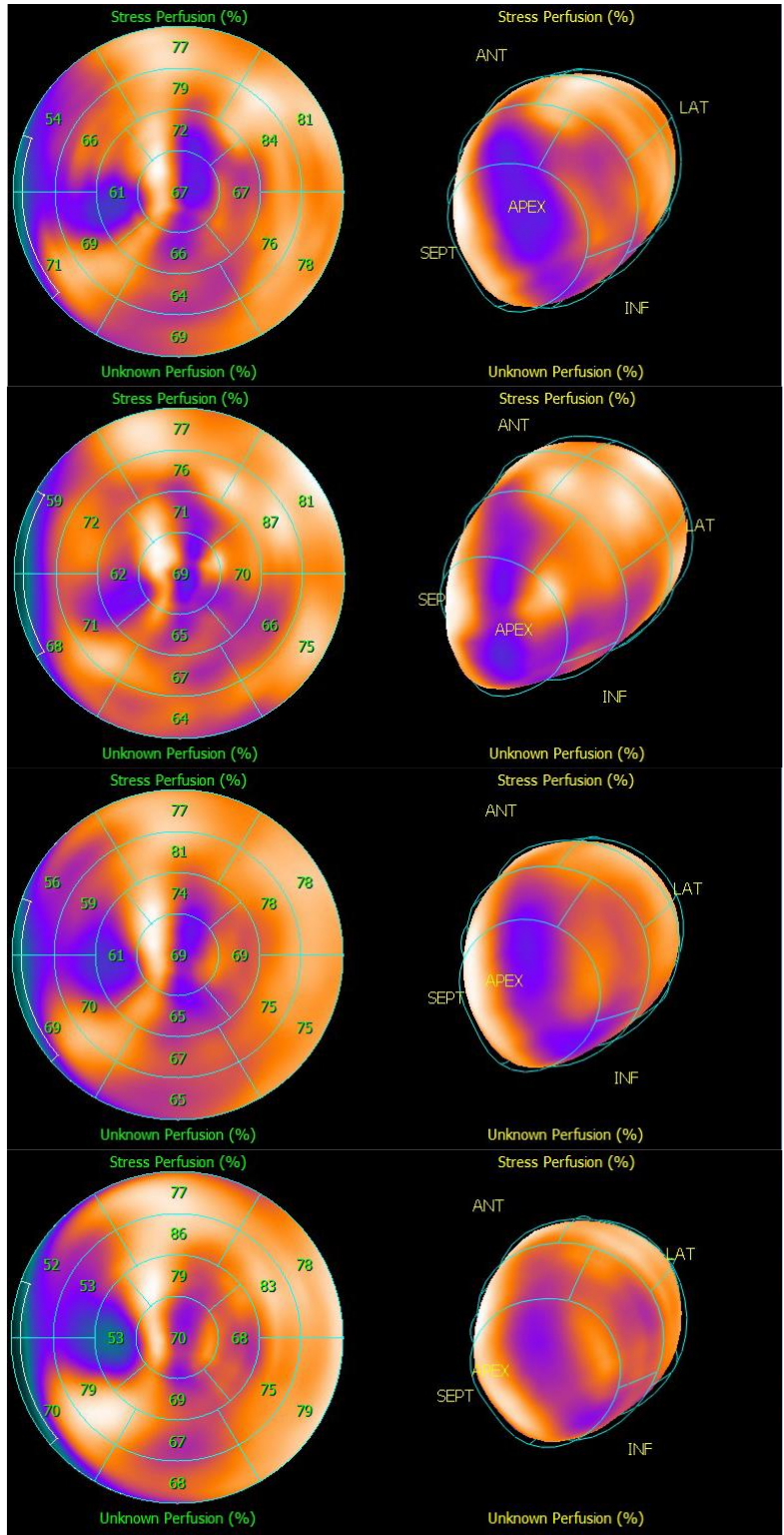


Figure 5.10: QGS Processing – 5 Cardiac view and Bull’s eye display of the cardiac phantom filled with 0.3 mCi Tc-99m and no blockage for D-SPECT Cardio.

As with previous sections, the five artificial blockage scenarios were applied: **no blockage**, followed by blockages of **1.5 mm**, **5 mm**, **8.5 mm**, and **12 mm**. The D-SPECT CZT's innovative design, with its rotating columns along the z-axis and advanced image reconstruction capabilities, provided high-resolution images even with the shorter acquisition time, allowing for precise visualization of each blockage.

The acquired images, shown in **Figure 5.11**, exhibited some interesting patterns. Just like in the previous experiments using different systems, the Bull's eye values in the cardiac apex were lower than expected, even in the no-blockage scenario. This observation was consistent across all blockages. Additionally, a decrease in values was seen in the general septal area in all cases, irrespective of the blockage size.

However, unlike the previous systems, there was no observed decrease in the Bull's eye values in the anterior or anterior-lateral regions, even as the blockages increased in size. This absence of a detectable trend in these regions raises the possibility that the very short acquisition time of 120 seconds may have led to an underestimation of the necessary scan duration, potentially affecting the system's ability to accurately reflect the impact of the blockages in these areas.



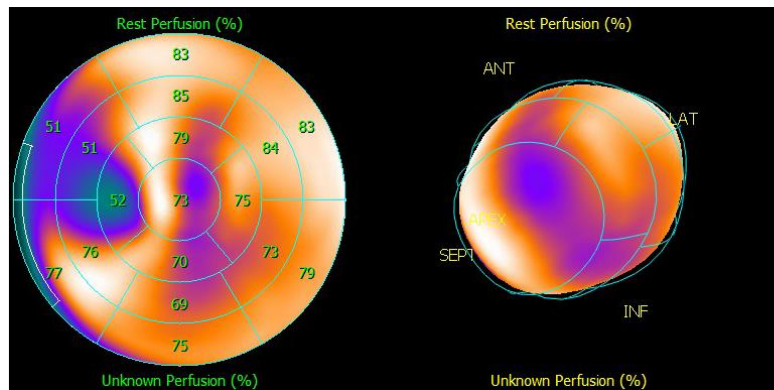


Figure 5.11: QGS Processing Bull's eye display of the cardiac phantom filled with 0.35 mCi Tc- for D-SPECT Cardio. (1st row: No blockage, 2nd row: 1.5mm blockage, 3rd row: 5mm blockage, 4th row: 8.5mm blockage, 5th row: 12mm blockage)

5.3.2 Variation 2: High-Activity Simulation

In the second variation of the experiment, the cardiac phantom was designed to simulate a heart with an activity level **15 times greater** than that of a typical clinical case. This was achieved by injecting **4.5 mCi** of Tc-99m at the start of the experiment. This higher activity level aimed to evaluate the systems' performance in scenarios where more counts are available, simulating conditions where higher doses are used for diagnostic purposes.

The acquisitions followed the same sequence of blockages as in the first variation:

1. **First Acquisition – 12 mm Blockage:** With an initial activity of 4.5 mCi, the first acquisition was performed with the 12 mm blockage inserted. The high activity allowed for faster acquisitions with shorter imaging times, which were particularly beneficial for older systems like the SMV DS7 and MiE ECAM, whose extended acquisition times could be significantly reduced under these conditions.
2. **Second Acquisition – 8.5 mm Blockage:** As with the first variation, the activity naturally decayed over time, but no additional Tc-99m was injected since the remaining activity was still sufficient for high-quality imaging. The 8.5 mm blockage was inserted, and the acquisition was performed on all three systems.
3. **Subsequent Acquisitions – 5 mm, 1.5 mm Blockages, and No Blockage:** The same sequence of acquisitions was performed, with the 5 mm, 1.5 mm, and no blockage plug inserted sequentially. The progressively smaller blockages were imaged without the need for additional Tc-99m due to the high initial activity, providing a direct comparison to the lower-activity scenario in Variation 1.

5.3.2.1 Imaging the High-Activity Heart Phantom with Acquisition Parameters: 128x128 Matrix, 64 Projections, 15 Seconds per Projection

In this subchapter, the high-activity heart phantom, prepared with an initial activity of 4.5 mCi of Tc-99m, was imaged using a 128x128 matrix, 64 projections, and 15 seconds per projection. This acquisition protocol, which reduces the time per projection compared to the lower-activity variation, was specifically designed to take advantage of the higher count rates associated with the elevated activity levels.

Imaging with SMV DS7 System and Mirage Processing

The first set of acquisitions was performed on the **SMV DS7** system using the **Mirage Processing** software. Due to the higher activity, the 15 seconds per projection provided sufficient counts for quality imaging, even with the traditional single-head rotating detector system. As discussed in previous sections, the older technology of the SMV DS7 can be limited by lengthy acquisition times, but the increased counts from the 4.5 mCi of Tc-99m injected into the phantom allowed for faster acquisition while still maintaining image quality.

The heart phantom was imaged in the same sequence of blockages as in the first variation, starting with the **12 mm blockage** and progressing through the **8.5 mm**, **5 mm**, **1.5 mm**, and **no blockage** scenarios. The Mirage processing software was utilized, applying the same reconstruction protocols (iterative reconstruction) as in the lower-activity variation for consistency. In this experiment, the total acquisition time was just over 16 minutes, with 20-minute intervals between acquisitions. As shown in **Figure 5.12**, for the first time, a consistent decrease in the Bull's eye values was observed in the apical anterior region as the blockages increased in size. Additionally, for the 12mm blockage, there was a significant reduction in the apical lateral region, which had not been noted with the smaller blockages.

These results can be compared with those from experiment **5.3.1.2**, conducted on the same single-head system and using the same processing software. The key differences between the two experiments were the much higher radiotracer concentration in the current experiment—15 times greater than the previous one—and the reduction in time per projection from 25 to 15 seconds due to the larger number of counts acquired from the higher concentration.

Although lower values were still recorded in the apex region, this experiment marks the first time a clear reduction was observed in the apical anterior region. The substantial increase in radiotracer concentration appears to have improved resolution and contrast, allowing for better detection of changes in regions that previously showed minimal variation.

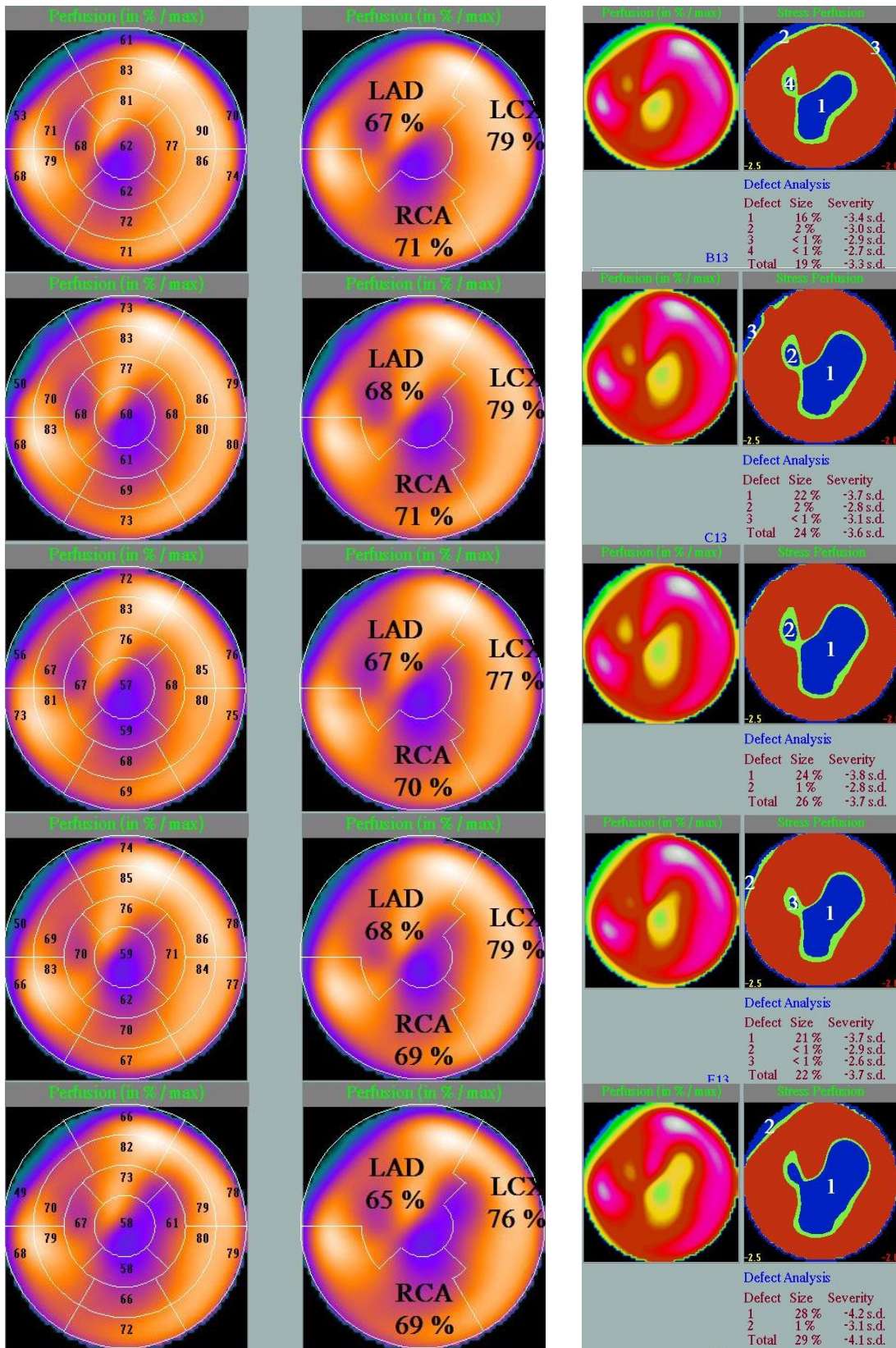


Figure 5.12: Mirage Processing - 3D perfusion (left) and 2D polar (right) display for SMV. (1st row: No blockage, 2nd row: 1.5mm blockage, 3rd row: 5mm blockage, 4th row: 8.5mm blockage, 5th row: 12mm blockage)

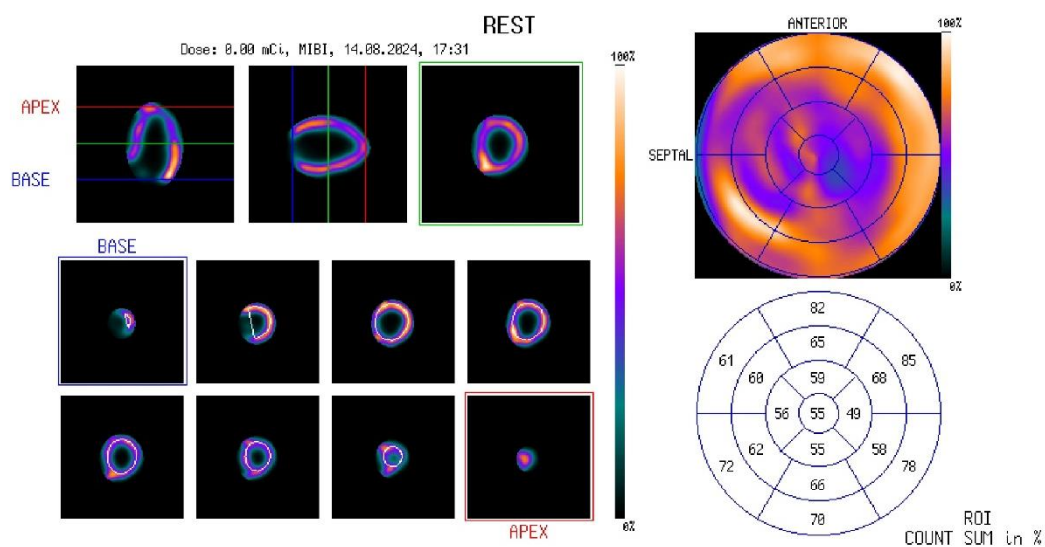
Imaging with MiE ECAM System and Scintron Processing

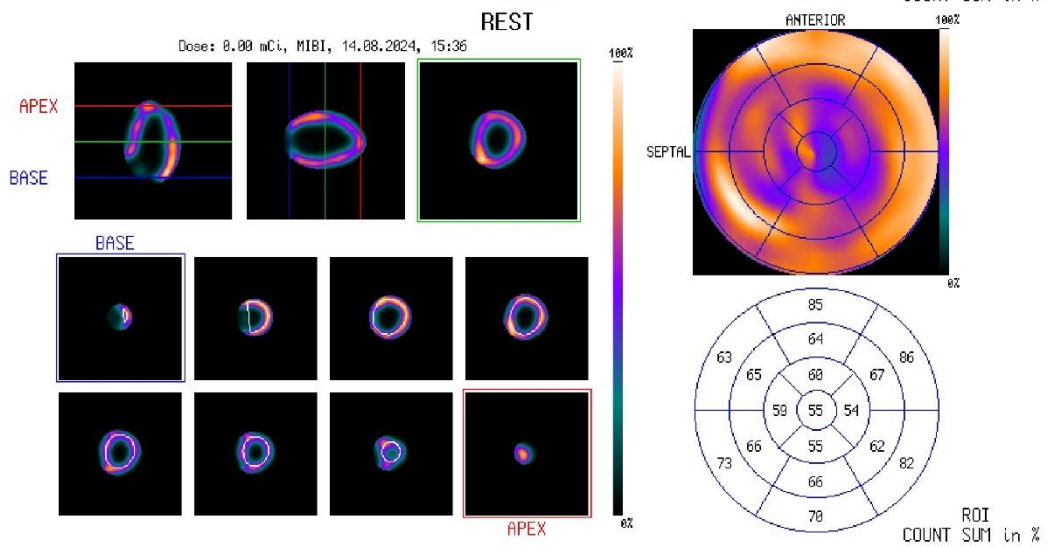
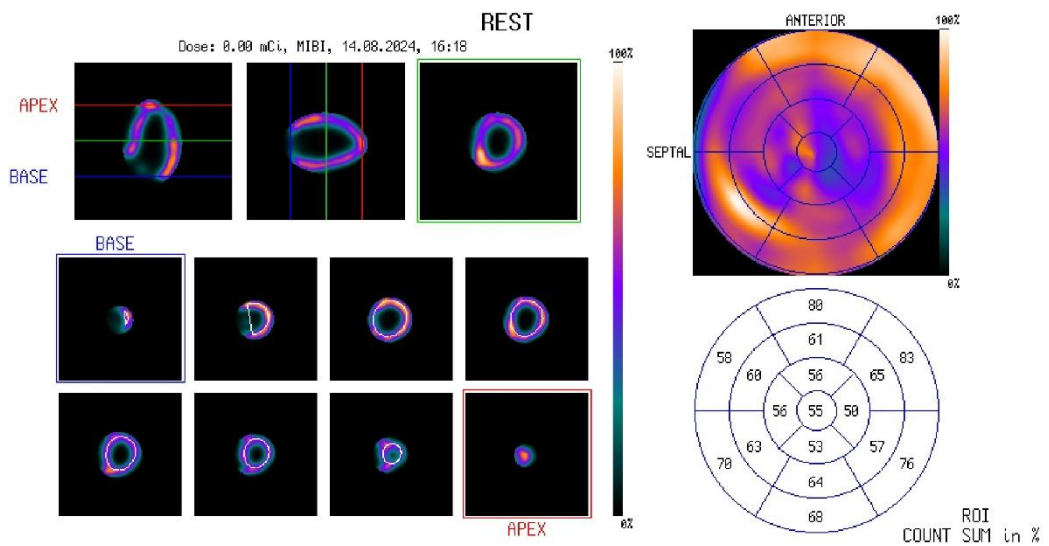
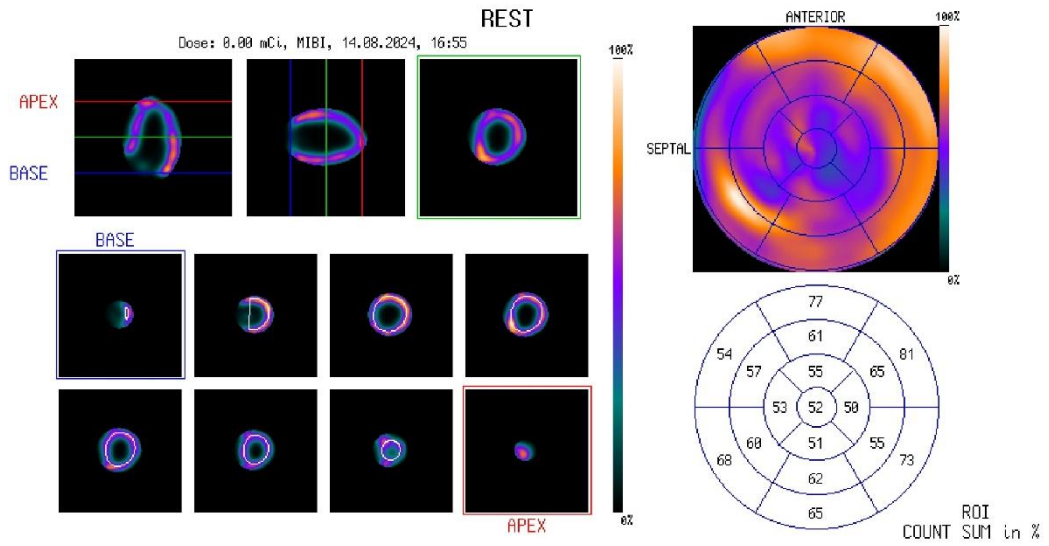
The same acquisition protocol (128x128 matrix, 64 projections, and 15 seconds per projection) was applied to the **MiE ECAM** system, this time utilizing the **Scintron** processing software. Similar to the **SMV DS7**, the higher activity allowed for a reduction in acquisition time while maintaining image quality. The **dual-head system** of the **MiE ECAM** performed well under these conditions, capturing the necessary counts quickly enough to generate high-resolution images.

As with the **SMV DS7**, the phantom was imaged with the **12 mm, 8.5 mm, 5 mm, 1.5 mm, and no blockage** plugs in sequence. The **Scintron** software was used for reconstruction, applying iterative methods to produce the final images. In this experiment, the acquisition time was again 8 minutes, with 12-minute intervals between acquisitions, and no additional Tc-99m was reinjected. Similar to the previous experiment described in **5.3.1.2**, the differences in this case were the increased radiotracer concentration and a reduced time per projection, just like in the single-head system experiment.

This time, a noticeable decrease in the Bull's eye value was observed in the mid-anterior region for the 12mm blockage. However, the decrease in values in the adjacent regions was minimal to nonexistent. As with the earlier experiment using the same system (**5.3.1.2**), the Bull's eye image displayed artifacts, not only in the apex but also throughout the apical and mid-ventricular regions.

These artifacts, which were similarly present in previous experiments on this system, continue to suggest limitations in image quality, particularly in these regions, despite the changes in radiotracer concentration and acquisition settings.





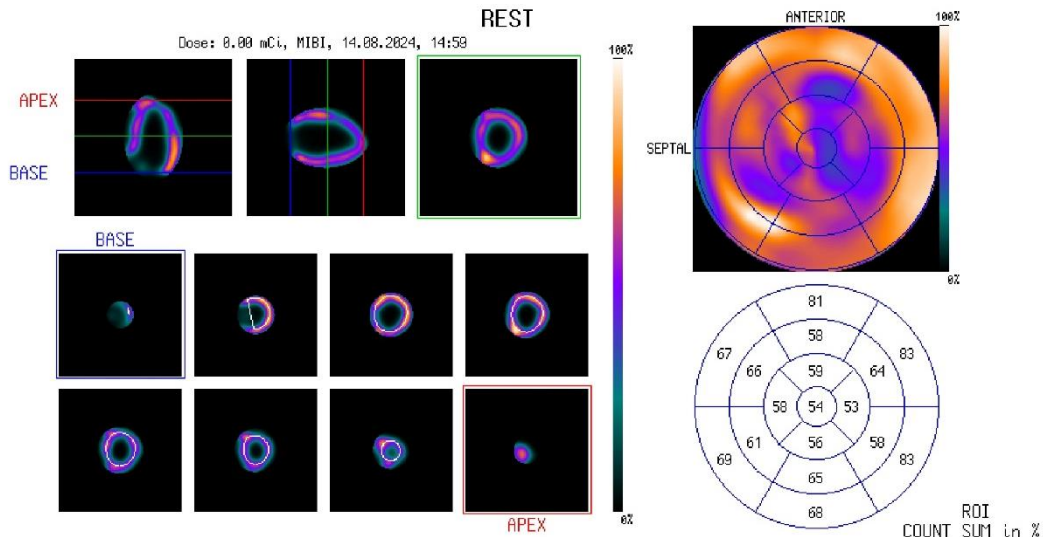


Figure 5.13: Scintatron Processing – 3 View (left) and Bull's eye (right) display for MiE ECAM. (1st row: No blockage, 2nd row: 1.5mm blockage, 3rd row: 5mm blockage, 4th row: 8.5mm blockage, 5th row: 12mm blockage)

5.3.2.2 Imaging the High-Activity Heart Phantom with Acquisition Parameters: 128x128 Matrix, 128 Projections, 15 Seconds per Projection

In this subchapter, the acquisition parameters were modified to **128 projections** while maintaining the same matrix size (128x128) and **15 seconds per projection**. The aim was to further improve image resolution by increasing the number of projections captured during the scan, particularly given the high activity of **4.5 mCi** in the phantom.

Imaging with SMV DS7 System and Mirage Processing

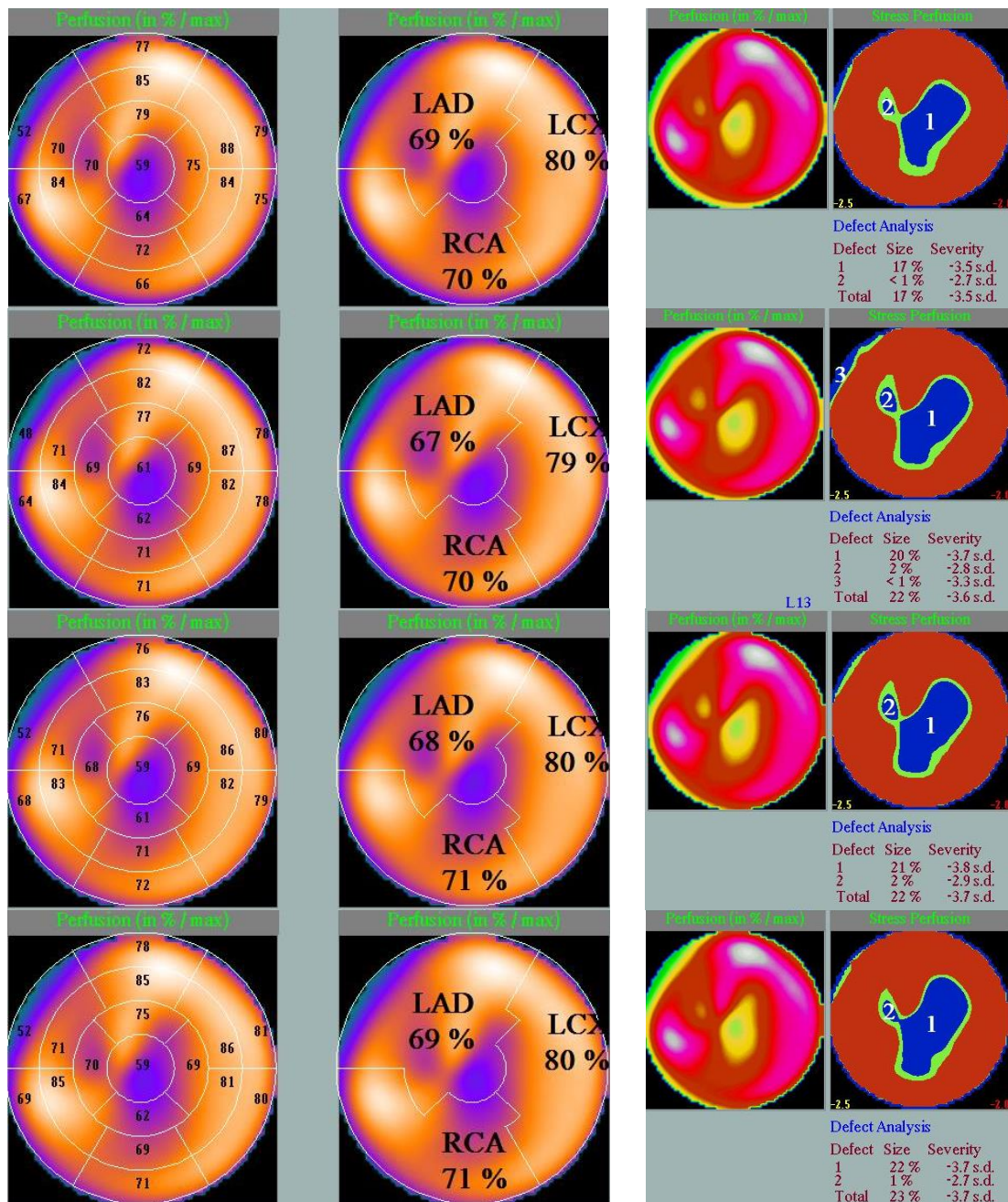
The **SMV DS7** system was once again used to perform the imaging, this time with the expanded projection set of **128 projections**. The increased number of projections, combined with the high count rates from the **4.5 mCi Tc-99m** activity, provided a clearer and more detailed image compared to the 64-projection protocol. The images were processed using the **Mirage** software with the same reconstruction settings.

Following the same sequence as before, the heart phantom was imaged with the **12 mm, 8.5 mm, 5 mm, 1.5 mm, and no blockage** configurations. The larger number of projections offered a more refined depiction of the blockage scenarios. In this experiment, the setup was similar to the one in **5.3.2.1** on the single-head system, with the key difference being the increase in the number of projections from 64 to 128. As a result, the total acquisition time extended to just over 32 minutes, with 35-minute intervals between each blockage acquisition.

Figure 5.14 illustrates a significant decrease in the Bull's eye value in the apical lateral region for the 12mm blockage, which had not been observed with the smaller

blockages. However, unlike in experiment 5.3.2.1, the decrease in the apical anterior value was inconsistent in this case, showing some variability compared to the steady reduction noted previously.

This inconsistency may be attributed to the extended acquisition time or the increased number of projections, affecting the sensitivity of the system in detecting subtle changes in this specific region.



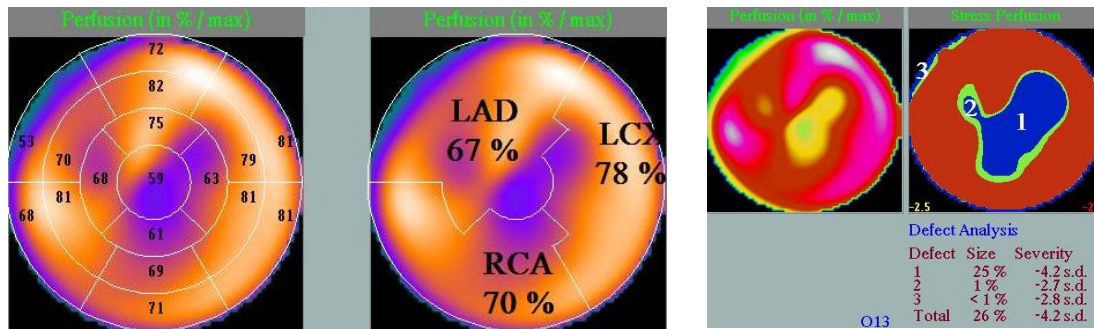


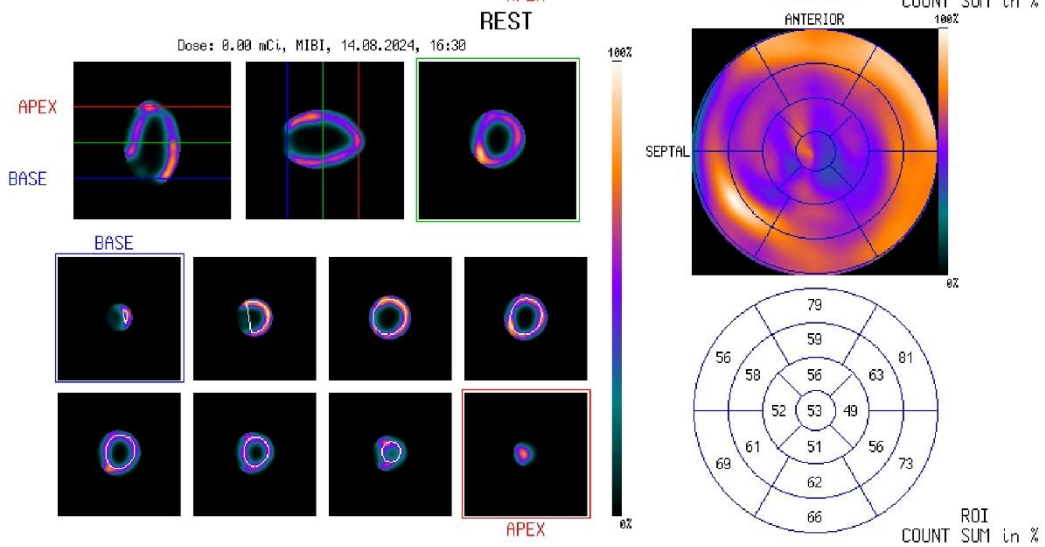
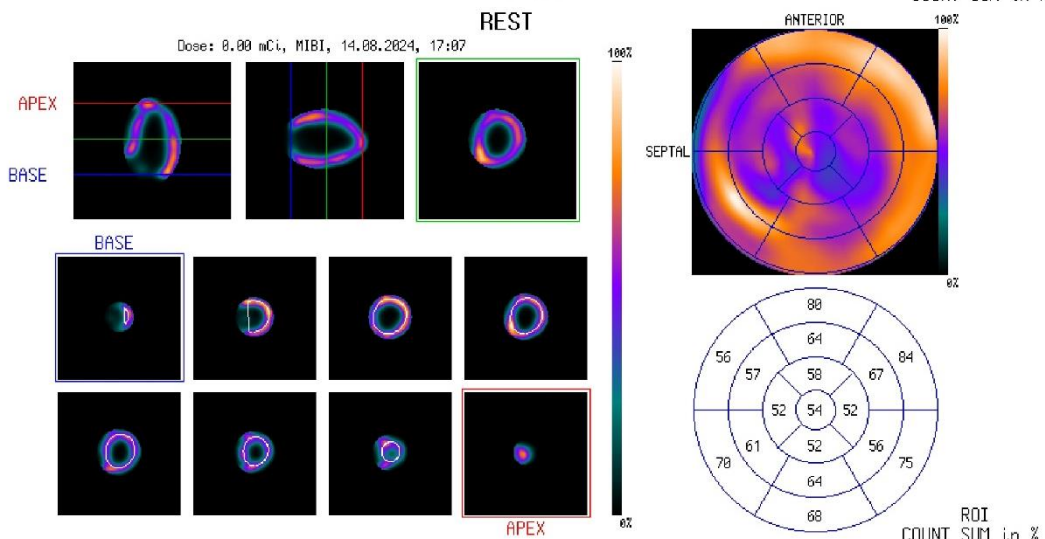
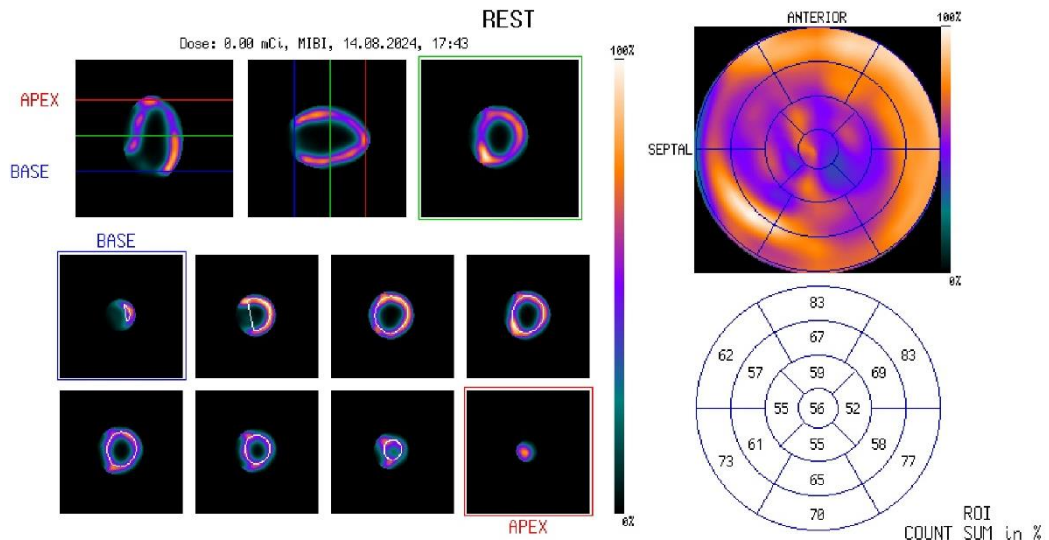
Figure 5.14: Mirage Processing - 3D perfusion (left) and 2D polar (right) display for SMV. (1st row: No blockage, 2nd row: 1.5mm blockage, 3rd row: 5mm blockage, 4th row: 8.5mm blockage, 5th row: 12mm blockage)

Imaging with MiE ECAM System and Scintron Processing

The **MiE ECAM** system also performed imaging with the **128 projections**, following the same protocol of **128x128 matrix** and **15 seconds per projection**. The **dual-head system** of the ECAM proved to be well-suited to the high activity conditions, particularly when combined with the increased number of projections, resulting in enhanced image resolution.

As before, the same sequence of **blockages** (12 mm, 8.5 mm, 5 mm, 1.5 mm, and no blockage) was applied to the phantom, with the images processed using the **Scintron** software. The acquisition time was 16 minutes, with 20-minute intervals between acquisitions, and no additional Tc-99m was reinjected. Compared to the experiment described in **5.3.2.1** on the same dual-head system, the primary difference here was the doubling of the number of projections, which also doubled the acquisition time.

Despite this change, the acquired images, as shown in **Figure 5.15**, reveal that the Bull's eye image displayed artifacts, not only in the apex but also across the entire apical and mid-ventricular regions. The level of artifacts observed is significant enough that it is difficult to determine whether the artificial blockages were responsible for the slight deviations in the Bull's eye values in certain areas. This suggests that the imaging artifacts may have masked the effects of the blockages, making the interpretation of the results less reliable.



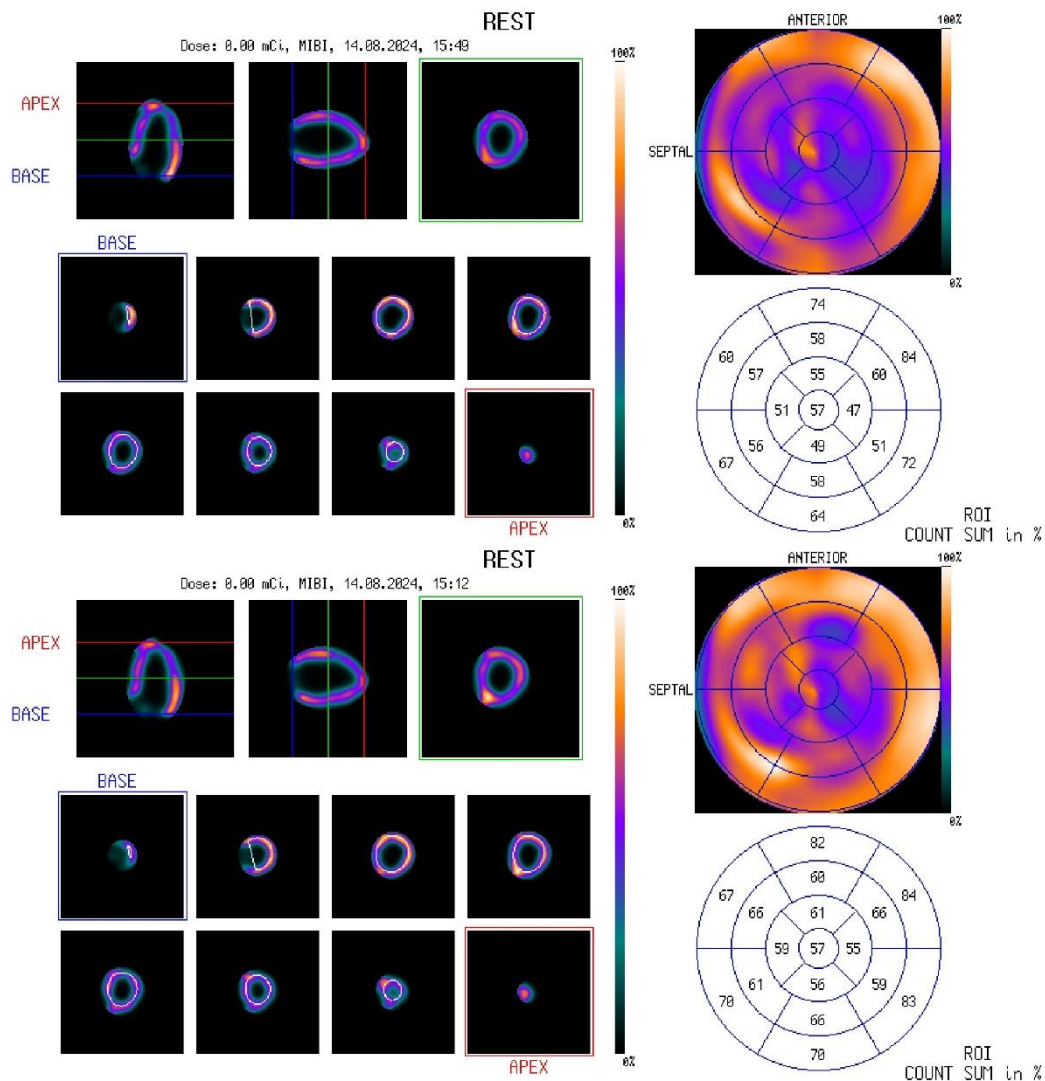
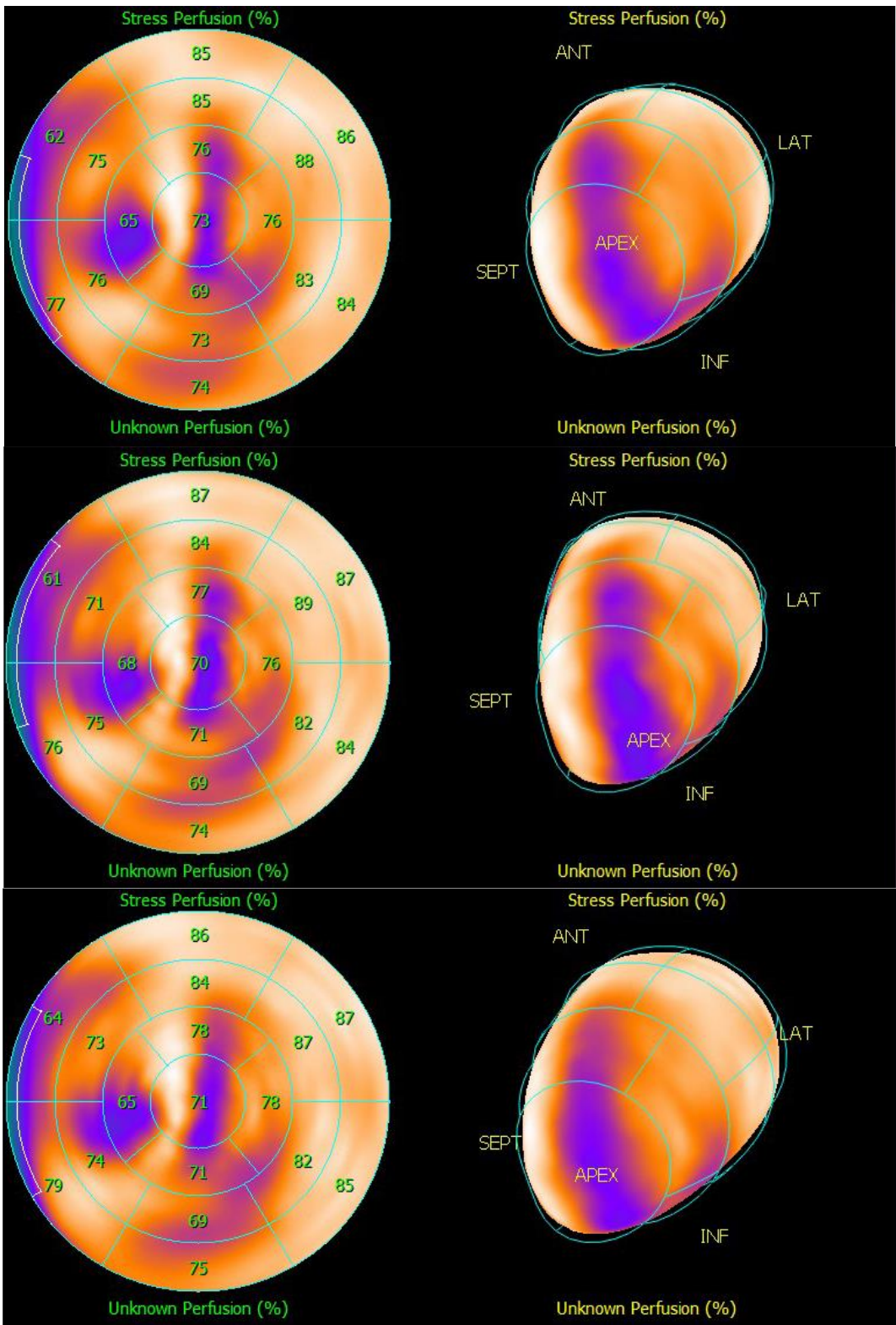


Figure 5.15: Scinttron Processing – 3 View (left) and Bull’s eye (right) display for MiE ECAM. (1st row: No blockage, 2nd row: 1.5mm blockage, 3rd row: 5mm blockage, 4th row: 8.5mm blockage, 5th row: 12mm blockage)

5.3.2.3 Imaging of the High-Activity Heart Phantom with Spectrum Dynamics D-SPECT CZT System and QGS Processing

The final set of acquisitions for this high-activity variation was conducted using the **Spectrum Dynamics D-SPECT Cardio CZT** system. For this experiment, the **4.5 mCi** of Tc-99m was utilized to simulate the high-activity conditions, and the acquisition time was set to **120 seconds**. Unlike the other systems, no matrix size or number of projections could be specified, as the system automatically optimizes the acquisition parameters based on the total scan time.

The images were processed using **Cedars-Sinai Medical Center's QGS software**, as in the lower-activity variation, with the same series of blockages applied in the following order: **12 mm, 8.5 mm, 5 mm, 1.5 mm, and no blockage** as shown in **Figure 5.16**



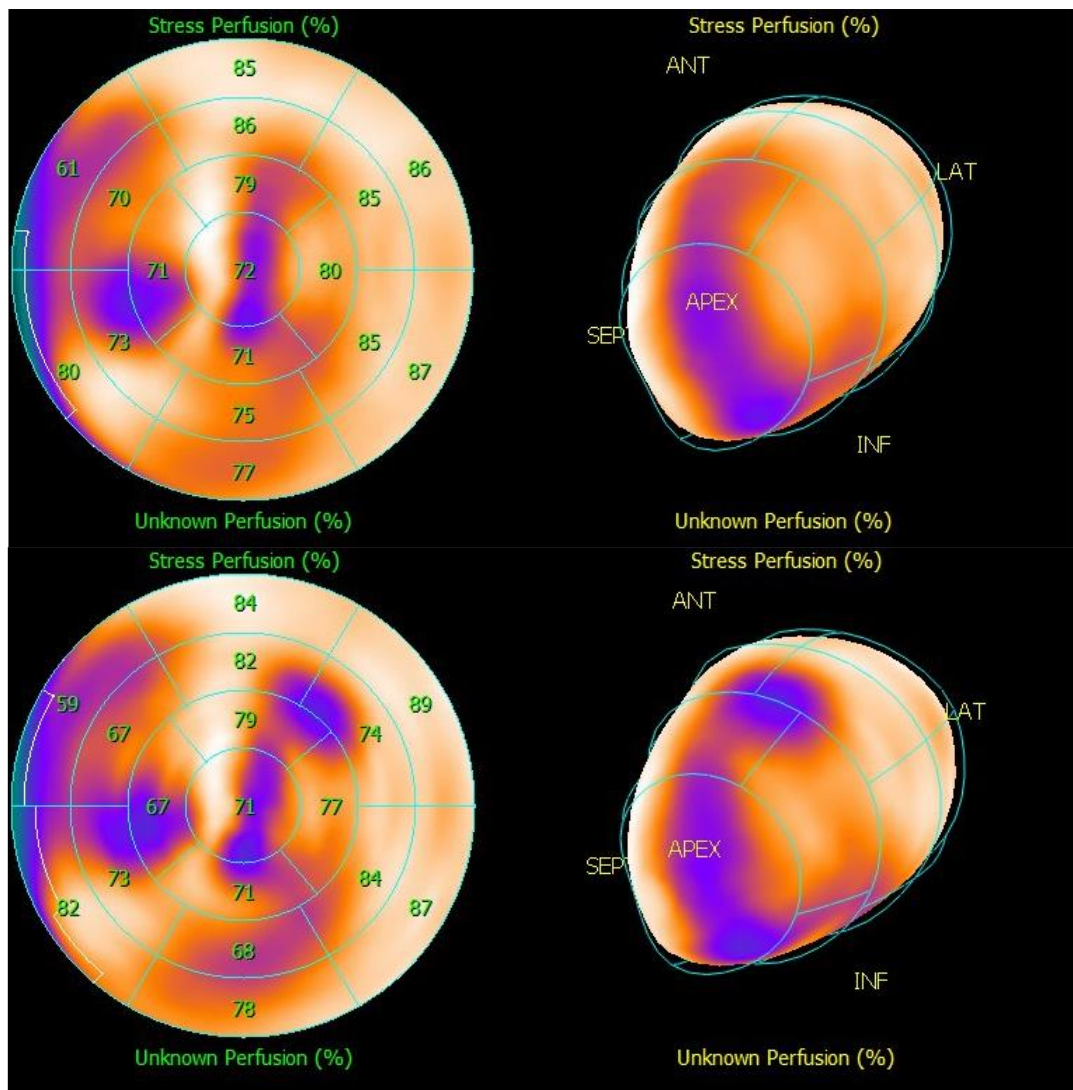


Figure 5.16: QGS Processing Bull's eye display of the cardiac phantom filled with 4.5 mCi Tc- for D-SPECT Cardio. (1st row: No blockage, 2nd row: 1.5mm blockage, 3rd row: 5mm blockage, 4th row: 8.5mm blockage, 5th row: 12mm blockage)

In this high-activity scenario, a significant difference was observed compared to the lower-activity acquisitions. Specifically, only with the 12 mm blockage did we detect a noticeable decrease in the Bull's eye values in the mid anterolateral region. This blockage also resulted in the formation of a distinct blue area between the apical anterior, mid anterolateral, and mid anterior regions, indicating a substantial reduction in perfusion or uptake in these regions.

In contrast, for the other blockages, the changes in values were minimal and did not lead to any similarly marked patterns. The high-activity conditions, combined with the short acquisition time, appeared to enhance the system's ability to differentiate the 12 mm blockage, though the absence of significant changes in the smaller blockages suggests that further optimization of acquisition parameters might still be necessary to fully leverage the system's capabilities under such conditions

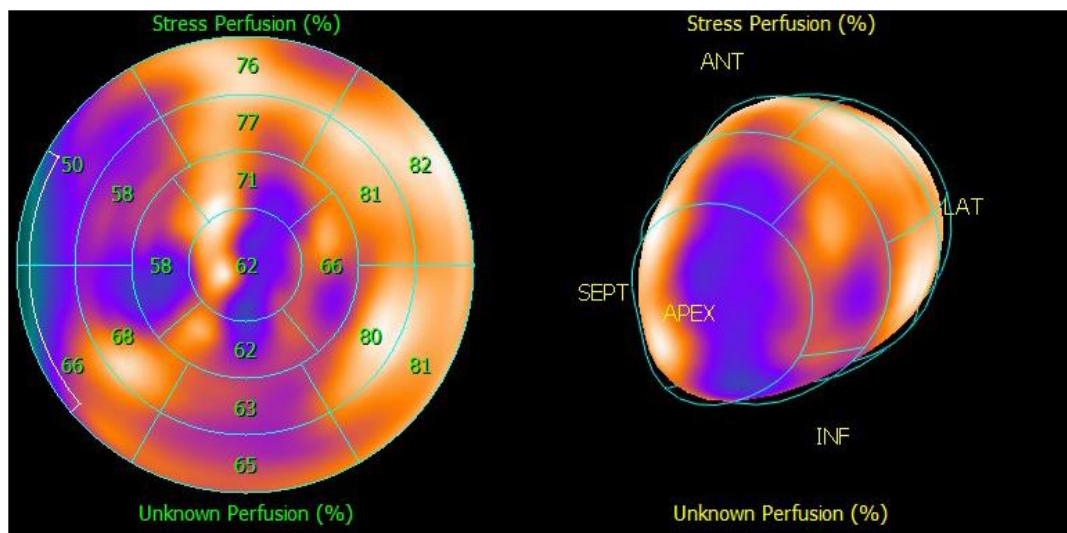
5.3.3 Variation 3: Low-Dose Protocol for the CZT System

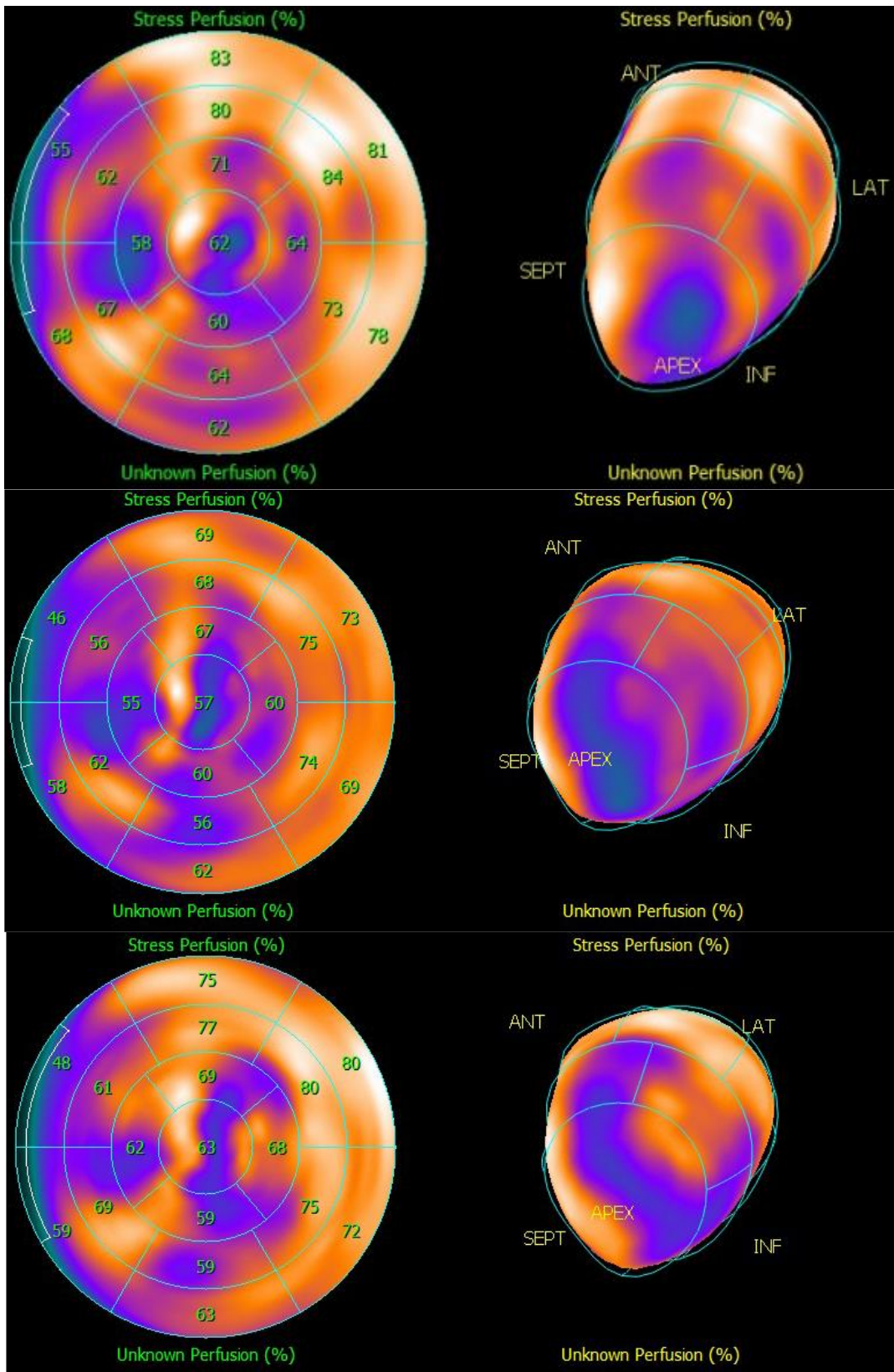
A third variation of the experiment was introduced specifically for the **Spectrum-Dynamics CARDIO 9 CZT system**, leveraging its advanced capability for **low-dose protocols**. In this variation, the initial Tc-99m activity was set to **0.1 mCi**, approximately **three times lower** than that used in Variation 1. The order of blockages was identical to the previous variations, starting with the **12 mm blockage** and proceeding through the **8.5 mm**, **5 mm**, **1.5 mm**, and finally the **no blockage** plug.

As in all previous experiments by this system and the **acquisition time** for each blockage was reduced to **2 minutes**. This shorter acquisition time minimized the decay of Tc-99m during the experiment, making it unnecessary to refill the phantom with additional activity after each acquisition. The combination of low activity and short acquisition times provided valuable insights into the performance of modern CZT technology in low-dose imaging scenarios, demonstrating its potential for reducing patient radiation exposure while maintaining diagnostic accuracy.

Figure 5.17, illustrating the results of this low-dose experiment, showed a striking similarity to those obtained under the high-activity protocol with 4.5 mCi. In both cases, the only definitive decrease in Bull's eye value was observed at the mid anterolateral area for the 12 mm blockage. This consistent finding across both low- and high-activity experiments highlights the sensitivity of the CZT system in detecting significant perfusion defects even with drastically reduced radiotracer amounts. However, as seen in the high-activity experiment, no substantial changes in values were observed for the smaller blockages.

This demonstrates that the CZT system's capacity for low-dose imaging did not compromise its ability to detect significant blockages, reinforcing the potential of the CARDIO 9 system to deliver reliable diagnostic information with minimal radiation exposure.





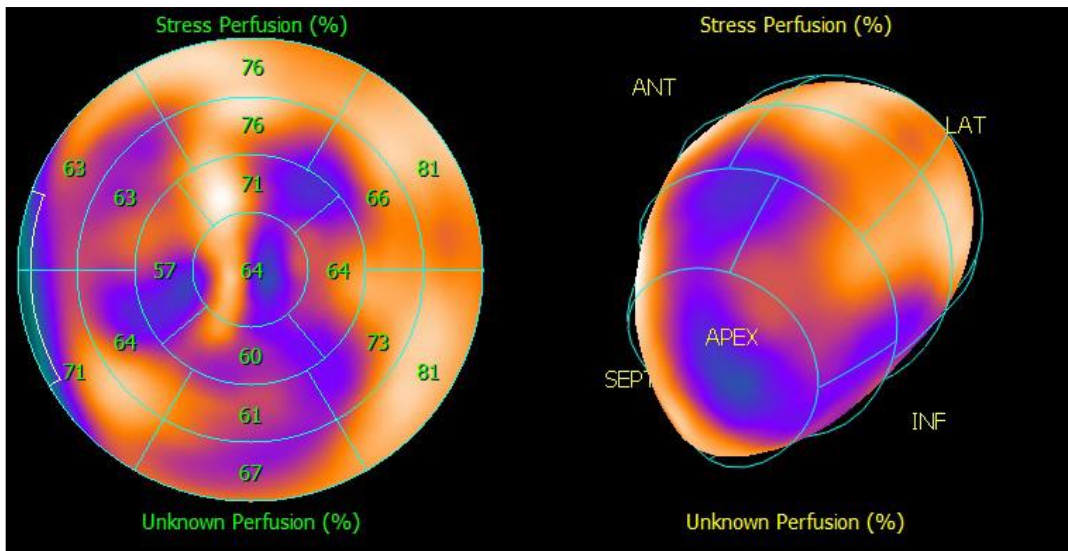


Figure 5.17: QGS Processing Bull's eye display of the cardiac phantom filled with 0.1 mCi Tc- for D-SPECT Cardio. (1st row: No blockage, 2nd row: 1.5mm blockage, 3rd row: 5mm blockage, 4th row: 8.5mm blockage, 5th row: 12mm blockage)

CHAPTER 6th

SUMMARY OF FINDINGS AND FUTURE PERSPECTIVES

6.1 Synopsis and Conclusions

The initial goal of this thesis was the creation of a realistic hollow heart phantom that can be filled with water and various pharmaceuticals for the simulation of nuclear cardiac examinations. This phantom was designed not as a hollow cylinder, like many commonly used phantoms, but as a structure that closely resembles a human heart in imaging. Given this success, it has been decided to pursue the creation of silicone phantoms in different dimensions.

In this chapter, we have conducted a detailed evaluation of the nuclear imaging results obtained from three SPECT systems: the SMV DS7 single-head system, the MiE ECAM dual-head system, and the Spectrum Dynamics CARDIO CZT system. These systems were used to assess the imaging quality of an anthropomorphic cardiac phantom under varying conditions, with simulated blockages of different sizes (12mm, 8.5mm, 5mm, and 1.5mm) and different radiotracer activities.

Key Observations:

1. **Bull's Eye Values and Apex Region:** Across all systems and experiments, a lower-than-expected Bull's eye value was consistently observed in the apex region. This anomaly was present even in scenarios with no artificial blockages. Furthermore, lower values were also detected in areas not directly adjacent to the blockage. This phenomenon could be linked to the limitations of the cardiac phantom's design. The initial .stl file used for the phantom was based on high-quality CT data. However, since the CT scan was not gated, the heart may not have been captured in the desired state typically seen during a cardiac scintigraphy. The static nature of the phantom's design could lead to artifacts, such as the reduced apex activity, which would not occur in a dynamic, real-world heart scan.
2. **Potential Blockage from Phantom Plug:** Another potential source of imaging anomalies is the design of the plug used in the phantom to simulate blockages. Even when no artificial blockage was intended, the plug's rubber edges may have touched the inner walls of the phantom, inadvertently simulating a slight blockage. This could explain some of the unexpected decreases in activity in regions distant from the intended blockage.
3. **CZT System Performance:** The three acquisitions with the Spectrum Dynamics CARDIO CZT system provided some unexpected results. In particular, the 12mm blockage was not visible in the acquisition with 0.35 mCi of activity. This could be attributed to the plug not being inserted correctly

during that specific experiment, as both higher and lower activity levels successfully detected the blockage. The variability in these results underscores the importance of consistent phantom handling and preparation to avoid experimental inconsistencies.

4. **Single-Head vs. Dual-Head System Performance:** Interestingly, in some experiments, the older SMV DS7 single-head system outperformed the more modern dual-head MiE ECAM system. One potential reason for this is the proximity of the detector to the phantom. With the SMV DS7 system, we were able to position the detector 5 cm closer to the phantom, as it does not have the light-rail safety features present in the ECAM system. These rails detect objects close to the detector and cause the system to retract, a feature that can interfere with optimal detector placement, especially when the ECAM system is configured with its two detectors at 90 degrees.
5. **Non calibrated Dose Calibrators.** Since the calibration of the dose calibrator devices is not performed regularly in the majority of clinics, the measured isotope activity may include significant errors and cannot be fully trusted.

Another contributing factor could be the rotation of the detectors. While the SMV DS7 performed a full 360-degree rotation around the phantom, the ECAM system rotated only 180 degrees, which may have impacted its ability to detect subtle changes in perfusion, particularly in smaller blockages.

Detailed Analysis of the Results:

1. **SMV DS7 (0.35 mCi, 64x64 matrix, 64 projections):** In the case of the 12mm blockage, a pronounced reduction in activity was observed in the apex and mid-anterior regions. However, inconsistent trends were seen across the other blockage sizes, with some cases (e.g., no blockage and 1.5mm blockage) showing unexpected increases in activity. This suggests that variability in radiotracer activity during the experiment could have influenced the results.
2. **MiE ECAM (0.35 mCi, 64x64 matrix, 64 projections):** For the 12mm blockage, a significant reduction in the mid-anterior region was noted, while the smaller blockages did not produce substantial changes in the Bull's eye plot. The dual-head system exhibited less variability than the single-head system, indicating more stable performance, though it was less sensitive to smaller blockages.
3. **SMV DS7 (4.5 mCi, 128x128 matrix, 64 projections):** Higher activity levels led to better detection of the 12mm blockage, particularly in the apical anterior region. The increased radiotracer concentration improved resolution, allowing for clearer identification of perfusion defects.
4. **MiE ECAM (4.5 mCi, 128x128 matrix, 64 projections):** Despite the increased activity, artifacts persisted in the apex and mid-ventricular regions, complicating the interpretation of the Bull's eye results. These artifacts may have masked the impact of the blockages, reducing the reliability of the results.

5. **Spectrum Dynamics CARDIO CZT (0.35 mCi):** The CZT system showed consistent underestimation of Bull's eye values in the apex across all blockages. A short acquisition time may have contributed to the absence of a detectable trend in certain regions, suggesting that longer scan durations might be necessary for better sensitivity.
6. **Spectrum Dynamics CARDIO CZT (4.5 mCi):** In high-activity scenarios, the 12mm blockage was clearly visible in the mid-anterolateral region, with significant reductions in perfusion. The system's ability to detect blockages with minimal radiation dose was further demonstrated in a subsequent low-dose protocol, reinforcing the CZT's potential for low-dose imaging.

Conclusions:

The results from this study reveal the complexities of phantom-based cardiac imaging and highlight several key factors that influence imaging outcomes:

1. **Phantom Design Limitations:** The static nature of the phantom, coupled with the non-gated acquisition of the initial CT data, likely contributed to some of the observed artifacts, particularly in the apex region.
2. **Experimental Setup and Equipment Sensitivity:** Differences in detector proximity, system configuration (single-head vs. dual-head), and acquisition parameters significantly affected the sensitivity of the systems to detect blockages. The older SMV DS7 system, despite its age, showed superior performance in some scenarios due to its ability to achieve closer detector positioning.
3. **System Performance:** The Spectrum Dynamics CZT system demonstrated potential for low-dose imaging with high sensitivity, particularly for larger blockages. However, optimization of acquisition times and parameters is necessary to fully leverage its capabilities for smaller blockages.

These findings underscore the importance of careful phantom design, consistent experimental protocols, and system optimization in nuclear cardiac imaging. The variations in performance between systems also highlight the need for tailored acquisition strategies to achieve optimal results in clinical settings.

6.2 Recommendations and Future Research Plans

Building on the findings and successes of this thesis, several recommendations and future research directions are proposed to further advance the development and application of the cardiac phantom.

The first recommended step is to reprint the cardiac phantom with one key modification: thickening the cardiac walls, particularly at the apex area, before utilizing Meshmixer's offset feature. This approach would ensure that the regions corresponding to the cardiac muscle are transformed into thicker void spaces, which could enhance the accuracy of perfusion simulation and mitigate some of the imaging artifacts observed in the current experiments. By

addressing the apex, where the low Bull's eye values were prevalent, this modification could yield more consistent and reliable results.

Another important suggestion relates to the 3D printing technique used in the creation of the phantom. For this experiment, the stereolithography (SLA) method was chosen due to the use of clear resin, which provided both watertightness and the ability to visually inspect the interior of the phantom during the experiments. However, for future printing endeavors, selective laser sintering (SLS) using nylon powder is highly recommended. The mechanical properties of nylon would allow for the reduction of phantom wall thickness, currently set at 5mm, resulting in better radiation penetration and more accurate imaging. Furthermore, the SLS process eliminates the need for internal support structures, simplifying the manufacturing process and avoiding potential issues related to their removal.

Additionally, the administered activity should be measured with a common and correctly calibrated dose calibrator for reliable results

Should the reprinted phantom demonstrate no problematic areas in the Bull's eye plots during the no blockage scenario, it would be valuable to repeat the experiments conducted in this thesis with Tc-99m and other isotopes like Tl-201. The comparison of results could confirm the reliability of the modifications and further expand the research scope to include other systems, such as SPECT/CT and PET/CT. These systems could provide complementary imaging data, enhancing the overall evaluation of the phantom's performance and enabling a broader understanding of nuclear cardiac imaging techniques. On a more ambitious level, a future version of the phantom could include not only a hollow representation of the heart but also the major cardiac arteries. These arteries would be designed to branch out like the roots of a tree, with each branch delivering activity solution to different areas of the heart, mimicking real blood flow. Such a model would introduce complex perfusion dynamics, where blockages in different arterial branches could result in distinct perfusion defects across various areas of the heart. These areas could be tiny chambers with thin boundary walls, challenging the imaging systems to detect differences in perfusion. If successful, this would create a highly realistic model for investigating specific coronary artery blockages.

A final step in advancing this research would be the creation of a phantom that mimics the periodic movement of the heart. This would involve a dynamic system capable of simulating the heart's beating motion, enabling the execution of gated experiments and simulations. Incorporating this feature would allow for the study of myocardial perfusion under realistic conditions, further aligning the phantom's behavior with that of a human heart during nuclear cardiac examinations.

By following these recommendations and expanding the research, the utility and realism of the anthropomorphic cardiac phantom could be greatly enhanced, making it a powerful tool for simulating and studying nuclear medicine cardiac imaging.

BIBLIOGRAPHY

1. Carlson S. A Glance At The History Of Nuclear Medicine. Acta Oncol. 1 January 1995;34(8):1095–102.
2. Radiation Protection Courses for Medical Ionizing Radiation Machine Operators, EEAΕ, Athens, June 2011.
3. Sathekge M, ChB M. Targeted radionuclide therapy.
4. Harkness-Brennan L. An Introduction to the Physics of Nuclear Medicine: Morgan & Claypool Publishers; 2018. Available: <https://iopscience.iop.org/book/mono/978-1-6432-7034-0>
5. Medical Imaging Techniques SPECT and PET.
6. Chantadisai M, Sirisalipoch S, Vachatimanont S. Utility of gated SPECT parameters in detection of coronary artery disease in patients with normal perfusion images. Egypt J Radiol Nucl Med. 15 December 2022;53(1):257.
7. Iniewski K. CZT detector technology for medical imaging. J Instrum. 4 November 2014;9(11):C11001–C11001.
8. Strauss HW, Mariani G, Volterrani D, Larson SM. Nuclear Oncology: From Pathophysiology to Clinical Applications. Cham: Springer International Publishing : Imprint : Springer; 2020.
9. Willson T. Principles of SPECT. Στο: Van Den Wyngaert T, Gnanasegaran G, Strobel K. Clinical Atlas of Bone SPECT/CT. Cham: Springer International Publishing; 2022 [παρατίθεται 26 Σεπτεμβρίου 2024]. pages 1–4. Available: https://link.springer.com/10.1007/978-3-030-32256-4_3-1
10. Gambhir SS, Berman DS, Ziffer J, Nagler M, Sandler M, Patton J. A Novel High-Sensitivity Rapid-Acquisition Single-Photon Cardiac Imaging Camera. J Nucl Med. April 2009;50(4):635–43.
11. Zanzonico P. Instrumentation for Single-Photon Emission Computed Tomography (SPECT). Στο: Volterrani D, Erba PA, Strauss HW, Mariani G, Larson SM. Nuclear Oncology. Cham: Springer International Publishing; 2022 [26 September 2024]. pages 1–27. Available: https://link.springer.com/10.1007/978-3-319-26067-9_5-2
12. Peil S, Gabrielse G. Observing the Quantum Limit of an Electron Cyclotron: QND Measurements of Quantum Jumps between Fock States. Phys Rev Lett. 16 August 1999;83(7):1287–90.
13. Wagner HN. A brief history of positron emission tomography (PET). Semin Nucl Med. July 1998;28(3):213–20.

14. Belcari N, Bisogni MG, Del Guerra A. Positron emission tomography: its 65 years and beyond. *Riv Nuovo Cimento*. 18 March 2024 Available: <https://link.springer.com/10.1007/s40766-024-00050-3>
15. Ter-Pogossian MM. PET, SPECT, AND NMRT: Competing.
16. Karp J, Mankoff D. Evolution of PET technology – from early days, to the PennPET Explorer.
17. Internationale Atomenergie-Organisation. Quality assurance for PET and PET/CT systems. Vienna: Internat. Atomic Energy Agency; 2009. 145 σ. (IAEA human health series).
18. Vaquero JJ, Kinahan P. Positron Emission Tomography: Current Challenges and Opportunities for Technological Advances in Clinical and Preclinical Imaging Systems. *Annu Rev Biomed Eng*. 2015;17:385–414.
19. Mettler FA, Guiberteau MJ. Essentials of nuclear medicine imaging. 6th ed. Philadelphia, PA: Elsevier Saunders; 2012.
20. Manabe O, Kikuchi T, Scholte AJHA, El Mahdiui M, Nishii R, Zhang MR, κ.ά. Radiopharmaceutical tracers for cardiac imaging. *J Nucl Cardiol Off Publ Am Soc Nucl Cardiol*. August 2018;25(4):1204–36.
21. Hutton BF. Developments in cardiac-specific SPECT imaging. *Q J Nucl Med Mol Imaging Off Publ Ital Assoc Nucl Med AIMN Int Assoc Radiopharmacol IAR Sect Soc Of*. June 2012;56(3):221–9.
22. Acampa W, Zampella E, Assante R, Lezaic L, Medolago G, Ghilardi A, κ.ά. Myocardial Perfusion Imaging. 10th publ. Vidovič B, επιμελητής. European Association of Nuclear Medicine; 2014 [26 September 2024]. Available: https://eanm-org.staging.codecove.at/wp-content/uploads/2024/06/EANM_2014_Myocardial_Tech_Guide.pdf
23. Dilsizian V, Narula J. Atlas of nuclear cardiology. Fourth edition. New York: Springer; 2013. 457 σ.
24. Harimoto K, Kawasaki T, Honda S, Kinoshita S, Kamitani T, Sugihara H. A Case of Isolated Septal Myocardial Infarction: Myocardial Perfusion-metabolism Mismatch as a Tool for Diagnosis. *Oman Med J*. December 2019;34(3):257–61.
25. Paul AK, Nabi HA. Gated myocardial perfusion SPECT: basic principles, technical aspects, and clinical applications. *J Nucl Med Technol*. December 2004;32(4):179–87; quiz 188–9.
26. Horvath J. A Brief History of 3D Printing. Στο: *Mastering 3D Printing [Διαδίκτυο]*. Berkeley, CA: Apress; 2014. pages 3–10. Available: http://link.springer.com/10.1007/978-1-4842-0025-4_1
27. Mhmood TR, Al-Karkhi NK. A Review of the Stereo lithography 3D Printing Process and the Effect of Parameters on Quality. *Al-Khwarizmi Eng J*. 5 June 2023;19(2):82–94.

28. Li Z, Rathore AS, Song C, Wei S, Wang Y, Xu W. PrinTracker: Fingerprinting 3D Printers using Commodity Scanners. Στο: Proceedings of the 2018 ACM SIGSAC Conference on Computer and Communications Security [Διαδίκτυο]. Toronto Canada: ACM; 2018. pages 1306–23. Available: <https://dl.acm.org/doi/10.1145/3243734.3243735>
29. Kristiawan RB, Imaduddin F, Ariawan D, Ubaidillah, Arifin Z. A review on the fused deposition modeling (FDM) 3D printing: Filament processing, materials, and printing parameters. *Open Eng.* 16 April 2021;11(1):639–49.
30. Chen AN, Wu JM, Liu K, Chen JY, Xiao H, Chen P, κ.ά. High-performance ceramic parts with complex shape prepared by selective laser sintering: a review. *Adv Appl Ceram.* 17 February 2018;117(2):100–17.
31. Song Y, Ghafari Y, Asefnejad A, Toghraie D. An overview of selective laser sintering 3D printing technology for biomedical and sports device applications: Processes, materials, and applications. *Opt Laser Technol.* April 2024;171:110459.
32. Deng W, Xie D, Liu F, Zhao J, Shen L, Tian Z. DLP-Based 3D Printing for Automated Precision Manufacturing. Wu CH. *Mob Inf Syst.* 4 May 2022;2022:1–14.
33. Singh AP, Pervaiz S. Current Status and Prospects of Multi-Jet Fusion (MJF) Based 3D Printing Technology. Volume 2A: Advanced Manufacturing. Virtual, Online: American Society of Mechanical Engineers; 2021. Available at: <https://asmedigitalcollection.asme.org/IMECE/proceedings/IMECE2021/85550/V02AT02A023/1132364>
34. Park BJ, Choi HJ, Moon SJ, Kim SJ, Bajracharya R, Min JY, κ.ά. Pharmaceutical applications of 3D printing technology: current understanding and future perspectives. *J Pharm Investig.* 29 October 2018; Available at: <http://link.springer.com/10.1007/s40005-018-00414-y>
35. Paul GM, Rezaenia A, Wen P, Condoor S, Parkar N, King W. Medical Applications for 3D Printing: Recent Developments. *Mo Med.* 2018;115(1):75–81.